Theoretical Study on Compound Chondrule Formation

Seiji Yasuda

February 2009

Theoretical Study on Compound Chondrule Formation

Seiji Yasuda
(Doctoral Program in Physics)

Submitted to the Graduate School of
Pure and Applied Sciences
in Partial Fulfillment of the Requirements
for the Degree of Doctor of Philosophy in
Science

at the
University of Tsukuba

Abstract

Chondrules are spherical-shaped, silicate particles that are the main component of chondritic meteorites. It is considered that they were formed by some heating (melting) events in the early solar nebula. There are compound chondrules, which are two or more chondrules fused together. Although the fraction of compound chondrules is very small ($\sim$ 5% of all chondrules), they offer crucial information regarding the physical states of solid materials during chondrule formation because of its uniqueness. Some compound chondrules seem to be formed by collisions of two independent particles during heating events in the solar nebula. However, the probability of random collisions in the early solar nebula is too small to explain the observed fraction of compound chondrules. Although some formation models for compound chondrules were proposed and examined the collision probability of particles, they did not notice the collision conditions. If two drops experience the high-speed or grazing collision, they would not coalesce. Or if the viscosities of both drops are too low, they would not keep their shape and would fuse together by surface tension. In this study, we simulate collisions of two silicate drops with three-dimensional hydrodynamics simulation in order to examine the collision conditions for compound chondrule formation quantitatively.

First, we examined "condition for coalescence" for various parameters; the collision velocity, the collision angle, the diameters and the viscosities of drops. We can classify the results of drops collisions into three groups; "Stretching separation", "Disruption", and "Coalescence". And we have understood the condition for coalescence with the energy balance.

Second, we examined "condition for keeping shape". In order to keep drops shape, the deformation timescale has to be longer than the solidification timescale. When the relative velocity is relatively low, the deformation is controlled by ram pressure of collision and the deformation time can be understood by the timescale of transit time of two drops. On the other hand, when the relative velocity is relatively high, it is controlled by the surface tension and we found that the deformation of the large drop is modeled by the oscillation of a viscoelastic body and the deformation time can be written as a quarter of the period

of damped oscillation. Moreover, we found that the boundary between these two cases can be obtained from the balance between the kinetic energy, which tends to deformation of the large drop and the viscous dissipation just after collision.

The solidification time is difficult to estimate because the crystallization processes by collision have not been understood well. In this paper, we assume the seed of the crystal occurs at the interaction region and define the solidification time as the growth time of crystal. It is the lower limit of the solidification time, so we can obtain the least viscosities of drops to satisfy the condition for keeping shape. In the ram pressure control case, the deformation time is longer than the solidification time for every viscosity, so it seems to be difficult to form compound chondrule by the collision in the ram pressure control case. In the surface tension control case, the deformation time is longer than the solidification time when the viscosities of the two drops are larger than about 330 poise. Therefore, in order to satisfy the condition for keeping shape, the collision should be the surface tension control case and the viscosities of the two drops are, at least, larger than about 330 poise.

Thus, we have obtained the collision conditions for compound chondrule formation quantitatively. Since we analytically understood the phenomena of drop collisions, we can know the conditions without using numerical simulations for a wide range of collision parameters and verify the formation models.

Then, we verified the "fragment-collision in the shock-wave heating model", which is one of the plausible models for compound chondrule formation, proposed by Miura et al. (2008a). In the "fragment-collision model", they noticed that the compound chondrule formation may take place due to mutual collisions among the fragments that are generated from a large dust particle. In the shock-wave heating model, which is one of the most plausible models for chondrule formation, the gas friction heats and melts the surface of the cm-sized dust particle and then the strong gas ram pressure causes the disruption of the molten surface layer.

We carried out three-dimensional hydrodynamics simulations of the disruption of a partially-molten dust particle exposed to high-speed gas flow in order to obtain the collision parameters

of collisions among the fragments. The hydrodynamics simulation shows details of the disruptive motion of the molten surface, production of many fragments, their trajectories parting from the parent particle, and mutual collisions among them. In our simulation, we identified 32 isolated fragments extracted from the parent particle. We detected 12 collisions between the fragments and obtained collision parameters with “Clump Find method”. The typical collision parameters show that almost all collisions turn out to be the ram pressure control cases. This result indicates that the collisions just after disruption satisfy the condition for coalescence but does not satisfy the condition for keeping shape.

Finally, we considered two possibilities to form compound chondrules in the fragment-collision model. First is a case where there is a temperature (viscosity) difference between two ejectors at the time of ejection. Second is a case where the collision among the ejectors that are from different disruption event take place.

Acknowledgments

I'm eternally grateful to my collaborators, Taishi Nakamoto and Hitoshi Miura for great discussions and suggestions. I express my appreciation to Masayuki Umemura for supports in my research activity. I also greatly appreciate helpful comments and suggestions for the crystallization process by Kyoko Tanaka and the modeling of the drop deformation phenomena by Kei Tanaka. I would like to give my thanks Masayuki Umemura, Masao Mori, Naomasa Nakai, and Taishi Nakamoto for reviewing my dissertation and great discussions. I am grateful to Toshihiko Kadono, Masayuki Uesugi, Katsuo Tsukamoto, Shogo Tachibana, Ryoichi Nishi, Masao Mori and Shigeru Ida for their comments and suggestions on my research. I owe coworkers in University of Tsukuba and Tokyo Institute of Technology many obligations. They gave a lot of comments and suggestions and I was stimulated by them. This work is supported by the Research Fellowship of Japan Society for the Promotion of Science for Young Scientists.

Finally, I would like to thank my parents, Masaki Yasuda and Michie Yasuda who have supported my research activity.

Contents

1 Chondrules and Compound Chondrules

1.1 Chondrules

Chondrules are mm-sized, spherical-shaped, silicate particles abundant in chondritic meteorites, which are the majority of meteorites falling onto the Earth (Figure 1). They are thought to have been formed from the dust particles heated by some flash heating event, melted, rounded by the surface tension, and cooled again in the early solar nebula (e.g., Jones et al. 2000). It is believed that the chondrules have crucial clues for planet formation, especially for planetesimal formation because of its solidification age and the formation process. The solidification age of general chondrules is about 4.56×10^9 yrs ago (Amelin et al. 2002). This age indicates that the formation of chondrules may occur before or around the same time of formation of planetesimals. In addition, the process of planetesimal formation is accumulation of the dust particles and that of chondrule formation is flash heating event of the dust particles. The fact that chondrules are included in meteorites indicates that the flash heating events occurred during the planetesimal formation.

1.2 Compound Chondrules

Compound chondrules, which are two or more chondrules fused together, exist in the various classes of chodrites (Figure 2). Although the fraction of compound chondrules is very small ($\sim$5% of all chondrules), they offer crucial information regarding the physical and chemical states of solid materials during chondrule formation because of their uniqueness (Gooding and Keil 1981, Wasson et al. 1995, Sekiya and Nakamura 1996, Akaki and Nakamura 2005, Ciesla 2006). Some compound chondrules seem to have been formed by mutual collisions between two or more independent chondrules during the heating event (Wasson et al. 1995, Akaki and Nakamura 2005). Compound chondrules have some physical features, which constraint their formation process. We introduce some of them below.

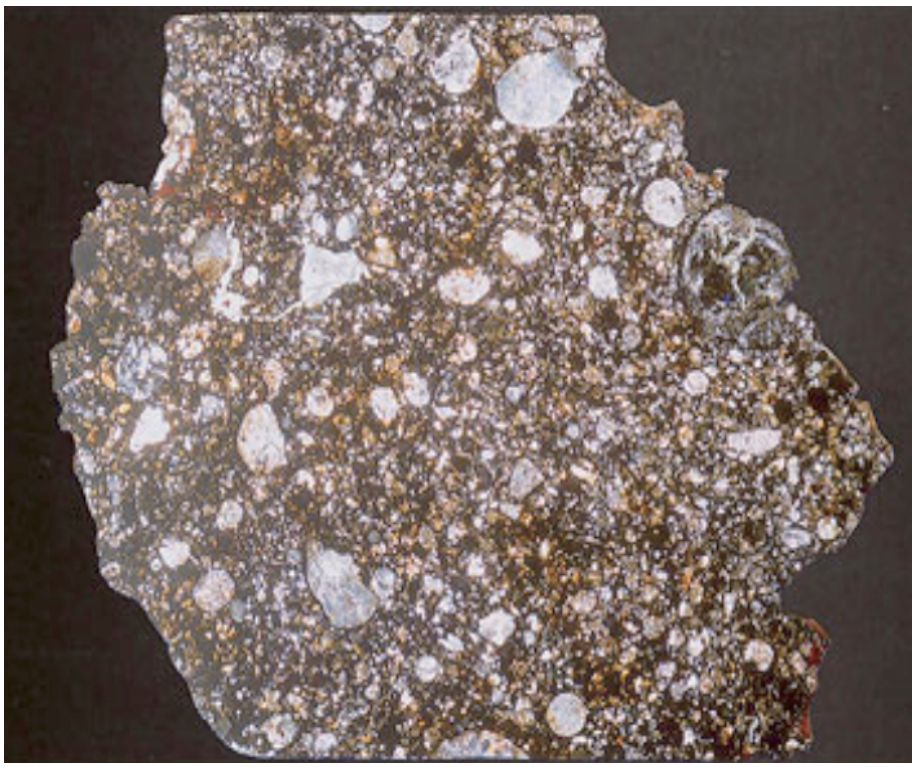

Figure 1: A transmitted light image of a thin section of Yamato-691 (EH3). The section shows numerous small chondrules. Long dimension is 16.5 mm. (from HP of Antarctic Meteorite Research Center)

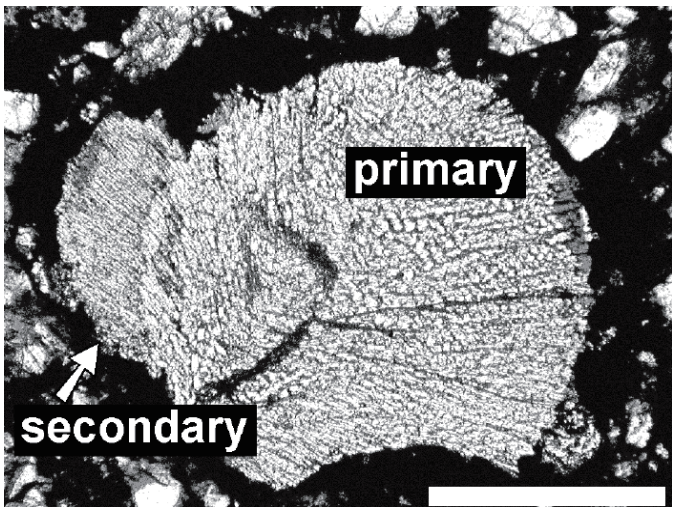

Figure 2: Compound chondrule in the Y793596, LL3.0 chondrite composed of two radial pyroxene chondrules. Scale bar is 300 μm in length (Akaki and Nakamura 2004).

1.2.1 Fraction

The fraction of compound chondrules is about 5% of all chondrules (Wasson et al. 1995, Akaki and Nakamura 2005). This fraction is one of the most important constraints on the formation process of the compound chondrules, becuase it is considered that the rate of mutual collisions among molten dust particles in the early solar nebula is too low to explain the observed fraction of compound chondrules when one estimates the number density of the dust particles based on the minimum mass solar model (Gooding and Keil 1981, Wasson et al. 1995, Sekiya and Nakamura 1996). For example, the collision rate during the heating event at 3AU (around asteroid belt) is at most

$$P_{\rm coll} = n_{\rm d}\Delta v_{\rm max}\pi r_{\rm max}^2 t_{\rm h} \sim 10^{-5} \left(\frac{n_{\rm d}}{10^{-9}\ {\rm cm}^{-3}}\right)\left(\frac{\Delta v_{\rm max}}{100\ {\rm cm\ s}^{-1}}\right)\left(\frac{r_{\rm max}}{1\ {\rm mm}}\right)^2\left(\frac{t_{\rm h,\ max}}{100\ {\rm sec}}\right), \quad (1)$$

where $n_{\rm g}$, $r_{\rm max}$, $\Delta v_{\rm max}$, and $t_{\rm h,\ max}$ are the number density of the dust particle at 3AU, the maximum radius of chondrules, the maximum relative velocity, which is constrained from the destruction of chondrule precursors, and the maximum heating time, which is constrained from the existence in volatile elements in chondrules, respectively. It indicates that the number density of molten dust particles should be enhanced in the chondrule forming region.

1.2.2 Size Ratio of Primary and Secondary

Wasson et al. (1995) defined compound chondrules based on textures and assigned each constituent chondrule as primary and secondary. The primary chondrule was rigid enough to retain its original shape at the time of compound chondrules formation. On the contrary, the secondary chondrule had a low viscosity enough to allow it to deform the shape of the primary. Wasson et al. (1995) also measured the mean and the median diameters of primaries and secondaries in compound chondrules and obtained the ratio of the secondary diameter to the primary diameter. They found that the mean and the median of the ratio are about 0.3 and 0.25, respectively, that is, the primary is smaller than the secondary. If the different viscosities of two components are caused by the different temperatures, the primary should be cooler than the secondary at their collision. However, if we assume that they were heated

in the same heating event, the primary should be hotter than the secondary, because the larger particle cools efficiently. This feature can be a strong constraint on the formation model of compound chondrules.

1.2.3 Shape

The most apparent feature of compound chondrules is that two chondrules attach and keep their shape, that is, we can clearly discriminate the components in compound chondrules. This feature would provide the conditions for collisions of molten dust particles (the relative velocity, the collision angle, and the viscosities of two chondrule precursors). However, unfortunately, we do not have quantitative conditions due to the difficulty of the experiments of two silicate drop collisions or numerical simulations. We will develop in this work a numerical simulation code for investigating two silicate drop collisions with the CIP method and give the quantitative indicator to the collision conditions in part I of this dissertation.

1.3 Shock-Wave Heating Model

Shock-wave heating model is one of the plausible models for chondrule formation (Jones et al. 2000). In order to form chondrules, the heating mechanism for chondrule precursor has to satisfy some observational constraints (e.g., peak temperature, heating rate, cooling rate, size distribution, shape, and so on; Jones et al. 2000). The shock-wave heating model has been studied by many authors and they suggest that it could explain the observational constraints (this point is summarized in detail in Miura 2006). The heating mechanism of the shock-wave heating model is very simple. Let us suppose that a shock wave passes through the solar nebula that consists of gas and dust particles. Dust particles tend to remain the original position, while the gas is accelerated by the gas pressure immediately. As a result, the relative velocity generates between the gas and the dust particle and the dust particles are heated by the gas frictional heating (a schematic picture is Figure 3).

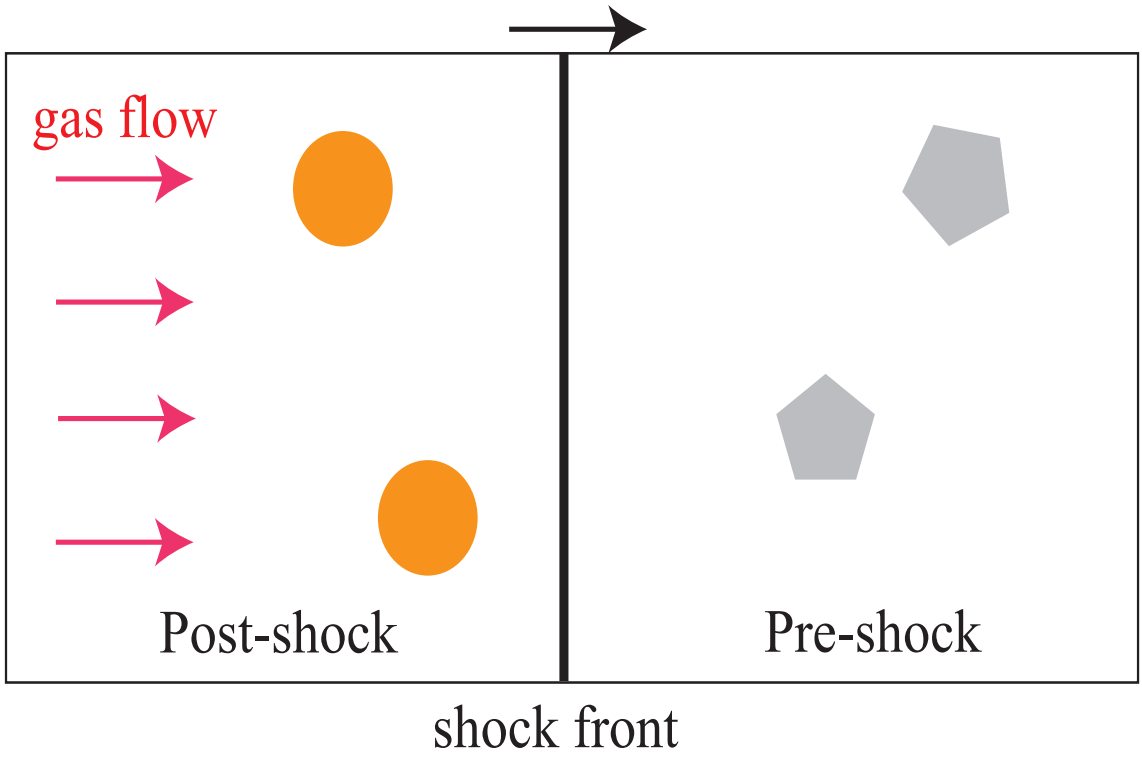

Figure 3: A schematic picture of the shock-wave heating model. The solar nebula consists of gas and dust particles. If a shock wave passes through the region, the post-shock gas is accelerated suddenly. On the contrary, the dust particle tends to remain the original position. As a result, the dust particles are heated by the gas friction.

1.4 Compound Chondrule Formation in Shock-wave Heating Model

As we estimated in subsection 1.2.1, the number density of molten dust particles should be enhanced to form enough amount of compound chondrules. However, Nakamoto and Miura (2004) have suggested that if the density of the large dust particles is higher than a critical value, they would be destroyed by a shock wave. Thus, it seems that the number density of the precursor particles should be lower than the critical density to produce the compound chondrules in the framework of the shock-wave heating model.

A model that may meet these conditions, i.e., the low number density of the precursor particles and the high frequency of collisions among molten particles, is the fragment-collision model proposed by Miura et al. (2008a). If there exists a cm-sized dust particle, only the surface is heated and melted due to the gas frictional heating because of its large size (Yasuda and Nakamoto 2005, 2006). The molten surface is torn by the strong gas ram pressure, and then a lot of fragments would be extracted from the original dust particle. The disruption event was examined by experimentally (Kadono and Arakawa 2005, 2008), analytically (Kato et al. 2006), and numerically (Miura and Nakamoto 2007). Since the local number density of fragments behind the original dust particle is enhanced, the mutual collisions among these fragments are likely to occur frequently. In addition, the collisions would occur during chondrule formation as inferred from the observations of compound chondrules. Miura et al. (2008a) estimated the collision probability, which is the number of collisions experienced by a fragment in one disruption event, is up to ~ 0.5, which is much larger than the observed fraction of compound chondrules ($\sim 5\%$). Therefore, the observed fraction can be explained if some fraction (e.g., 10%; Miura et al. 2008a) of large dust particles experienced the disruption event in the chondrule-forming region.

In the simple model proposed by Miura et al. (2008a), they calculated the collision probability by using statistical quantities (velocity dispersion and number density of fragments) in which the radii of all fragments were uniform. However, the velocity dispersion does not necessarily lead to the mutual collisions among fragments; e.g., the case in which fragments

are ejected radially from the original dust particle and they have velocities proportional to the distance from the original dust particle. In addition, even if the fragments collide each other, they do not coalesce necessarily because the condition whether the colliding two drops coalesce or not depends on the collisional velocity (Weber number of impact) and the collision angle (impact parameter) according to the water drop collision experiments (Ashgriz and Poo 1990, Qian and Law 1997). Moreover, even if they coalesce, they do not always keep their shape. It depends not only on the collision velocity and angle but also on the viscosities of two drops.

In order to answer these matters, we have to obtain the physical values of each fragment (velocity, position, radius, and orbit) and the condition of each collision (Weber number of impact and impact factor), not the statistical quantities as used by Miura et al. (2008a).

1.5 Purposes of This Thesis

The first purpose of this work is to examine the collision conditions for compound chondrule formation. We simulate collisions of two silicate drops for various parameters (collision velocity, collision angle, diameters of drops, and viscosities of drops) with three-dimensional hydrodynamics calculations (Part I).

- We classify collision outcomes, investigate their boundaries analytically, and obtain the condition for coalescence for a wide range of parameters (section 4).
- We investigate the condition for keeping shape for parameters that satisfy the condition for coalescence by comparing the deformation time of a large drop, which is obtained from numerical simulation, with the solidification time, which is obtained from the theory of crystallization (section 5).

We can obtain the collision conditions (condition for coalescence and condition for keeping shape) for compound chondrule formation for a wide range of parameters. In this stage, we can verify the compound chondrule formation models proposed so far from the view point of the collision conditions.

The second purpose is to verify the fragment-collisoion model from the view point of the collision conditions. We examine the disruption of a half-molten dust particle and dynamics of fragments with three-dimensional hydrodynamics simulations (Part II).

- We trace the motion of each fragment extracted from the original dust particle and obtain the radius, velocity and position at every moment. From this simulation, we can analyze the phenomena of collisions among fragments and obtain the relative velocities and collision angles of impacts (section 10).
- Comparing these quantities with results of collision conditions obtained from Part I, we discuss whether these collisions contribute to the formation of compound chondrules or not and then calculate the probability of the compound chondrule formation (section 11).

Part I

Collision Condition for Compound Chondrule Formation

2 Introduction

A lot of compound chondrule formation models were proposed by numerous researchers (Gooding and Keil 1981, Wasson et al. 1995, Sekiya and Nakamura 1996, Liffman 1996, Ciesla 2006, Miura et al. 2008). Almost all papers noticed that how the collision probability is raised up to the fraction of compound chondrules is on a key. However, in spite of its importance, collision conditions was not considered because we do not know what collisions can make compound chondrules quantatively. If two melting particles experience a high-speed or grazing collision, they would not coalesce. Or if the viscosities of both components are too low, they would not keep their shape and would fuse together by surface tension. In such cases, we cannot observe them as compound chondrules. Thus, we are necessary to consider the collision conditions to compare the various formation models with some observation.

The purpose of this part is to examine the collision condition for compound chondrule formation quantitatively. We investigate collisions of two silicate drops with three-dimensinal hydrodynamics simulation. We numerically simulate two drop collisions for various parameters (collision velocity, collision angle, diameters of drops, and viscosities of drops) and categorize thier outcomes. In addition, we analytically interpret these numerical results. We will examine the condition for coalescence, which means whether colliding two drops coalesce or not in section 4 and the condition for keeping their shape, which means whether or not solidification occurs before their deformation in section 5. From these conditions, we obtain the collision condition for forming compound chondrules. We verify the compound chondrule

formation models so far with the collision condition in section 6.

3 Model

3.1 Collision Parameters

We simulate the collision of two drops for various parameters. Collision outcomes significantly depend on the diameters (d_1, d_2) and viscosities (μ_1, μ_2) of drops, relative velocity ($u = |u_1 - u_2|$), and collision angle θ, where we define the drop 1 is smaller than the drop 2 (figure 4).

Our numerical simulation covers a wide range of collision parameters. According to experiments of binary drop collision (Ashgriz and Poo 1990, Jiang et al 1992, Qian and Law 1997, etc.), the collision outcomes significantly depend on the three dimensionless parameters. They are the Weber number, drop diameters ratio Δ, and the non-dimensional impact parameter Im, which are defined as follows:

$$We = \frac{\rho_{\mathrm{d}} d_1 u^2}{\gamma_{\mathrm{s}}}, \qquad \Delta = \frac{d_1}{d_2}, \qquad Im = \frac{2D}{d_1 + d_2}, \tag{2}$$

where D is the impact parameter defined as the distance between the center of masses of the two drops. In addition to these non-dimensinal parameters, d_2, μ_1, μ_2 are also important parameters in the case of high viscous drops. When we consider the binary water drop collisions, the viscous dissipation in a water drop is not significant and it can be neglected (Ashgriz and Poo 1990). However, when we consider high viscous drop collisions, viscous dissipation is important for collision outcomes. Moreover, we have to treat not only the size ratio but also the size of a large drop as an important parameter in the case of binary high viscous drop collisions (subsection 4.4.3).

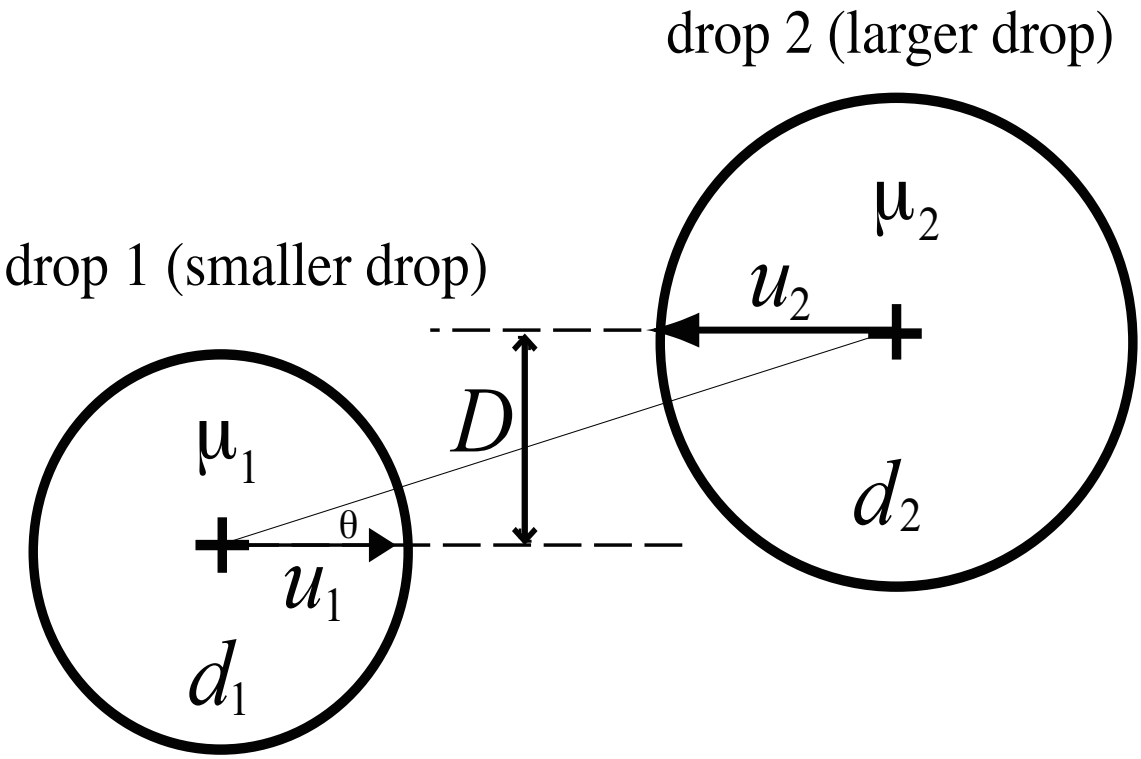

Figure 4: A schematic picture of the collision of the two drops.

3.2 Basic Equations

In order to simulate the collision of two drops, we solve the equations of continuity, motion, and energy. The basic equations of continuity and motion are almost the same as adopted by Miura and Nakamoto (2007), so we can use the same numerical scheme to solve these equations. They developed the numerical simulation code using the Cubic Interpolated propagation (CIP) scheme in order to examine the deformation of a drop exposed to the fast gas flow. The detailed numerical scheme to solve the equation of continuity and motion is written in Miura and Nakamoto (2007). The energy equation, however, was not considered in Miura and Nakamoto (2007). The internal energy is transported by the fluid motion. When we consider two different viscous drops, we have to solve the energy equation because the viscosity is the function of the internal energy. In this subsection, we review the equations of continuity and motion adopted in Miura and Nakamoto (2007) and then introduce a method of solving the energy equation.

3.2.1 Equation of Continuity

In order to express two drops, that is, the drops in the computational domain, we use the color function ϕ, which takes the value of unity ($\phi = 1$) inside the drops, and zero ($\phi = 0$) outside of them. Using the color function, the density of the fluid element ρ is given by

$$\rho = \rho_{\rm d}\phi + \rho_{\rm a}(1 - \phi), \tag{3}$$

where the subscripts "d" and "a" indicate the drops and the ambient region, respectively. The equation of continuity is written by using the color function under the condition of $\rho_{\rm a}/(\rho_{\rm d} - \rho_{\rm a}) \ll 1$ as

$$\frac{\partial \phi}{\partial t} + \boldsymbol{\nabla} \cdot (\phi \boldsymbol{u}) = 0, \tag{4}$$

where $\boldsymbol{u}$ represents the velocity of fluid element (Miura and Nakamoto 2007). This equation describes the time evolution of the color function, in addition, the density ρ through Eq. (3).

3.2.2 Equation of Motion

The equation of motion is given by

$$\frac{\partial \boldsymbol{u}}{\partial t} + (\boldsymbol{u} \cdot \boldsymbol{\nabla})\boldsymbol{u} = \frac{-\boldsymbol{\nabla} p + \mu \triangle \boldsymbol{u} + \boldsymbol{F}_{\mathrm{s}}}{\rho}, \tag{5}$$

where p, μ, and $\boldsymbol{F}_{\mathrm{s}}$ are the pressure, the viscosity, and the surface tension, respectively. The viscosity is expressed by using the color function as

$$\mu = \begin{cases} \mu_{\mathrm{a}} & \text{for } \phi \leq \phi_{\mathrm{a}}, \\ \mu_{\mathrm{a}} \exp\left[\frac{\ln(\mu_{\mathrm{d}}/\mu_{\mathrm{a}})}{1-\phi_{\mathrm{a}}}(\phi - \phi_{\mathrm{a}})\right] & \text{for } \phi_{\mathrm{a}} < \phi \leq 1 \end{cases} \tag{6}$$

where μ_{d} and μ_{a} are viscosities of the drops and the ambient region, respectively. In our model, μ_{d} is a function of the internal energy of the drops. We assume that a cell that has the color function less than ϕ_{a} is the ambient region and we set $\phi_{\mathrm{a}} = 10^{-2}$ in this work. It should be noted that the forces $\boldsymbol{F}_{\mathrm{s}}$ takes place only at the surface of the drops ($|\boldsymbol{\nabla}\phi| \neq 0$).

3.2.3 Equation of State

We can obtain the equation that describes the time evolution of the pressure p from the equation of state, which is given by

$$\frac{dp}{d\rho} = c_{\mathrm{s}}^2, \tag{7}$$

where c_{s} is the sound speed. We can rewrite it into

$$\frac{dp}{dt} = c_{\mathrm{s}}^2 \frac{d\rho}{dt}. \tag{8}$$

Substituting the mass conservation equation, we obtain

$$\frac{dp}{dt} + (\boldsymbol{u} \cdot \boldsymbol{\nabla})p = -\rho c_{\mathrm{s}}^2 \boldsymbol{\nabla} \cdot \boldsymbol{u}. \tag{9}$$

3.2.4 Equation of Energy

In order to express the collision of two drops that have different viscosities, we change the value of viscosities of drops μ_{d} depending on the internal energy. We model the viscosity of the dust particle as a function of the internal energy as shown in Figure 5. The horizontal

axis shows the internal energy per unit volume e and the vertical one shows the viscosity $\mu_{\rm d}$ in the logarithmic scale. We set $\mu_{\rm d} = \mu_{\rm liq}$ at $e = e_{\rm liq}$ and $\mu_{\rm d} = \mu_{\rm sol}$ at $e = e_{\rm sol}$, where $e_{\rm sol}$ and $e_{\rm liq}$ are internal energies at the liquidus and solidus, respectively. We assume that the viscosity is given by

$$\mu_{\rm d} = \begin{cases} \mu_{\rm sol} & \text{for } e \leq e_{\rm sol}, \\ \mu_{\rm sol} \exp\left[\frac{\ln(\mu_{\rm liq}/\mu_{\rm sol})}{e_{\rm liq}-e_{\rm sol}}(e - e_{\rm sol})\right] & \text{for } e_{\rm sol} < e < e_{\rm liq}, \\ \mu_{\rm liq} & \text{for } e_{\rm liq} \leq e. \end{cases} \tag{10}$$

Since the internal energy is transported by the fluid motion, we need to solve the advection of the internal energy. The energy conservative equation is written by

$$\frac{\partial e}{\partial t} + \boldsymbol{\nabla} \cdot (e\boldsymbol{u}) = 0. \tag{11}$$

3.3 Numerical Simulation

3.3.1 Numerical Model

We consider two drops and simulate collision of them. Figure 6 shows a schematic picture of our numerical model and coordinate system. We adopt the Cartesian coordinate system (x, y, z), which is co-moving with the mass center of drops. In order to express the drops, we use the color function as mentioned in subsection 3.2.1, that is, $\phi = 1$ for drops and $\phi = 0$ for the ambient region. While we calculate outside of the drops for simplicity, we have to reduce the influence of the ambient region on the dynamics of the drops as much as possible. In order to do so, we put the density and the sound velocity of the ambient region as $\rho_{\rm a} = 10^{-6}$ g cm^{-3} and $c_{\rm s,a} = 10^{-5}$ cm s^{-1} (see Miura and Nakamoto 2007, section 4.2).

3.3.2 Numerical Scheme

When we solve the equation of continuity (Eq. 4), we have to pay attention to guarantee the mass conservation and to keep the sharp profile of ϕ. Original CIP scheme (Yabe and Wang 1991) does not guarantee the mass conservation, so we adopt the R-CIP-CSL2 scheme, which

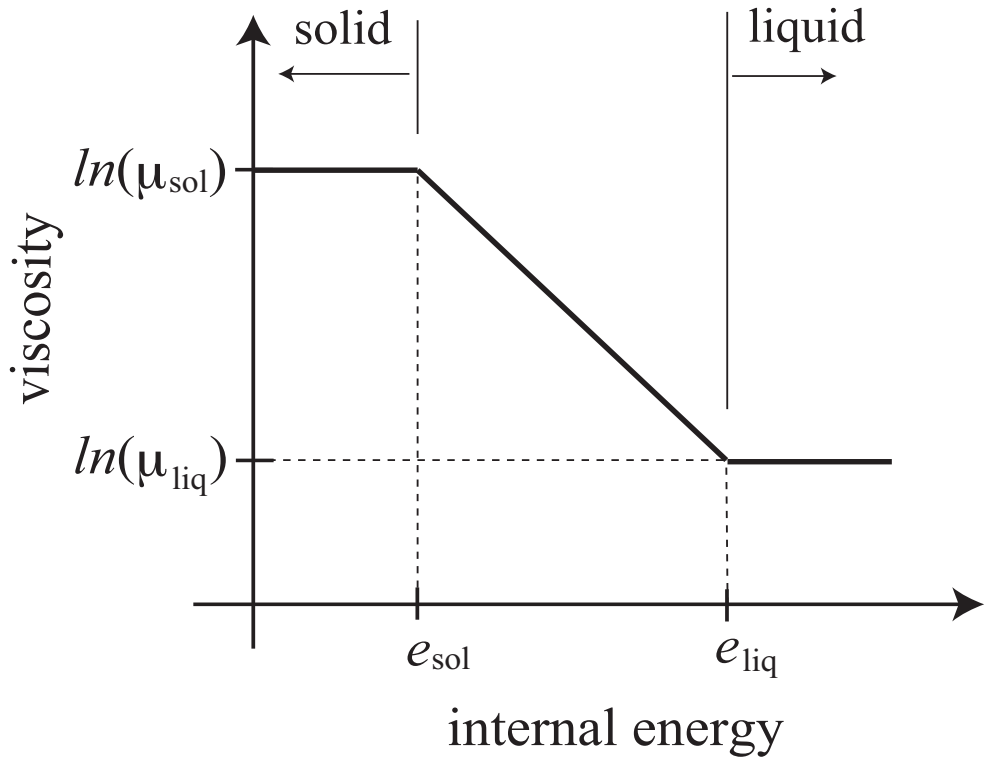

Figure 5: A model of viscosity of the dust particle. The vertical axis and horizontal axis represent the viscosity of the dust particle $\mu_{\rm d}$ in logarithmic scale and the internal energy e, respectively. The solid part ($e < e_{\rm sol}$) has the viscosity of $\mu_{\rm sol}$ and the liquid part ($e > e_{\rm liq}$) has $\mu_{\rm liq}$. The viscosity for $e_{\rm sol} < e < e_{\rm liq}$ is interpolated as shown in this figure.

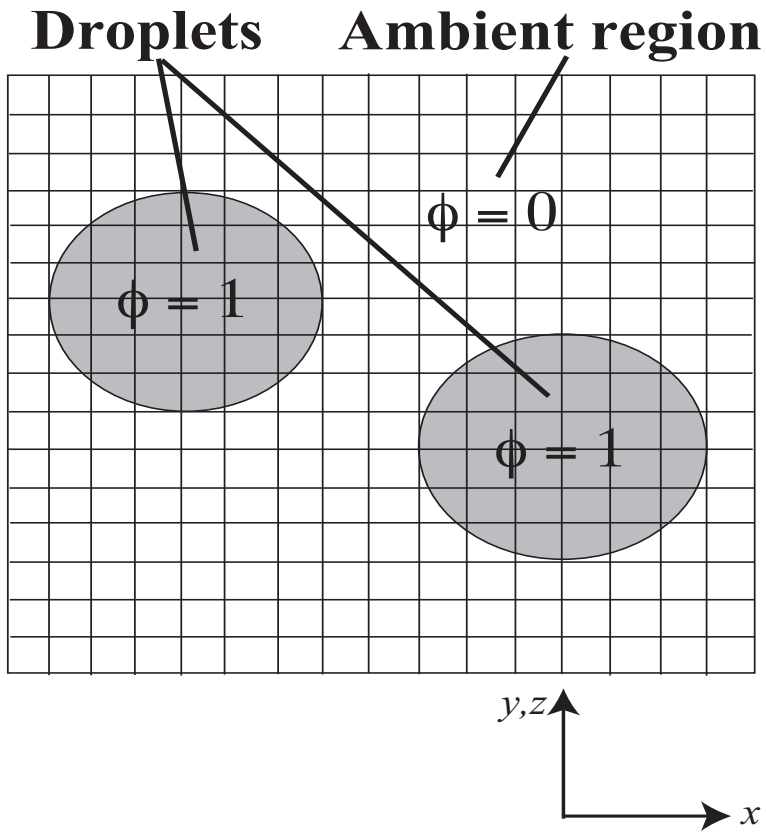

Figure 6: A summary of our numerical model and coordinate system. We adopt the Cartesian coordinate system and express the drops by the color function ϕ.

guarantees the exact conservation (Nakamura et al. 2001). In addition, when we calculate the equation of continuity we use the anti-diffusion technique to avoid numerical diffusion of ϕ, that is, to keep the sharp profile.

The equation of motion (Eq. 5) and the equation of state (Eq. 7) can be separated into the advection phase and the non-advection phase. We solve the advection equations using the R-CIP scheme, which is the oscillation preventing scheme for advection equation (Xiao et al., 1996b) and the non-advection equations using the C-CUP scheme (Yabe et al., 2001; also see Miura et al., 2007).

The evolution of the internal energy e by Eq. (11) can be solved by using the result of the equation of continuity as follows. For simplicity, we explain it in the case of the one-dimensional flow, but an extension to the multi-dimensional flow is straightforward. The mass contained in a spatial cell i at the next time step $n+1$ is calculated by

$$m_i^{n+1} = m_i^n + J_{i-1/2} - J_{i+1/2}, \tag{12}$$

where m_i^n is the mass at the present time step n, $J_{i-1/2}$ is the mass flux from the cell $i-1$ to i. The mass flux $J_{i-1/2}$ has been already obtained by solving Eq. (4). The internal energy e is transported with the mass. The internal energy per unit mass is given by $e\delta_v/m$, where δ_v is the volume of the cell. Therefore, the evolution of the internal energy at the cell i at the time step $n+1$ is given by

$$e_i^{n+1} = e_i^n + J_{i-1/2}(e\delta_v/m)^n_{iup(i-1/2)} - J_{i+1/2}(e\delta_v/m)^n_{iup(i+1/2)}, \tag{13}$$

where iup indicates the cell number of the upstream side, e.g., $iup(i-1/2) = i-1$ for $J_{i-1/2} > 0$ and $iup(i-1/2) = i$ for $J_{i-1/2} < 0$.

3.4 Physical Parameters of Drops

We investigate the binary drop collisions for a wide range of parameters. The range of Weber number is $1 \leq We \leq 1000$, Impact factor covers all the range ($0 \leq x \leq 1$), the size ratios (Δ)

are 0.5 and 1.0, the diameter of the large drop (d_2) is 0.5 mm and 1mm, and the viscosity of small drop (μ_1) is 1 poise and 10 poise. We assume that two drops are forsterite (Mg_2SiO_4) drops. The value of the surface tension coefficient γ_s is 400 dyn cm^{-2} and that of the density ρ_d is 3 g cm^{-3}.

4 Condition for Coalescence

As a result of numerical simulations for various parameters, we can obtain three characteristic collision outcomes (three categories); "coalescence", "stretching separation", and "disruption". In this section, we show the characteristic results of these categories and how collision outcomes change depending on collision parameters.

4.1 Results for Characteristic Parameters

4.1.1 Coalescence

In the case of relatively lower Weber number (lower relative velocity) and lower impact parameter (lower collision angle), two drops coalesce eternally. Figure 7 shows a result of binary drop collision for $d_2 = 1$ mm, $\Delta = 1$ ($d_1 = 1$ mm), $\mu_1 = \mu_2 = 1$poise, $We = 30$ ($u = 200$ cm s^{-1}) and $Im = 0$. When two equal-size drops experience a head-on collision, they form a torus-like structure, which consists of a thin film and a thick circumference (panel f). This structure was also observed in the experiments of binary water drop collision (see Figure 4 in Ashgriz and Poo 1990). Owing to large surface energy, this torus-like drop contracts with mass transfer from the circumference to the film (panels g and h). After that this drop approaches a spherical shape after some oscillation (panels i - l).

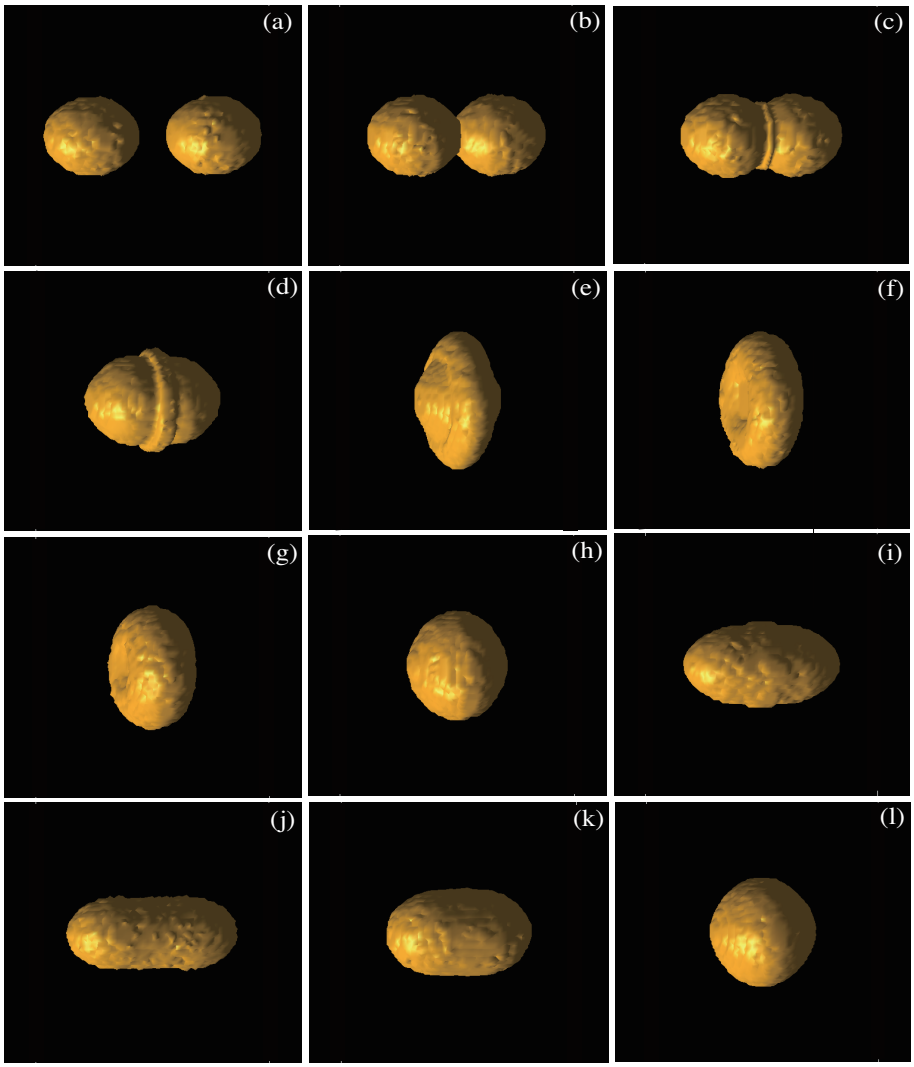

Figure 7: "Coalescence" for $We = 30$, $Im = 0$, $d_2 = 1$ mm, $\Delta = 1$, $\mu_1 = \mu_2 = 1$ poise.

4.1.2 Stretching Separation

In the case of higher impact parameter, we can see a "stretching separation" case. Figure 8 shows a result of $Im = 0.8$, and the other parameters are the same as Fig. 7. In this case, only a portion of two drops comes in direct contact and the remaining portion of the drops tends to move in the direction of their trajectory and consequently stretches the region of interaction (panels c - g). For these parameters, while two drops temporally coalesce, they separate eventually (panels h and i) because the kinetic energy of the portion exceeds the energy dissipations by the surface energy of the interaction region, the viscous dissipation at the interaction region, and the rotational energy generated by their collision.

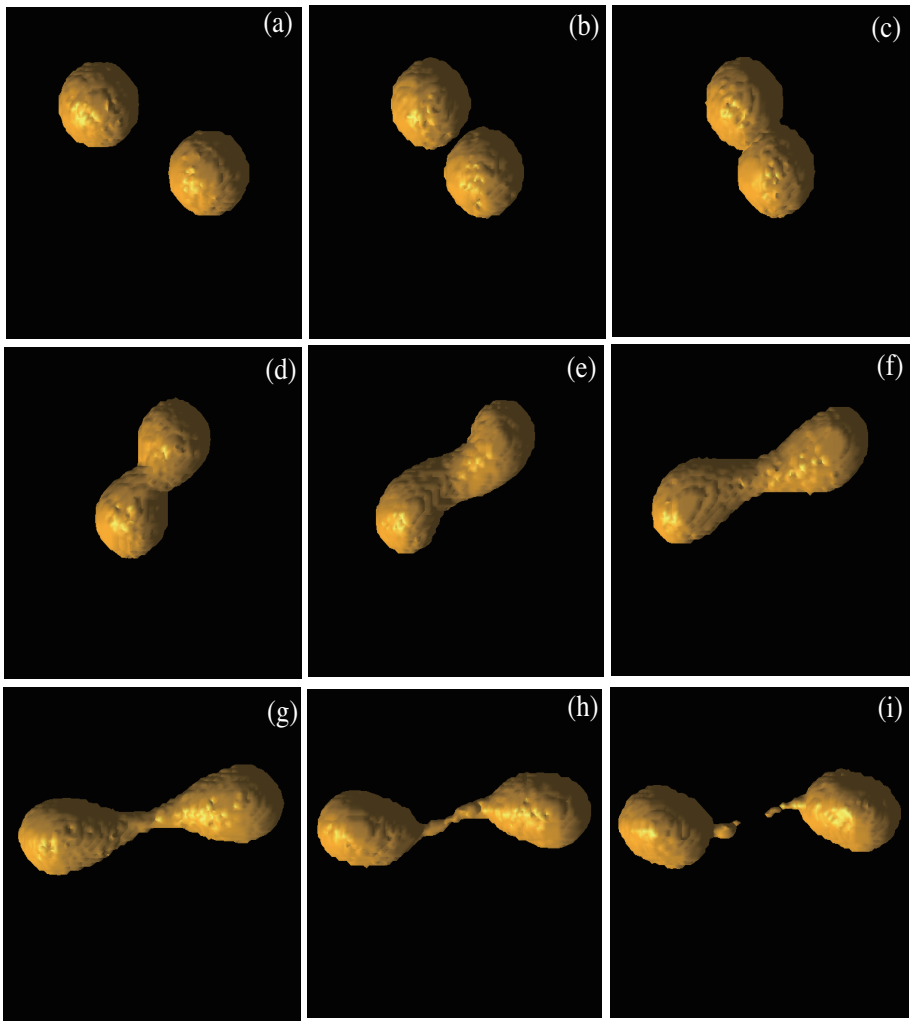

Figure 8: "Stretching separation" for $We = 30$, $Im = 0.8$, $d_2 = 1$ mm, $\Delta = 1$, $\mu_1 = \mu_2 = 1$ poise.

4.1.3 Disruption

In the case of relatively higher Weber number, we can see the "disruption". In experiments of binary water drop collisions, we can see the "reflexive separation" instead of "disruption". It can be interpreted that the critical Weber number for "reflexive separation" ($We_{\rm ref}$) is larger than that of "disruption" ($We_{\rm dis}$) because the viscosity and the surface tension of silicate drop is much larger than those of water drop (Appendix B). Figure 9 shows the result of $We = 190$ ($u = 500$ cm s^{-1}), and the other parameters are the same as Fig. 7. First, it evolves similarly as the case with $We = 30$ (the "coalescence" case in 4.1.1) and two drops form torus-like structure (panel i), while the portion of the circumference spreads due to the large kinetic energy (panels f- h). However, as the deformation proceeds, discontinuity generates between the film and the circumference (panels j and k). So this drop is not able to contract because the mass transfer from the circumference to the film does not take place. As a result, the circumference disrupts into some small drops to decrease the surface energy (panel l).

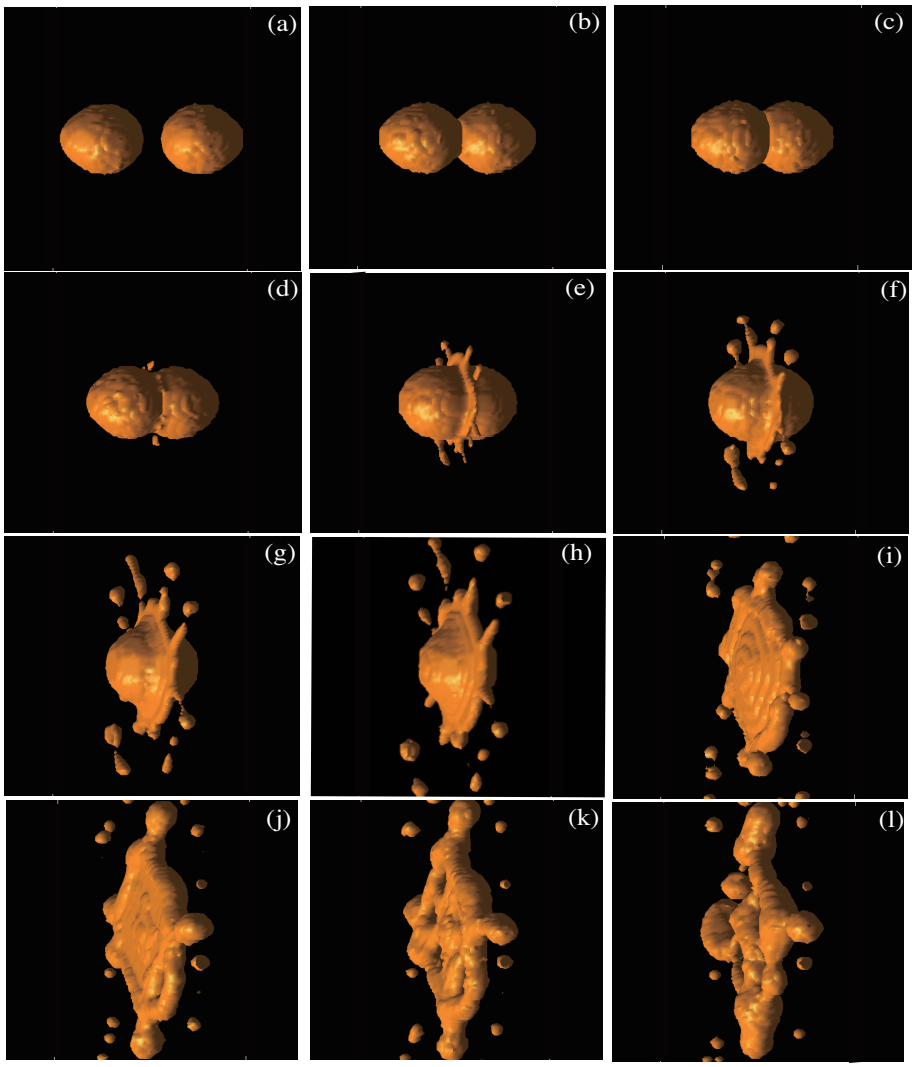

Figure 9: "Disruption" for $We = 190$, $Im = 0$, $d_2 = 1$ mm, $\Delta = 1$, $\mu_1 = \mu_2 = 1$ poise.

4.2 Results for Various Weber Number and Impact Parameter

Figure 10 summarizes simulation results of various Weber numbers and impact parameters. The radii and the viscosities of two drops are $d_2 = 1$ mm, $\Delta = 1$ ($d_1 = 1$ mm), and $\mu_1 = \mu_2 = 1$ poise. Symbols "circle" ($\bigcirc$), "triangle" ($\triangle$), and "square" ($\square$) represent results of "coalescence", "stretching separation", and "disruption", respectively. The solid curve represents the boundary between "coalescence" and "stretching separation" cases and the dashed curve represents that between "coalescence" and "disruption" cases resulted from our analysis with the energy balance (see subsections 4.5 and 4.6). At lower Weber number and lower impact parameter region, we can see "coalescence". When the Weber number is less than about 100 and the impact parameter is small, all collisions result in "coalescence". When the Weber number is fixed and the impact parameter is increased, the region of interaction reduces resulting in a decrement of the ratio of the energy dissipations to the stretching kinetic energy. The "stretching separation" occurs when this ratio reaches a critical value, which will be quantified in subsection 4.5. For small impact parameters, as the Weber number is increased, a critical condition that the discontinuity between the film and the circumference emerges, is generated. The "Disruption" occurs when the kinetic energy for deformation is enough to deform the drop to the critical condition, which will be quantified in subsection 4.6.

4.3 Comparison with Results of Binary Water Drop Collisions

For parameter sets in the previous section, the magnitude of the dissipation by the surface energy is much larger than that of the viscous dissipation (Appendix A). So our numerical results of the boundary between "coalescence" and "stretching separation" should agree with the experimental results for water drop collisions. In figure 11, we compare our numerical results with the experimental results obtained by Ashgriz and Poo (1990). The parameters are the same as Fig. 10. Filled circles and triangles represent the experimental results for "coalescence" and "stretching separation", respectively. Open circles and triangles represent

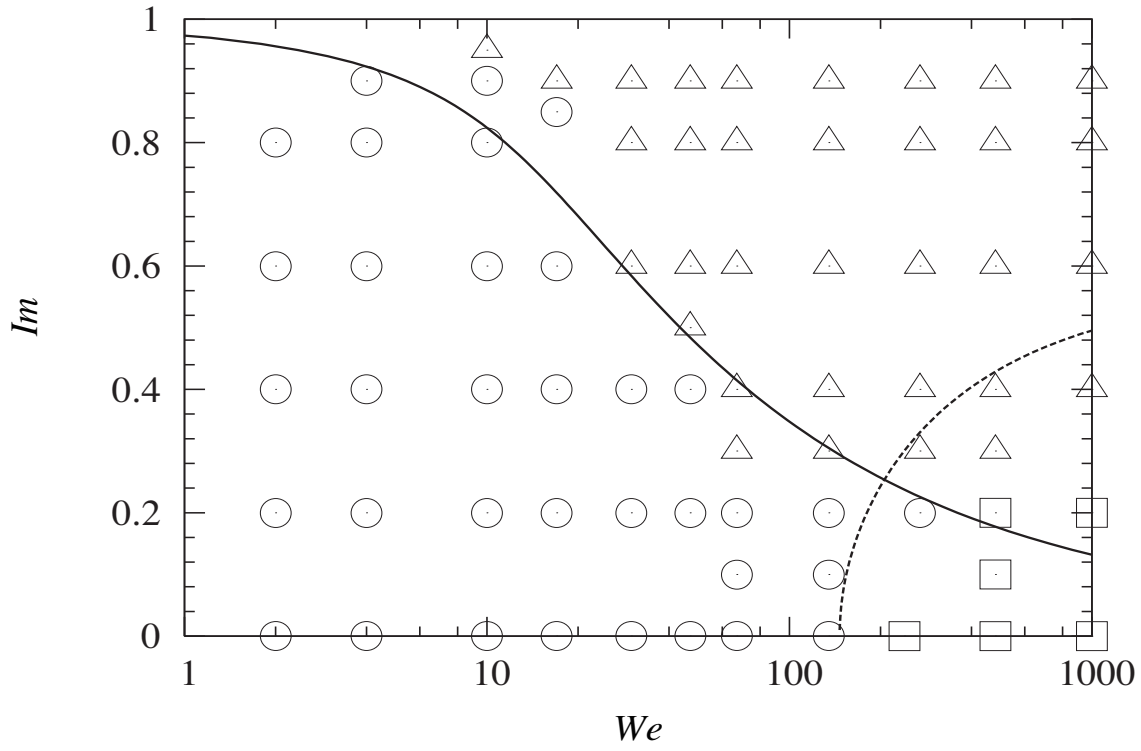

Figure 10: Collisional outcomes of two drops whose radii and viscosities are $d_1 = d_2 = 1$ mm, that is, $\Delta = 1$ and $\mu_1 = \mu_2 = 1$ poise after collision depending on the Weber number (We) and impact factor (Im). The symbols "circle", "triangle", and "square" represent "coalescence", "stretching separation", and "disruption", respectively. The solid and the dashed curves indicate the boundary between "coalescence" and "stretching separation", and"coalescence" and "disruption" analyzed with energy balance (see subsections 4.5 and 4.6).

the numerical results for "coalescence" and "stretching separation", respectively. These symbols show a very good agreement. This is a supporting evidence for the validity of our numerical simulation. It should be noted that the "reflexive separation" case does not appear in our numerical simulation because of different Ohnesorge number (Appendix B).

4.4 Results for Various Parameters

4.4.1 Collision of Two Drops of Different Sizes

The collision of two drops with size ratio $\Delta = 0.5$ ($r_2 = 1$ mm, $r_2 = 0.5$ mm) is investigated. The results are shown in Figure 12. This figure shows that the "coalescence" region becomes larger than that in Fig 10. The first reason is that the kinetic energy for separation and deformation is less than that of the case of $\Delta = 1.0$. In addition, for the stretching separation, it is more difficult for unequal-size drops to separate after the collision than two equal-size drops. This is because for the same impact parameter, the volume of non-interaction region is small when the size ratio is small, so the kinetic energy which contributes to stretching motion is also small.

4.4.2 Dependence on Viscosity

Figure 13 shows the numerical simulation results of $\mu_1 = 10$ poise and the other parameters are the same as Fig. 10. We can see that the region of "coalescence" is broader than that in Fig. 10. This is because the viscous dissipation at the interaction region is more effective.

4.4.3 Dependence on Size of Drops

Figure 14 shows the results of $d_1 = d_2 = 0.5$ mm and the other parameters are the same as Fig. 10. We can see that the region of "coalescence" is not so different from Fig. 10. In fact, the size dependence on the collision outcomes was not discussed in the experiments of the binary collision of water drops or some low viscous drops. For lower viscosities of drops, the viscous dissipation is less effective than the kinetic energy and the surface energy (Appendix

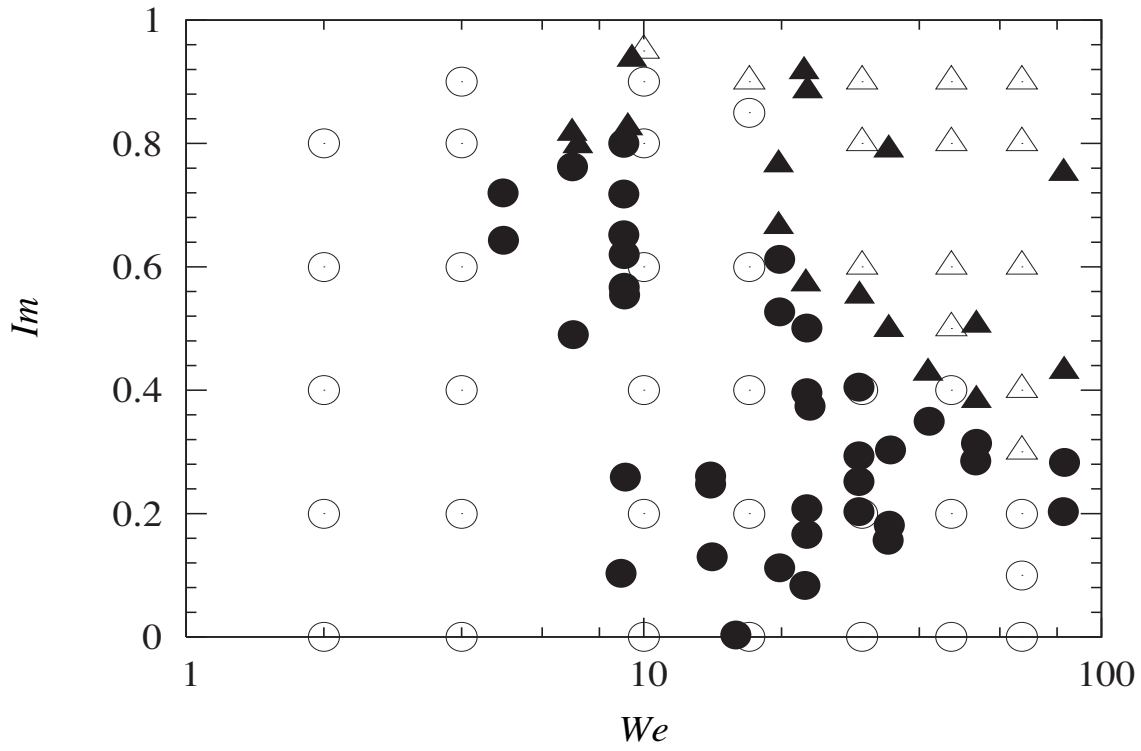

Figure 11: Comparison between the experiment of the binary collision of water drops (Ashgriz and Poo 1990) and our numerical simulations. The parameters are the same as Fig. 10. Filled circles and triangles represent the experimental results for "coalescence" and "stretching separation", respectively. Open circles and triangles represent the results of our numerical simulation (same result as Fig. 10). This diagram shows that our numerical simulation is good agreement with the experiments.

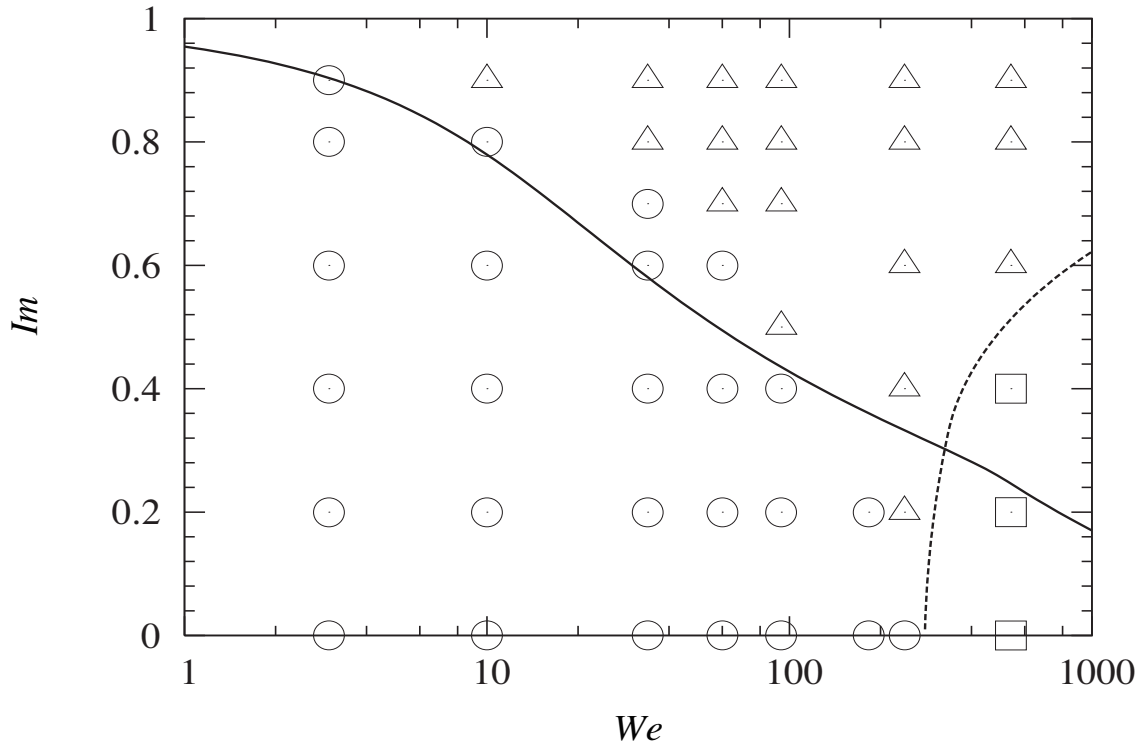

Figure 12: In the case of radius of the small drop is $d_1 = 0.5$ mm, that is, $\Delta = 0.5$. Other parameters are the same as Figure 10.

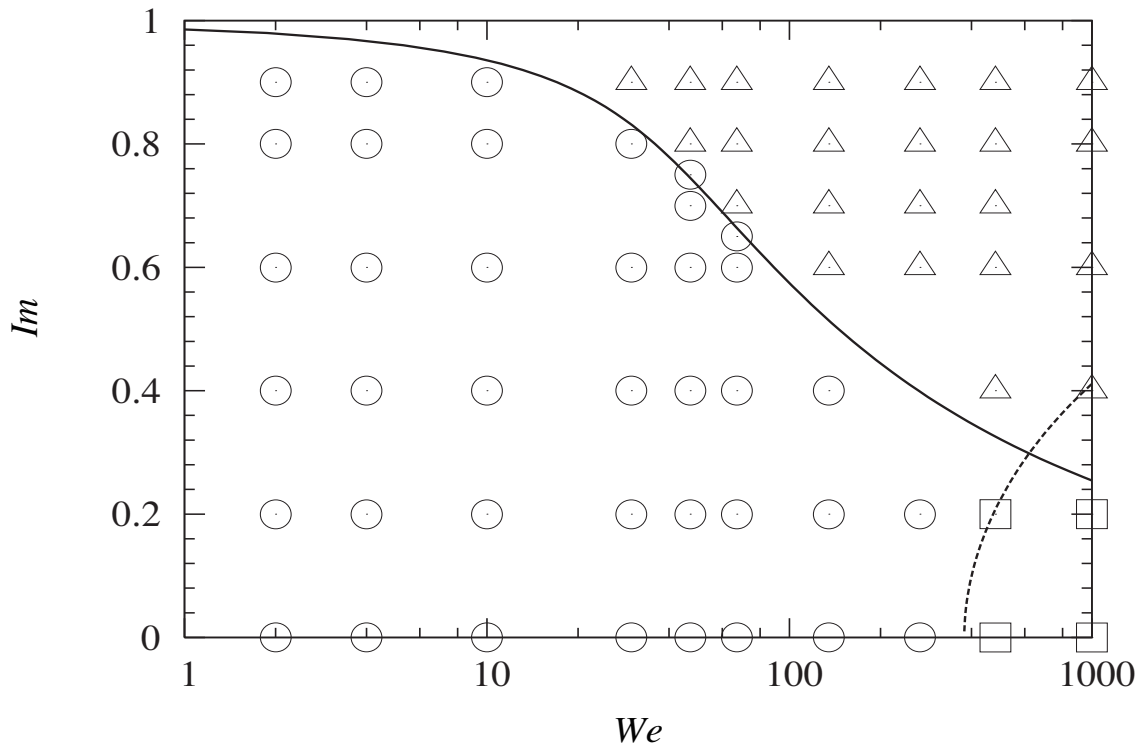

Figure 13: In the case of the viscosity of the small drop is $\mu_1 = 10$ poise. Other parameters are the same as Figure 10.

A). The kinetic energy is of the order of $K \sim \rho u^2 d^3$ (e.g., Eq. 20) and the surface energy is of the order of $S \sim \sigma d^2$ (e.g., Eq. 21). The boundary between "coalescence" and "stretching separation" can be approximately determined by $K = S$, so the critical relative velocity $u_{\rm crit}$ is proportional to $d^{-\frac{1}{2}}$. Therefore, the critical Weber number, which indicates the boundary between "coalescence" and "stretching separation" is

$$We_{\rm crit} \equiv \frac{\rho u_{\rm crit}^2 d}{\sigma} = const. \tag{14}$$

However, in the case where the viscosities of drops are more than 10 poise, we can see the size dependence in the collision outcomes. Figure 15 shows the results of $\mu_{\rm s} = 10$ poise and the other parameters are the same as the parameters of Fig. 12. The region of "coalescence" is broader than the case of Fig. 13. This is because, the velocity gradient is larger and the viscous dissipation is more effective when the diameters of drops are small. When the drops have large viscosities, the boundary is determined by the kinetic energy and the viscous dissipation $E_{\rm vis} \sim \mu d^3 \times u/d$. The boundary is estimated by $K = E_{\rm vis}$ (e.g., Eq. 22). So, the critical relative velocity is proportional to d^{-1} and the critical Weber number is also proportional to d^{-1}.

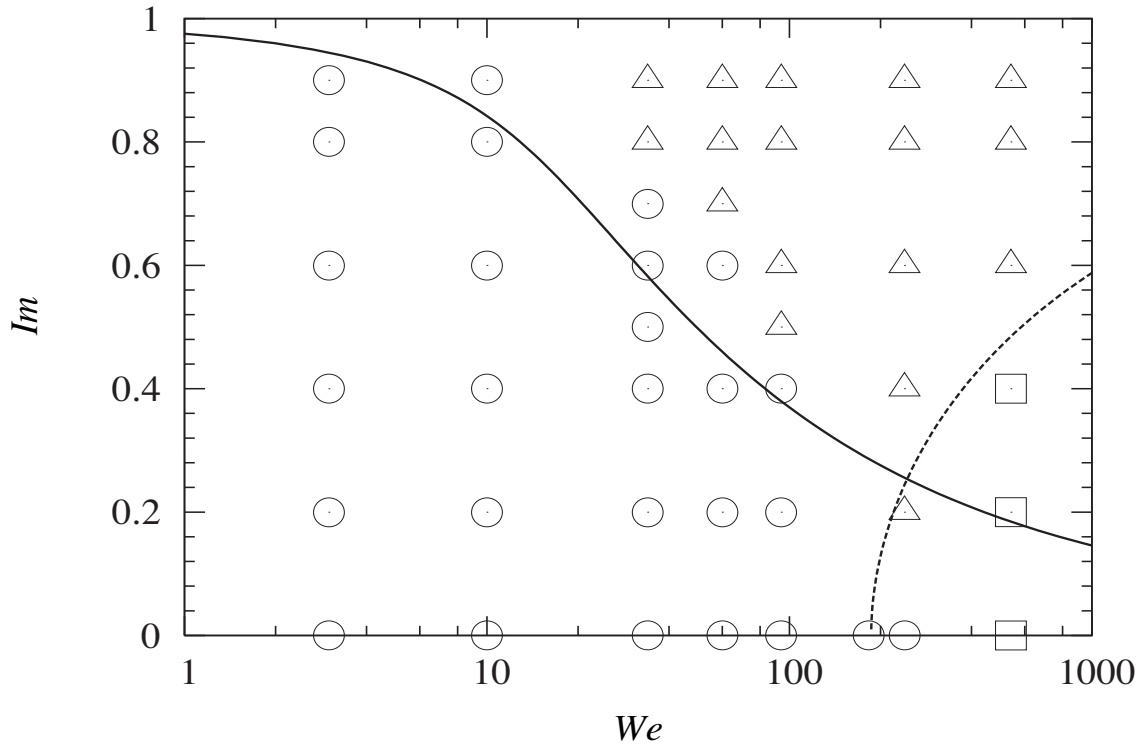

Figure 14: In the case of the radii of the drops are $d_1 = d_2 = 0.5$ mm. Other parameters are the same as Figure 10.

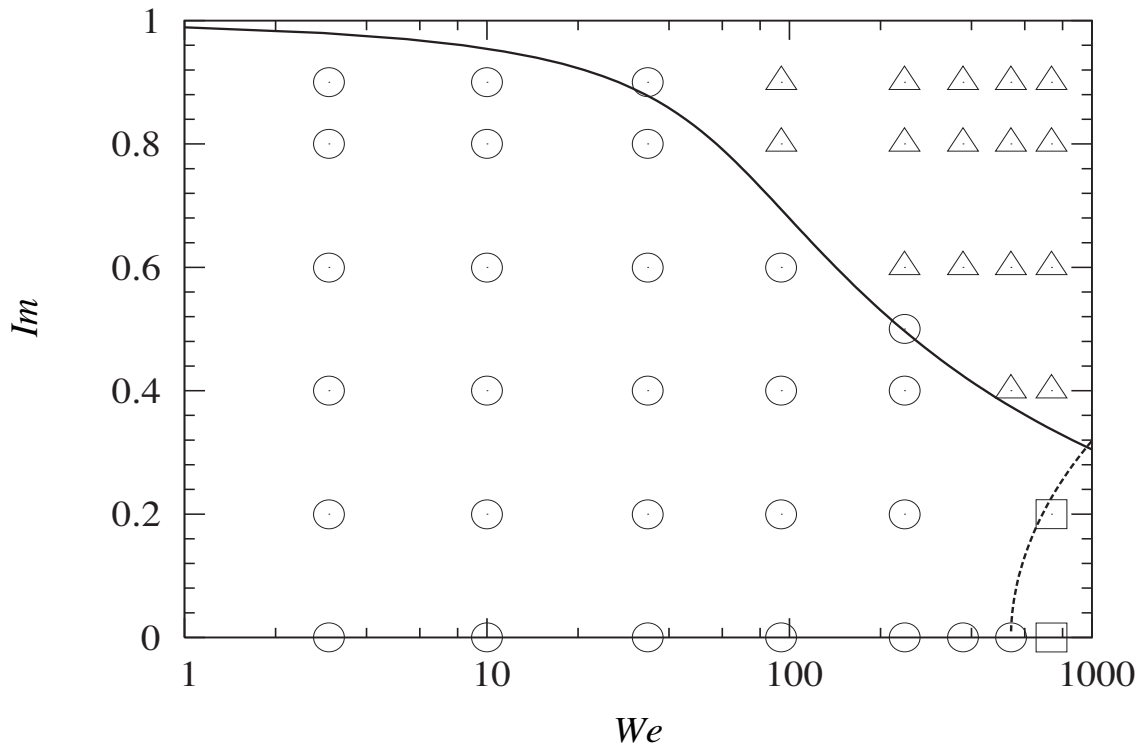

Figure 15: In the case of the viscosity of the small drop is $\mu_1 = 10$ poise. Other parameters are the same as Figure 12.

4.5 Boundary between Coalescence and Stretching Separation

In our numerical simulations, we found three categories of outcomes. In this subsection, we analyze the boundary between "coalescence" and "stretching separation" by considering an energy balance. The way of analysis is along the way of Ashgriz and Poo (1990). The "stretching separation" occurs when the stretching kinetic energy $K_{\rm str}$ overcomes energy dissipations due to the surface energy at the interaction region, the viscous dissipation of the drops, and the rotational energy, which is excited by the collision. It should be noted that the viscous dissipation was ignored in Ashgriz and Poo (1990) because they used water drops in their experiment. The viscosity of water drop ($\sim 10^{-2}$ poise) is much less than that of silicate drop, so the viscous dissipation was not effective for the energy dissipation (Appendix A). In addition, the rotational energy was not considered. It is true that the contribution of dissipation by the rotational energy is not so important in the parameter range of their experiment ($We \leq 100$) (Appendix A). However, the contribution of the dissipation by the rotational energy becomes important for larger Weber number cases because the dissipation by the rotational energy is proportional to u^2 (see Eq. 26).

Now, we consider the colliding two drops like figure 16. The stretching kinetic energy has two parts. One is the kinetic energy of the interaction region and the other is the remaining part of the total kinetic energy (Ashgriz and Poo 1990). And the stretching kinetic energy, $K_{\rm str}$, is given by

$$K_{\rm str} = \frac{1}{2}\rho\big((V_1 - V_{1\rm i})u_1^2 + (V_2 - V_{2\rm i})u_2^2\big) + \frac{1}{2}\rho\big(V_{1\rm i}(u_1\sin\theta)^2 + V_{2\rm i}(u_2\sin\theta)^2\big), \qquad (15)$$

where θ is the angle between the relative velocity vector and the center-to-center line at the time of collision (see Fig. 16), $\sin\theta = Im$, and u_1 and u_2 are the velocities of drops in the mass-center coordinates, respectively. They are given by

$$\begin{aligned} u_1 &= \frac{u}{1+\Delta^3}, \\ u_2 &= \frac{\Delta^3 u}{1+\Delta^3}. \end{aligned} \qquad (16)$$

And V_1, V_2, $V_{1\mathrm{i}}$, and $V_{2\mathrm{i}}$ are the volumes of the small drop, the large drop, the interaction part of the small drop, and that of the large drop, respectively. The volumes of the interaction regions are found from the following equations,

$$\begin{aligned} V_{1\mathrm{i}} &= \phi_1 V_1, \\ V_{2\mathrm{i}} &= \phi_2 V_2, \end{aligned} \tag{17}$$

where ϕ_1 and ϕ_2 represent the interaction rate and are defined as

$$\phi_1 = \begin{cases} 1 - \frac{1}{4\Delta^3}(2\Delta - \tau)^2(\Delta + \tau) & \text{for} \quad h > \frac{1}{2}d_1, \\ 1 & \text{for} \quad h \leq \frac{1}{2}d_1, \end{cases} \tag{18}$$

$$\phi_2 = \begin{cases} 1 - \frac{1}{4}(2 - \tau)^2(1 + \tau) & \text{for} \quad h > \frac{1}{2}d_2, \\ \frac{\tau^2}{4}(3 - \tau) & \text{for} \quad h \leq \frac{1}{2}d_2, \end{cases} \tag{19}$$

where $\tau \equiv (1 - Im)(1 + \Delta)$ and h is the width of the overlapping region, which is equal to the sum of the drop radii minus the impact parameter, $h = \frac{1}{2}(d_1 + d_2)(1 - Im)$ (Ashgriz and Poo 1990). Using equations (16) - (19), equation (15) can be written as

$$K_{\mathrm{str}} = \frac{1}{2}\rho u^2 V_2 \Big(\frac{\Delta^3}{(1 + \Delta^3)^2} \big((1 + \Delta^3) - (1 - Im^2)(\phi_1 + \Delta^3 \phi_2) \big) \Big). \tag{20}$$

This kinetic energy is dissipated at the interaction region and the rotation, which is excited by the collision. The surface energy, S, associated with the region of interaction is estimated as the surface energy associated with a cylinder with the same volume and with height l (Ashgriz and Poo 1990).

$$\begin{aligned} S &= 2\sigma \Big(\pi l (V_{1\mathrm{i}} + V_{2\mathrm{i}}) \Big)^{1/2} \\ &= \sigma \Big(2\pi V_2 d_2 \tau (\Delta^3 \phi_1 + \phi_2)) \Big)^{1/2}. \end{aligned} \tag{21}$$

The diffusion of the kinetic energy due to the viscosity, E_{vis}, is written as

$$\begin{aligned} E_{\mathrm{vis}} &= \frac{u}{h}(\mu_1 V_{1\mathrm{i}} + \mu_2 V_{2\mathrm{i}}) \\ &= \frac{u}{h}(\mu_1 \phi_2 V_2 + \mu_1 \phi_1 \Delta^3 V_2). \end{aligned} \tag{22}$$

The rotational energy, $E_{\rm rot}$, which is exited by the collision is written as

$$E_{\rm rot} = \frac{L^2}{2I}, \tag{23}$$

where L and I are the angular momentum and the moment of inertia given by

$$\begin{aligned} L &= \rho V_1 u_1 \frac{D}{2} \\ &= \frac{\rho \Delta V_2 u d_2 (1+\Delta) I m}{4(1+\Delta^3)}, \end{aligned} \tag{24}$$

and

$$I = \frac{2}{5}\rho V_2 \Big(\frac{d_2}{2}\Big)^2 (1+\Delta^3)^{\frac{5}{3}}. \tag{25}$$

We assume that the shape of the coalesced drop is spherical. Then, substituting equation (24) and equation (25) to equation (23), we obtain

$$E_{\rm rot} = \frac{5\rho V_2 \Delta^6 (1+\Delta)^2 I m^2 u^2}{16(1+\Delta^3)^{\frac{11}{3}}}. \tag{26}$$

The boundary between the "stretching separation" and "coalescence" is determined by assuming that the effective stretching kinetic energy is equal to the sum of the surface energy at the interactive region, diffusion due to the viscosity, and the rotational energy:

$$K_{\rm str} = S + E_{\rm vis} + E_{\rm rot}. \tag{27}$$

This condition is shown in Figs. 10, 12, 13, 14, and 15. We can see that our analytic model nicely expresses the boundary between "coalescence" and "stretching separation".

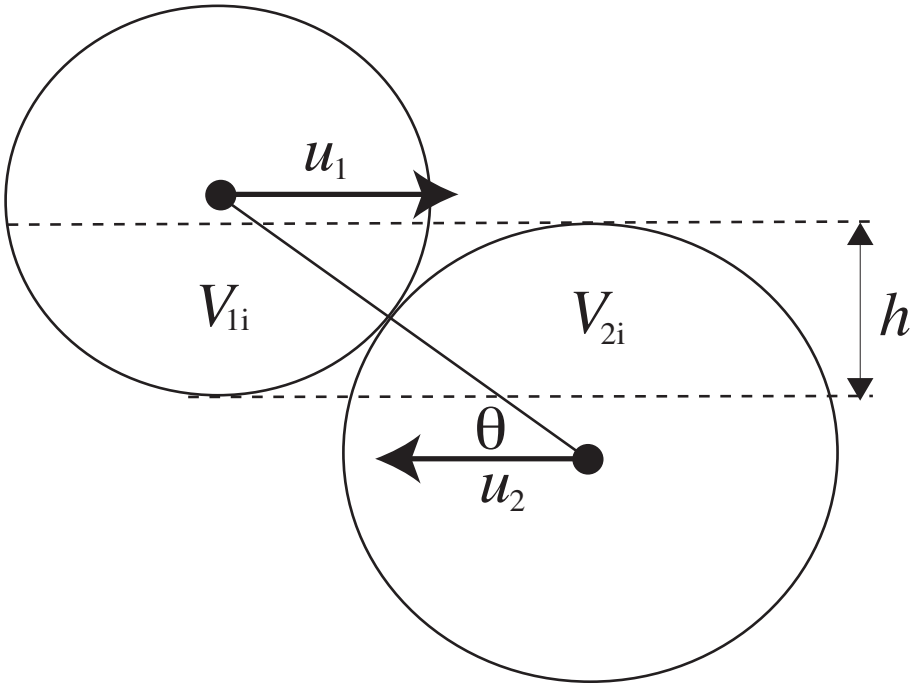

Figure 16: A schematic picture of collision of two drops.

4.6 Boundary between Coalescence and Disruption

In this subsection, we analyze the boundary between "coalescence" and "disruption" by considering the energy balance. As seen in subsection 4.1.3, "disruption" occurs when the discontinuity generates between the film and the circumference (we call this shape as the "critical shape" here in after). That is to say, "disruption" occurs when the kinetic energy for deformation exceeds the critical surface energy of combined drop $S_{\max}$. The kinetic energy for deformation can be expressed by,

$$K_{\rm def} = \frac{1}{2}\rho\big(V_{1\rm i}(u_1\cos\theta)^2 + V_{2\rm i}(u_2\cos\theta)^2\big). \tag{28}$$

Substituting equations (16) - (19) to above equation, we obtain

$$K_{\rm def} = \frac{1}{2}\rho V_2 u^2\Big(\frac{\Delta^3(1-Im^2)}{(1+\Delta^3)^2}\big(\phi_1+\Delta^3\phi_2\big)\Big). \tag{29}$$

This kinetic energy is dissipated by the viscous dissipation during its deformation. We assume that the viscous dissipation is given by

$$E_{\rm vis} = \alpha(\mu_1\frac{u}{d_1}V_1 + \mu_2\frac{u}{d_2}V_2), \tag{30}$$

where α is an adjustment factor. The velocity gradient changes significantly during its deformation from collision of two drops to torus-like structure. Thus it is difficult to express this phenomenon in an equation, so we assume above form as an approximation. Using equations (16) - (19), equation (30) can be written as

$$E_{\rm vis} = \alpha\frac{u}{d_2}V_2(\mu_2+\Delta^2\mu_1). \tag{31}$$

The increment of the surface energy, ΔS, which leads to "disruption", can be expressed by

$$\Delta S = S_{\max} - S_0, \tag{32}$$

where S_0 is the initial surface energy and can be written as

$$\begin{aligned} S_0 &= \sigma\pi(d_1^2+d_2^2) \\ &= \sigma\pi d_2^2(1+\Delta^2). \end{aligned} \tag{33}$$

And $S_{\max}$ can be obtained by our numerical simulation.

The boundary between the "coalescence" and "disruption" is determined by the energy balance,

$$K - E_{\text{vis}} = \Delta S. \tag{34}$$

This condition with $\alpha = 3$ is shown in Figs. 10, 12, 13, 14, and 15. We can see that our analytic model expresses the boundary between "coalescence" and "disruption" very well.

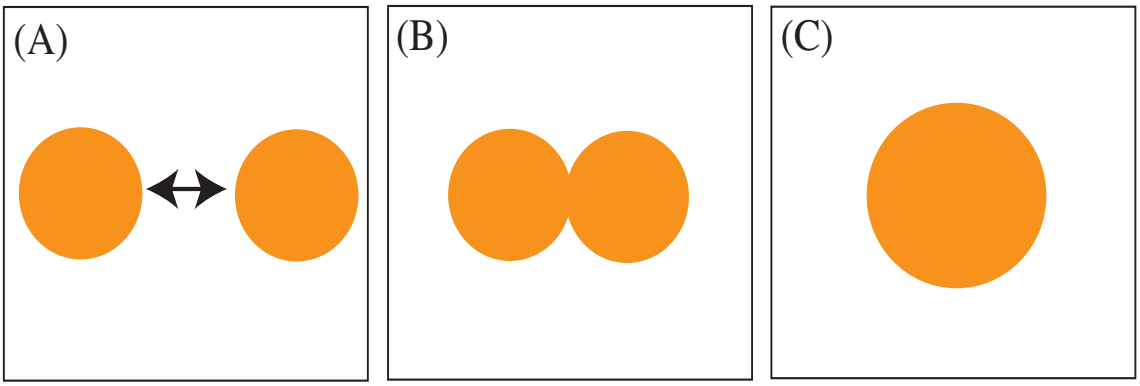

Figure 17: A schematic picture of evolution of colliding two drops. Panel (A) shows two drops before collision. After collision, the large drop that consists of two drops deforms toward equilibrium shape (panels B - C).

5 Condition for Keeping Shape

In this section, we examine the condition for keeping a shape. If the attached two drops deform before solidification, it may be difficult to form compound chondrules even if they coalesce. So we define the condition for keeping their shape as that the deformation time is longer than the solidification time. First, we examine the deformation time after collision in the "coalescence" cases by numerical simulation. Second, we estimate the solidification time from the theory of crystallization. And finally, we show the condition for keeping a shape comparing them.

5.1 Deformation Time

5.1.1 Surface Tension Control and Ram Pressure Control

After colliding two drops, they form a large drop and it deforms toward equilibrium shape over time by the ram pressure of the collision and/or the surface tension force (Figure 17). Once the large drop reaches equilibrium shape, i.e., a sphere, it may be difficult to form compound chondrules, so we define the deformation time as the time from just after the collision (Fig. 17B) to reaching the equilibrium shape (Fig. 17C).

Solid line in Figure 18 shows the deformation time for the head-on collision case as the function of the Weber number. The deformation time is constant for the lower Weber number (lower relative velocity). On the contrary, for the higher Weber number, the deformation time shortens as the Weber number increases. We can see the same trend for other impact parameters. Figure 19 shows the deformation time for various Weber number and impact parameter. The number above symbols show the deformation time. We can categorize coalescence region into two regions; in a region, the deformation time is constant (square) and in the other region, the deformation time shortens as the Weber number increases (circle). Deformation of the large drop is controlled by the ram pressure of collision and/or the surface tension force. In the higher Weber number region (circle), the ram pressure mainly controls the deformation. We call this region as "ram pressure control" case in this study. In this case, the deformation time is approximately expressed by the crossing time of the large drop, that is,

$$t_{\mathrm{def}} = \frac{d_2}{u \cos\theta}. \tag{35}$$

The dashed line in Fig. 18 shows the deformation time expressed by equation (35). This line shows a good agreement with the numerical simulation at higher Weber number. In the lower Weber number region (square), the surface tension force mainly controls the deformation. We call this region as "surface tension control" case. In this region, two drops attach gently and form a larger drop whose shape is like Fig. 17 (B). Because the surface energy of the larger drop is more than that of equilibrium shape (sphere), it is gradually deformed by the surface tension force, so the deformation time is constant in this region. However, it is noted that the timescale strongly depends on the viscosities of two drops.

5.1.2 Deformation Time in Surface Tension Control Cases

The deformation time in the surface tension control case depends on the viscosities of two drops. Figure 20 shows the deformation time for various viscosities of drops in the surface tension control case. The horizontal and vertical axes represent the viscosities of the two

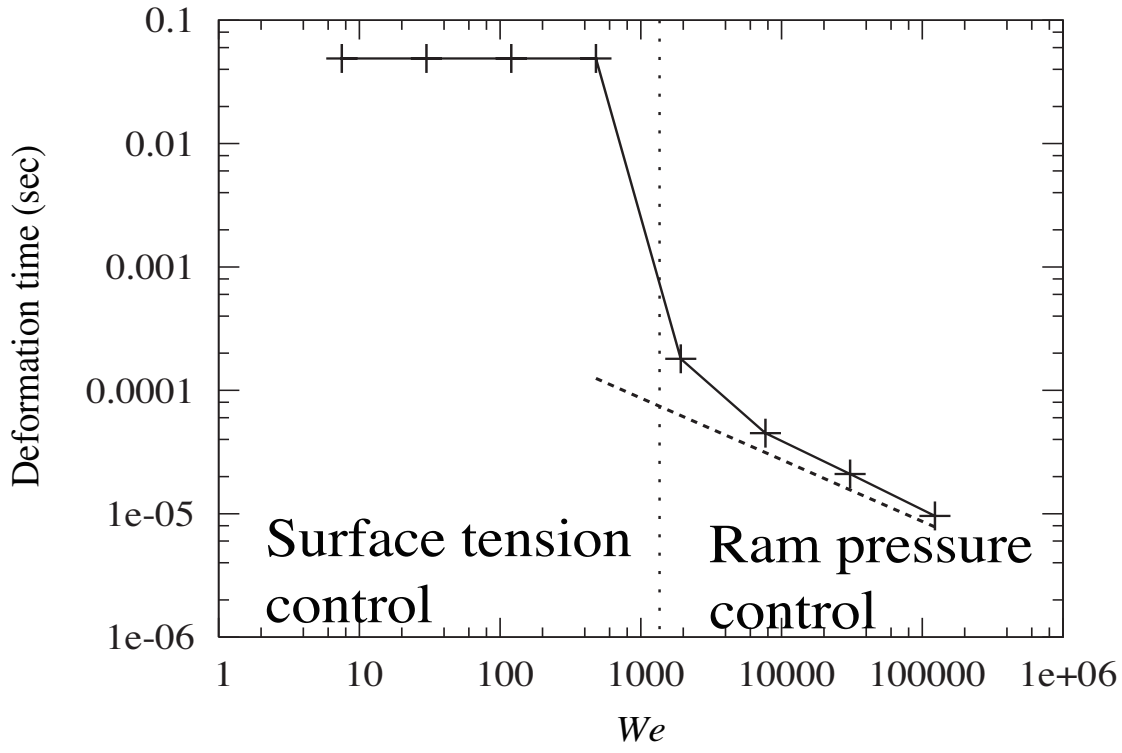

Figure 18: The deformation time for the head-on collision ($Im = 0$) case. The horizontal axis represents the Weber number. Parameters are $d_1 = d_2 = 1$ mm, $\mu_1 = 1000$ poise, and $\mu_2 = 10$ poise. The solid line shows the deformation time obtained by numerical simulations, the dashed line shows the analytic line $t = d_2/u\cos\theta$, and the dotted line shows the boundary between the surface tension control cases and the ram pressure control cases.

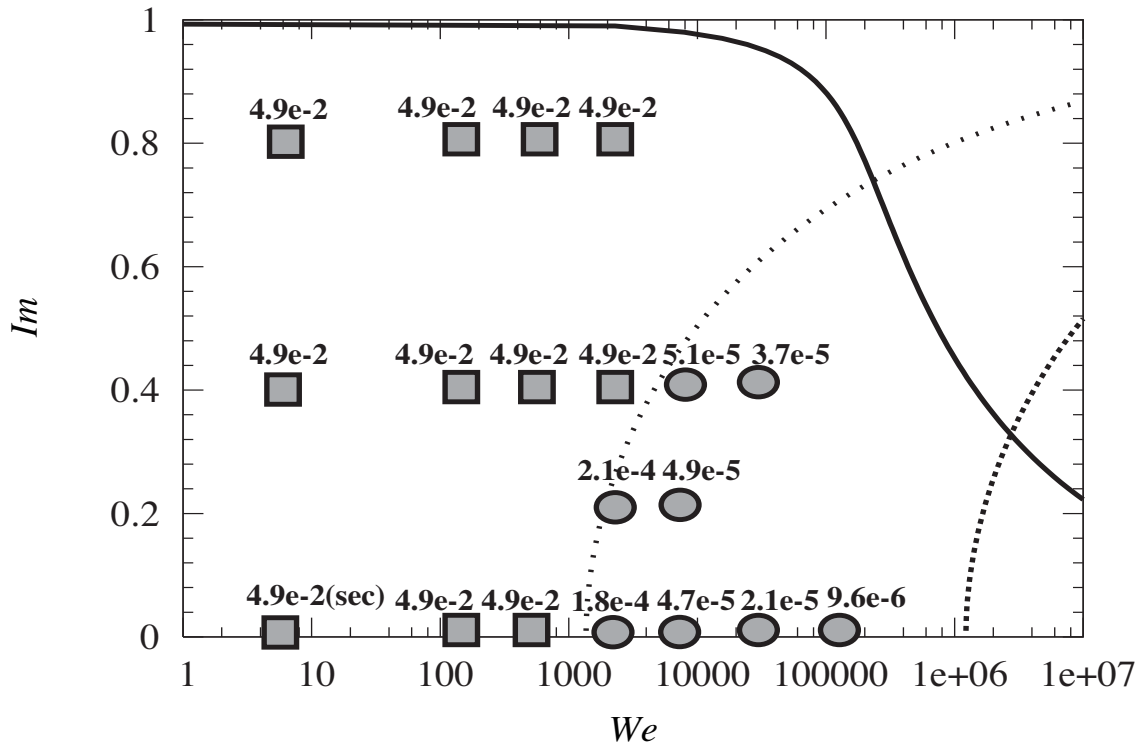

Figure 19: The deformation time as a function of the Impact parameter and the Weber number. Other parameters are the same as Fig. 18. The solid curve shows the boundary between "coalescence" and "stretching separation". The dashed curve shows the boundary between "coalescence" and "disruption". The symbols square (□) and circle (◯) represent the surface tension control case and the ram pressure control case, and the dotted line shows the boundary of them, respectively.

drops. The diameters of the drops are 1 mm. We can see that when the viscosities of the drops are low, the deformation time does not depend on the viscosities. On the contrary, when the viscosities of drops are high, the deformation time is proportional to the viscosities. This trend can be understood using a damped oscillation model.

First, let us consider two inviscid drops. After a collision of the two drops, a large drop formed by two drops oscillates around the equilibrium shape like figure 21. We can regard this phenomena as the oscillation of an elastic body and can be modeled by a free oscillation of a spring (Figure 22A). The deformation time can be expressed by about a quarter of the period of free oscillation from our definition (this corresponds to the deformation from Fig. 21A to Fig. 21B). The frequency and the period of free oscillation can be estimated by linear analysis as,

$$\begin{aligned} \omega_{\rm osc} &= \Big(\frac{64\sigma}{\rho d^3}\Big)^{\frac{1}{2}}, \\ T_{\rm osc} &= \frac{1}{\omega_{\rm osc}} = 4.8\times10^{-4}\ {\rm sec}\Big(\frac{d}{1.26\ {\rm mm}}\Big)^{\frac{3}{2}}, \end{aligned} \tag{36}$$

where d is the diameter of the large drop (Chandrasekhar 1959).

The oscillation of the large viscous drop is damped by viscous dissipation. We can regard the oscillation of the large viscous drop as the oscillation of a viscoelastic body and can be modeled by a spring and a dashpot, which generates the drag force proportional to the velocity (Fig. 22B). The equation of motion is given by,

$$\frac{d^2x}{dt^2} = -\omega_{\rm osc}^2 x - 2\lambda\frac{dx}{dt}, \tag{37}$$

where x and λ are the displacement from the equilibrium point and the coefficient of damping, respectively. On the other hand, the equation of motion of the large drop of the interaction region is given by

$$\rho\frac{dv}{dt} = F_{\rm s} + \mu_{\rm e}\frac{d^2v}{dx^2}. \tag{38}$$

This equation is approximately written as

$$\frac{dv}{dt} \sim \frac{F_{\rm s}}{\rho} - \frac{\mu_{\rm e}v}{\rho r^2}, \tag{39}$$

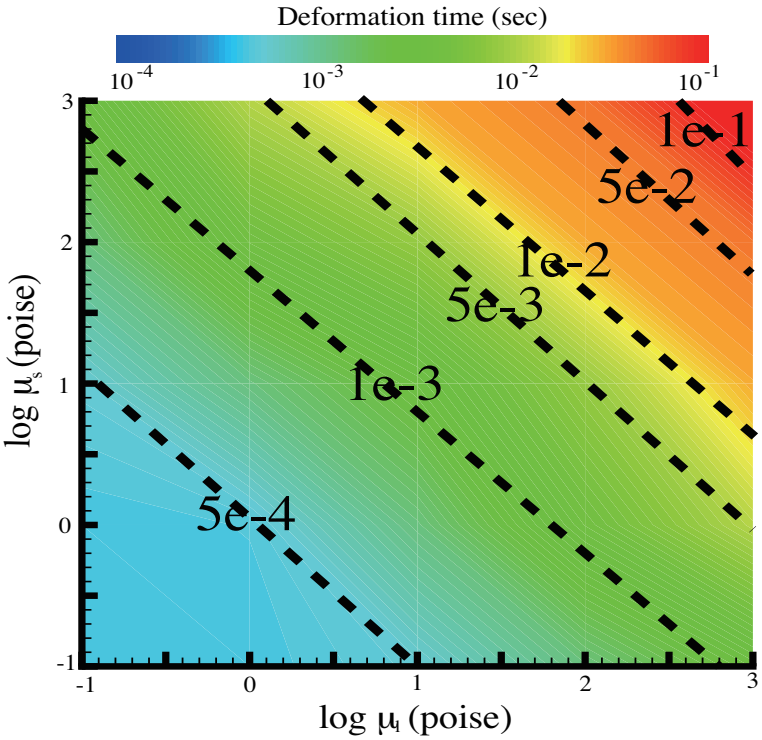

Figure 20: The deformation time in the surface tension control case. The horizontal and the vertical axes show the viscosities of two drops. The diameters of two drops are 1 mm. The color contour shows results of our numerical simulation and the dashed lines show results of analytical estimation. They show a very good agreement.

where F_s, r, and μ_e are the surface tension force, the radius of the drop, and the viscosity of the interaction region, respectively. From our viscosity model (Eq. 6), the viscosity of the interaction region can be approximately expressed by $\mu_e \sim \sqrt{\mu_1 \mu_2}$. From Eqs. (37) and (39), the coefficient of damping λ corresponds to the term of $\mu_e / 2\rho r^2$. The period of the oscillation can be written by

$$T = \begin{cases} (\omega_{osc}^2 - \lambda^2)^{-\frac{1}{2}} & \text{for } \lambda < \omega_{osc} \text{ (damped oscillation),} \\ (\lambda + \sqrt{\lambda^2 - \omega_{osc}^2})^{-1} & \text{for } \lambda \geq \omega_{osc} \text{ (over damping).} \end{cases} \tag{40}$$

The deformation time (a quarter of the period of the large drop) from our analysis is expressed by the dashed lines in Fig. 20.

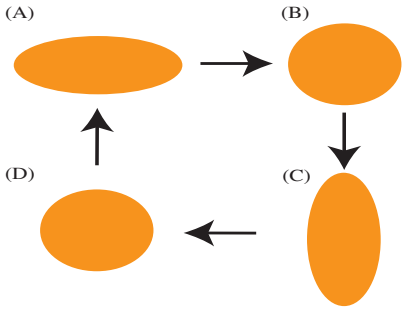

Figure 21: A schematic picture of an oscillating drop.

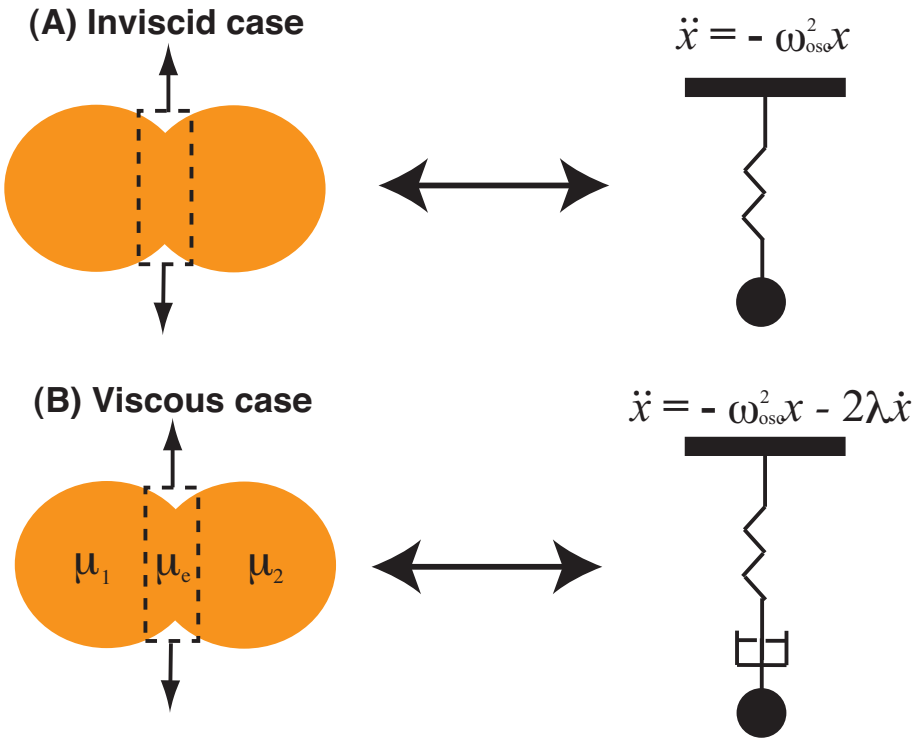

Figure 22: A schematic picture of an oscillating drop. The dynamics of the interaction region can be modeled by the free oscillation (the inviscid case) and the damped oscillation (the viscous case).

5.1.3 Boundary between Surface Tension Control and Ram Pressure Control Cases

In this subsection, we analyze the boundary between the surface tension control cases and the ram pressure control cases by considering an energy balance. The deformation is controlled by the ram pressure of the collision when the kinetic energy for the deformation overcomes the viscous dissipation. The kinetic energy for deformation is written by (same as Eq. 29).

$$K_{\rm def} = \frac{1}{2}\rho V_2 u^2 \Big(\frac{\Delta^3(1-Im^2)}{(1+\Delta^3)^2} \big(\phi_1 + \Delta^3 \phi_2\big) \Big). \tag{41}$$

This kinetic energy is dissipated by the viscous dissipation when two drops collide. We assume that the viscous dissipation is written as

$$E_{\rm vis} = \beta \frac{u}{d_2} V_2 (\mu_2 + \Delta^2 \mu_1), \tag{42}$$

where β is an adjustment factor. While we adopt the velocity gradient as u/d_1 or u/d_2, actually, they change with time. We calculate the mean value of the velocity gradients and obtain $\beta \sim 0.1$ in all the cases. The boundary between the surface tension control cases and the ram pressure control cases is determined as that the kinetic energy is equal to the viscous dissipation:

$$K = E_{\rm vis}. \tag{43}$$

This condition with $\beta = 0.1$ is superimposed on our calculation results, Figs. 18 and 19. We can see that our analytic model nicely expresses the boundary between the ram pressure control cases and the surface tension control cases.

5.2 Discussions

5.2.1 Coverage of Numerical Simulation

In this subsection, we consider the coverage of our numerical simulation. If the viscosities of the drops are too high, they would behave as the solid instead of the liquid. In this case, we cannot simulate the collision of two drops rightly, because the right hand side of the equation of motion does not have terms that describe the solid feature.

Now, we consider the situation that we keep on adding the strain to a body. When the body is an elastic body (solid), the stress is constant with time. The elastic body can be modeled by a spring (Fig. 23a). The relation between the stress (σ) and the strain (ε) can be written by

$$\sigma = E\varepsilon, \tag{44}$$

where E is the Young's modulus (Hooke's law). On the contrary, when the body is a viscous body (liquid), the stress approaches 0 immediately. The viscous body can be modeled by a dash pot (Fig. 23b). The relation between the stress and the strain can be written by

$$\sigma = \eta \frac{d\varepsilon}{dt}, \tag{45}$$

where η is the coefficient of viscosity (Newton's law). When the body is viscoelastic, the stress approaches 0 with time. The viscoelastic body can be modeled by a spring and a dash pot connected in series (Maxwell model). The relation between the stress and the strain can be calculated by Eqs. (44) and (45),

$$\sigma + \frac{\eta}{E}\frac{d\sigma}{dt} = \eta \frac{d\varepsilon}{dt}. \tag{46}$$

The solution of the Eq. (46) is

$$\sigma(t) = \sigma_0 \exp\Big(-\frac{t}{\tau_{\rm r}}\Big), \tag{47}$$

where $\tau_{\rm r} = \eta/E$ is the relaxation time of the stress. The viscoelastic body behaves as the solid when the timescale of a phenomena is shorter than the relaxation time, while it behaves as the liquid when the timescale of a phenomena is longer than the relaxation time.

Now, we estimate the coverage of our numerical simulation. As shown in the previous section, the deformation after a collision of two drops can be modeled by the viscoelastic body. Then the relaxation time is

$$\tau_{\rm r} \sim 10^{-11}\ {\rm sec}\Big(\frac{\mu_{\rm e}}{1\ {\rm poise}}\Big)\Big(\frac{E}{10^{11}\ {\rm dyn\ cm^{-2}}}\Big)^{-1}. \tag{48}$$

The characteristic timescale of the drop collision can be estimated from the crossing time of

two drops as

$$t_{\rm p} \sim \frac{r}{\Delta v} = 10^{-3}\ {\rm sec}\Big(\frac{r}{1\ {\rm mm}}\Big)\Big(\frac{\Delta v}{100\ {\rm cm\ s^{-1}}}\Big). \tag{49}$$

When the relative velocity is too high and/or the viscosities of two drops are too high, the timescale of collision is shorter than that of the relaxation.

5.2.2 Solidification Time

In this subsection, we estimate the solidification time of the large drop in order to compare with the deformation time obtained from the previous subsection. We should note that the solidification time does not always correspond to the cooling time of the large drop. According to the crystallization experiments under the levitated condition, homogeneous nucleation is very difficult for the forsterite (Mg_2SiO_4) and the enstatite ($MgSiO_3$);(Nagashima et al. 2006). They concluded that the onset of crystallization was triggered by heterogeneous nucleation, which occurs due to the collision with small dust particles. The crystallization processes would depend on the temperatures of the drops, the relative velocity, the geometry of the interaction region, and so on. Unfortunately, the crystallization processes by the collision have not been understood well yet. We should estimate the feasible solidification time in the future. Thus we estimate here the solidification times for heterogeneous nucleation as the lower limit of the solidification time.

We assume that the seed of crystal occurs by collision at the interaction region, the crystal grows through the large drop, and the large drop solidifies (see Fig. 24). In this case, the solidification time can be interpreted as the crossing time of the crystal growth through the large drop, which is given by

$$t_{\rm sol} = \frac{r}{da/dt}, \tag{50}$$

where r and a represent the size of the small drop and the size of crystal, respectively. The growth rate of crystal depends on the temperature of the drop (Kouchi et al. 1994),

$$\frac{da}{dt} = D_0 \exp\{-\frac{E_{\rm a}}{kT}\}\Big(1 - \exp\{-\frac{q_{\rm l}(T - T_{\rm e})}{kT^2}\}\Big), \tag{51}$$

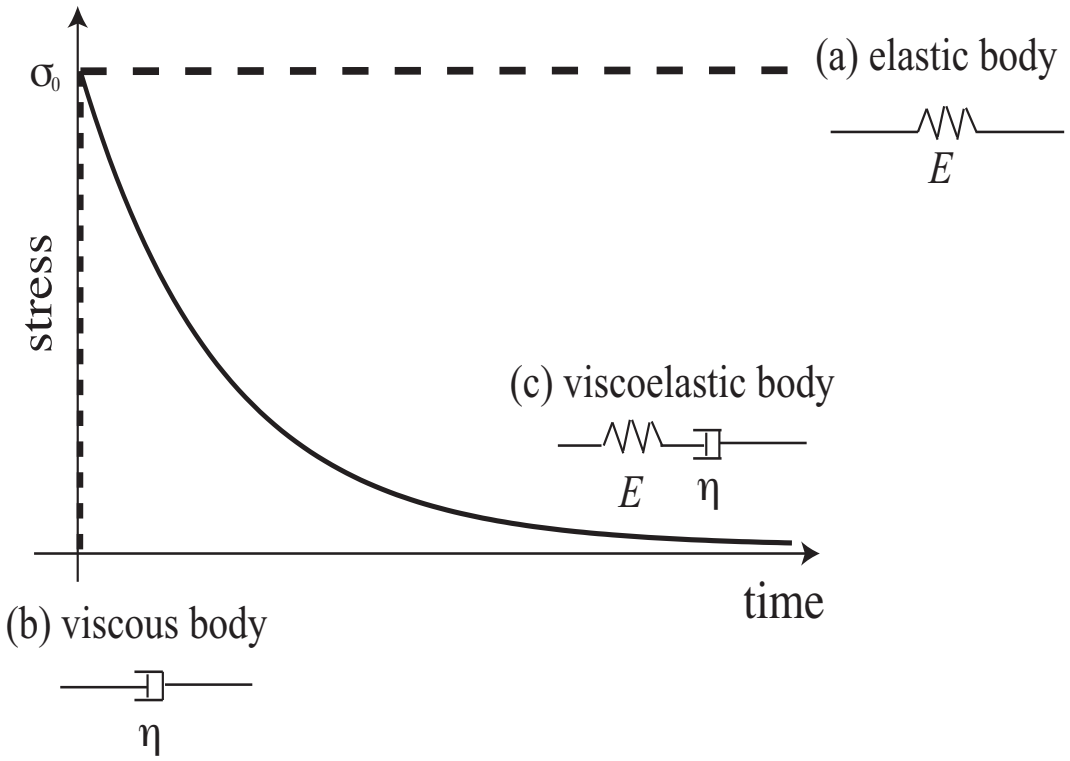

Figure 23: The time evolution of the stress of an elastic body, a viscous body, and a viscoelastic body being added the constant strain to a body. For the elastic body, the stress is constant (the dashed line)and it can be modeled by a spring. For the viscous body, the stress approaches 0 immediately and it can be modeled by a dash pot (the dotted line). And for the viscoelastic body, the stress approaches 0 with time (the solid curve) and it can be modeled by a spring and a dash pot connected in series.

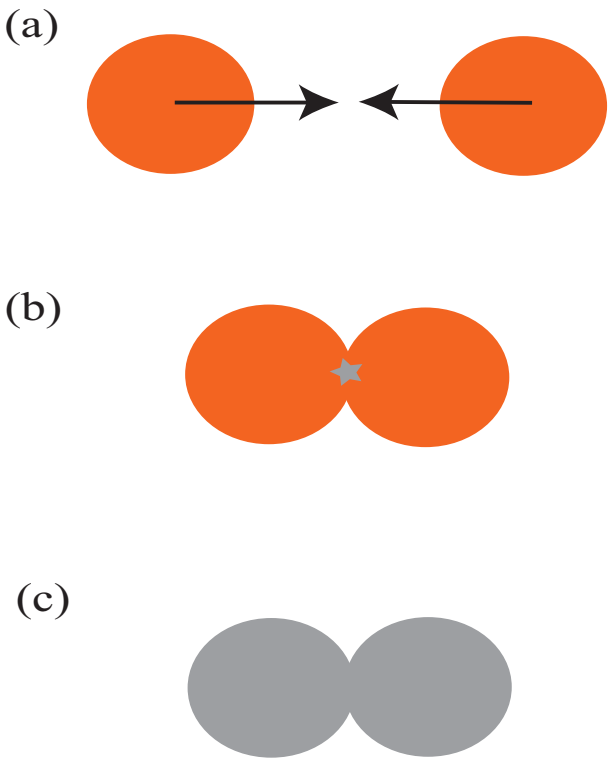

Figure 24: A schematic picture of solidification of the drop for heterogeneous nucleation. We assume that the seed of crystal (marked star in panel b) is formed just after the collision.

where D_0, E_a, q_l and T_e are the surface diffusion velocity, the activation energy, the latent heat, and the melting temperature, respectively. Figure 25 shows the nucleation time for forsterite ($D_0 = 8.2 \times 10^5$ cm s^{-1}, $E_a/k = 23000$ K, $q_l/k = 13800$ K, $T_e = 2163$ K; Tanaka et al. 2008). In the vicinity of the melting point, the growth rate increases as the temperature increases due to the latent heat. For the other case, the solidification time shortens as the temperature increases because the number of molecules that exceed the activation energy increases for higher temperature.

5.2.3 Condition for Keeping Shape in Ram Pressure Control Cases

Now, we compare the solidification time with the deformation time in the ram pressure control case. Fig. 26 shows the solidification time for forsterite (the solid curve) and the maxi-

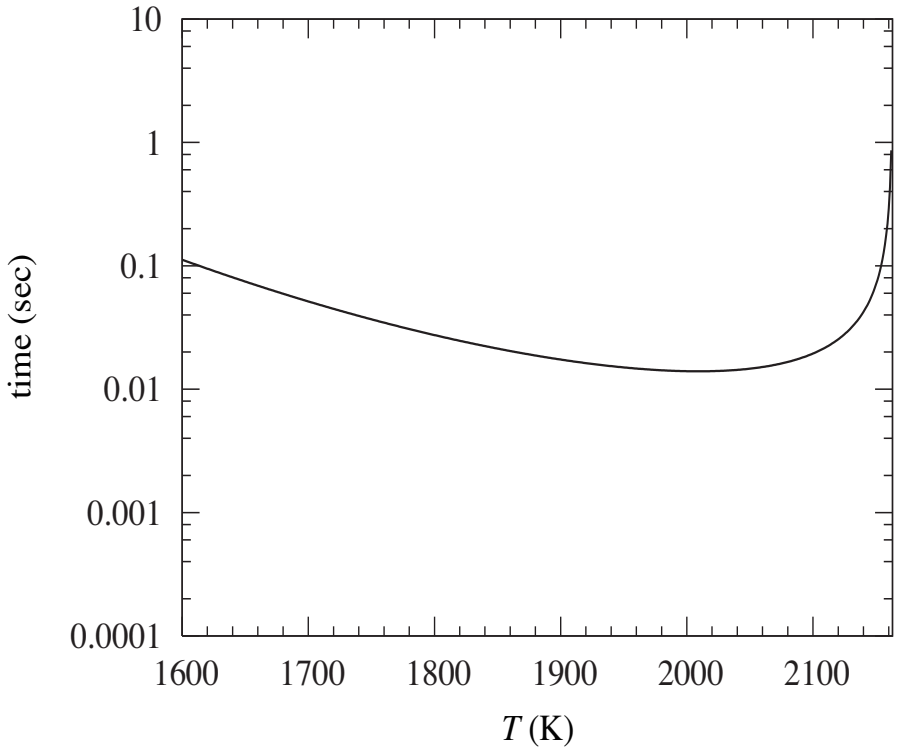

Figure 25: The solidification time for forsterite (Mg_2SiO_4).

mum deformation time in the ram pressure control case (the dashed curve). The horizontal axis shows the viscosity of one drop that has a larger viscosity, that is $\mu_{\rm m} = \max(\mu_1, \mu_2)$. We use the relationship between the viscosity and the temperature of magma (Shaw 1972) in order to compare two times,

$$\mu = \exp\{A\Big(\frac{E_{\rm a}}{kT} - 1.5\Big) - 8.7\}(1-\Phi)^{-2.5}, \tag{52}$$

where A is the coefficient of the chemical composition and in our case, A = 0.86. And Φ represents the volume fraction of the phenocryst and air bubble. The solidification time is longer than the deformation time at every viscosity. Therefore, the condition for keeping shape is not satisfied in the ram pressure control case. In the case of enstatite, the solidification time is much longer than that of forsterite (Nagashima et al. 2006). Moreover, the homogeneous nucleation time is also much longer. Thus it seems to be difficult to form compound chondrules in the ram pressure control case.

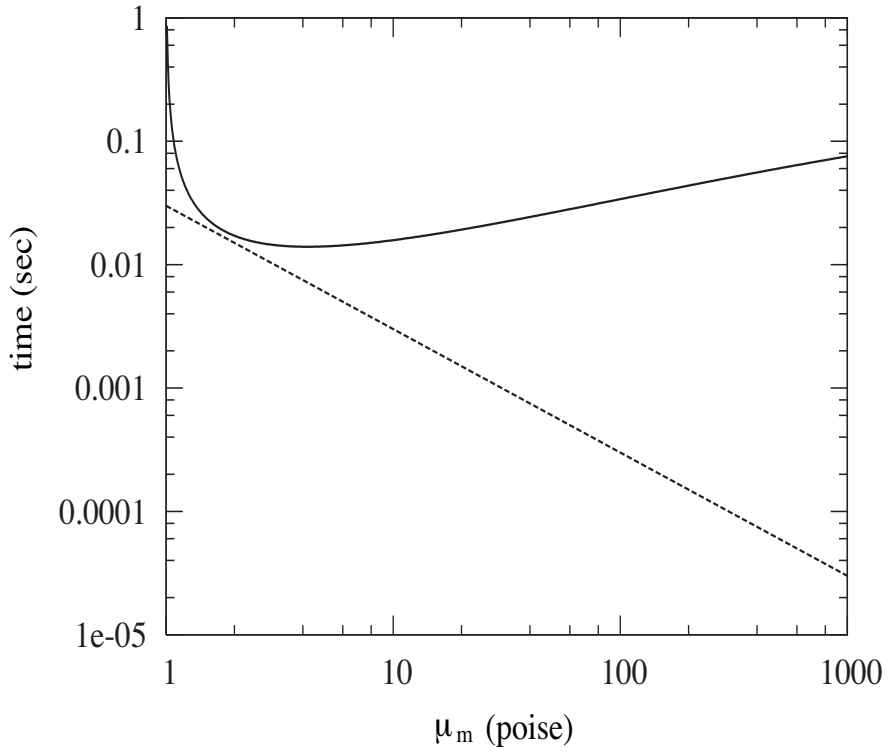

Figure 26: The solidification time (solid curve) and the maximum deformation time (dashed curve) in the ram pressure control case. The solidification time is longer than the deformation time at every viscosity.

5.2.4 Condition for Keeping Shape in Surface Tension Control Cases

Figure 27 shows the comparison of the solidification time for forsterite (solid curve) with the deformation time in the surface tension control case (dashed curve) when the viscosities of the two drops are the same. The diameters of the drops are 1 mm. It should be noted that the solidification time is a function of $\mu_{\rm m}$. On the other hand, the deformation time is a function of the viscosity of the interaction region $\mu_{\rm e}$. When the two drops have the same viscosities, $\mu_{\rm m} = \mu_{\rm e}$. In the grey region ($\mu_{\rm m} = \mu_{\rm e} > 330$ poise), the deformation time is longer than the solidification time and the condition for keeping shape is satisfied. Figure 28 shows the deformation time and the solidification time for various viscosities of two drops. In the grey region, the deformation time is longer than the solidification time. As noted, this solidification time that we compare with the deformation time is the lower limit. Therefore, in order to satisfy the condition for keeping shape, the collision should be the surface tension control case and the viscosities of the two drops are, at least, larger than about 330 poise.

While we obtain the lower limit of the condition for keeping shape, we should obtain a feasible condition when we can estimate the feasible solidification time in the future.

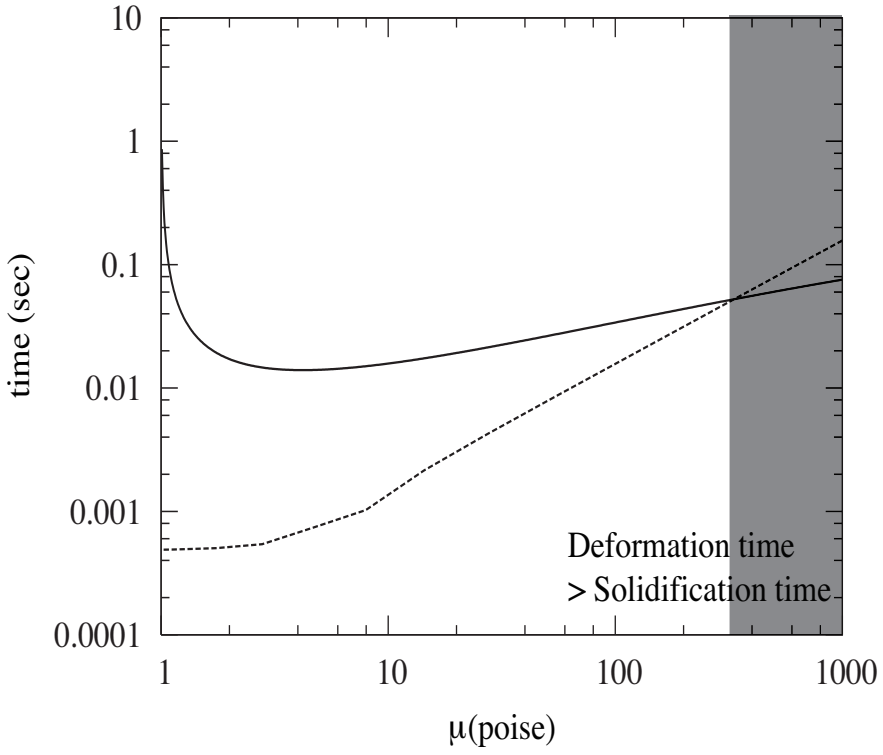

Figure 27: The solidification time (solid curve) and the deformation time (dashed curve) for the same viscous drops as a function of the viscosity. In the grey region, the deformation time is longer than the solidification time and the condition for keeping shape is satisfied.

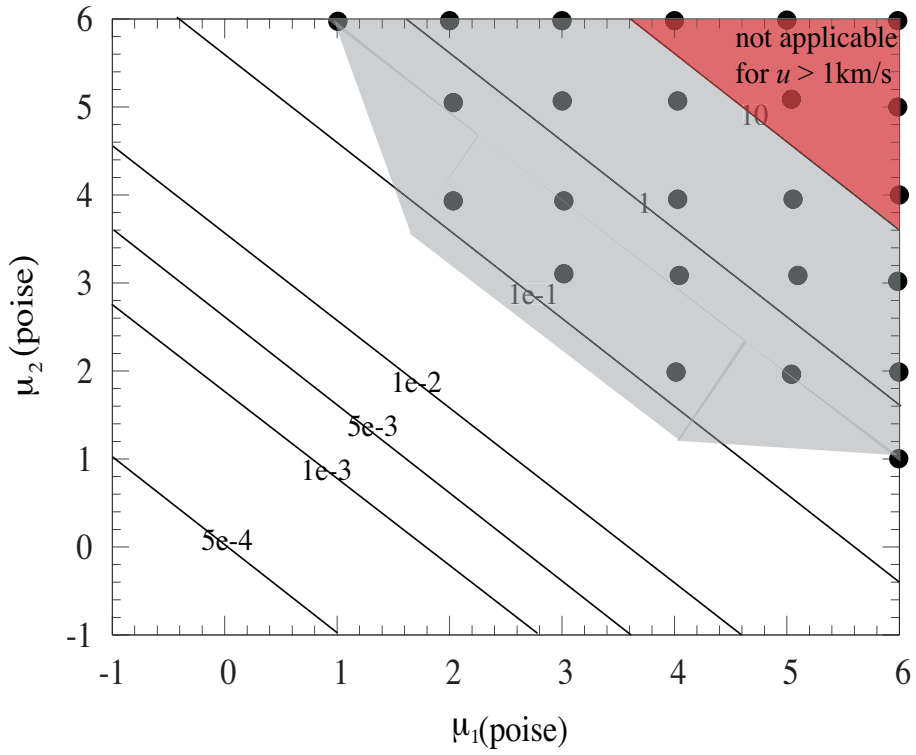

Figure 28: The condition for keeping shape. The horizontal and vertical axes are viscosities of the two drops. The solid lines show the contour of the deformation time estimated in subsection 5.1. The grey region shows the condition for keeping shape, that is, the deformation time is larger than the solidification time. In the red region, our numerical simulation is not applicable because the relative velocity is larger than 1 km s^{-1}.

6 Summary of Part I

We simulated two silicate drop collisions for various collision parameter, such as the collision velocity, the collision angle, the diameters, and the viscosities of the drops, with three-dimensional hydro-dynamics simulation in order to examine collision conditions for compound chondrule formation. The collision conditions are composed of two conditions; "condition for coalescence" and "condition for keeping shape".

We have found that collision outcomes can be classified into three categories; "coalescence", in which the two drops fuse together, "stretching separation", in which while the two drops coalesce once, they separate eventually, and "disruption", in which a large drop consisted of the two drop disrupts into some fragments.

We have understood the condition for coalescence with the energy balance. The boundary between "coalescence" and "stretching separation" can be obtained from the balance between the kinetic energy which tends to separation of two drops and the energy dissipations, such as the surface energy of the interaction region, the viscous dissipation, and the rotation energy. The boundary between "coalescence" and "disruption" can be obtained from the balance between the kinetic energy which tends to deformation of a large drop consisted of the two drops and the increment of the surface energy which leads to the disruption.

It is important for compound chondrule formation to solidify the large drop before deformation. Thus, the deformation time should be longer than the solidification time. First, we investigated the deformation time of the large drop with hydro-dynamics simulation.

The deformation is controlled by the ram pressure of the collision and the surface tension. When the relative velocity is high, the deformation is mainly controlled by the ram pressure of the collision (ram pressure control) and the deformation time can be interpreted as the transit time of the two drops. On the contrary, when the relative velocity is low, the deformation is mainly controlled by the surface tension (surface tension control) and the deformation time depends on the diameters and the viscosities of the two drops. The dynamics of the large drop can be modeled by a viscoelastic body and the deformation time in surface tension

control case can be written by a quarter of the damped oscillation period. The boundary between these two cases can be obtained from the balance between the kinetic energy which tends to deformation and the viscous dissipation just after collision.

The solidification time is difficult to estimate because the crystallization processes by collision have not been understood well. In this study, we assumed that the seed of the crystal occurs at the interaction region and defined the solidification time as the growth time of crystal, which is the lower limit of the solidification time. Then, we compared it with the deformation time.

In the ram pressure control case, the deformation time is longer than the solidification time for every viscosity. It is difficult to form compound chondrule by the collision in the ram pressure control case. In the surface tension control case, the deformation time is longer than the solidification time for more than about 330 poise. Therefore, we found that in order to satisfy the condition for keeping shape, the collision should be the surface tension control case and the viscosities of the two drops are, at least, larger than about 330 poise. We would obtain a feasible condition when we can estimate the feasible solidification time in the future.

Now, we have obtained the collision conditions for compound chondrule formation quantitatively. Since we have analytically understood the phenomena of drop collisions, we can know the conditions without using numerical simulations for a wide range of collision parameters and verify compound chondrule formation models from the view point of the collision conditions.

Part II

Verification of Fragment-Collision Model in the Shock-Wave Heating Model

7 Introduction

Chondrules are mm-sized, spherical-shaped, silicate particles abundant in chondritic meteorites. They are thought to have been formed from dust particles heated by some flash heating events; they were melted and rounded by the surface tension, and cooled again in the early solar nebula. There are three viable heating models; lightning, X-wind model, and shock-wave heating model (e.g., Jones et al. 2000). In this part, we focus on the shock-wave heating model. In the shock-wave heating model, dust particles are exposed to the high-speed gas flow behind the shock front and heated by the gas frictional heating. Many researchers investigated the thermal evolution of chondrules in pre- and post-shock regions by using numerical works (Hood and Horanyi 1991, 1993; Ruzmakina and Ip 1994; Tanaka et al. 1998; Hood 1998; Iida et al. 2001; Desch and Connolly 2002; Ciesla and Hood 2002; Miura et al. 2002; Miura and Nakamoto 2005, 2006). From these simulations, the shock conditions appropriate for the chondrule formation have been revealed by comparing with the observational constraints (Jones et al. 2000). However, some unsolved mysteries still remain. One of them is the formation mechanism of compound chondrules.

Compound chondrules, which consist of two or more chondrules fused together, exist in various classes of chondrites. Although the fraction of compound chondrules is very small ($\sim 5\%$ of all chondrules), they offer crucial information regarding the physical and chemical states of solid materials during chondrule formation because of their uniqueness (Gooding

and Keil 1981, Wasson et al. 1995, Sekiya and Nakamura 1996, Akaki and Nakamura 2005, Ciesla et al. 2006). Some compound chondrules seem to have been formed by mutual collisions between two or more independent chondrules during the heating event (Wasson et al. 1995, Akaki and Nakamura 2005).

Some formation models for compound chondrules have been proposed so far. In a simple consideration, mutual collisions among molten dust particles in the solar nebula are thought to be responsible for the formation of compound chondrules (Gooding and Keil 1981, Wasson et al. 1995, Sekiya and Nakamura 1996). However, it has been shown that the rate of collisions among molten particles is too low to explain the observed fraction of compound chondrules when one estimates the number density of the dust particles based on the minimum mass solar nebula model. The number density of molten dust particles should be enhanced by some means. Another group of models are ones based on the shock-wave heating chondrule formation model. However, Nakamoto and Miura (2004) have suggested that if the number density of large dust particles is higher than a critical density, they are destroyed in a shock wave. Thus, it seems that the number density of the precursor particles should be lower than the critical density to produce the compound chondrules in the framework of the shock-wave heating model. A model that may meet simultaneously these conditions, i.e., the low number density of the precursor particles and the high frequency of collisions among molten particles, is the fragment-collision model proposed by Miura et al. (2008a). It may be worth noting that the vapor pressure in the chondrule forming region can be very high, if a lot of small dust particles are contained in the region and evaporated by the shock-wave heating, even though the number density of the large dust particles is low enough. The high vapor pressure would be suitable to explain the chemical and the isotopic fractionation patterns in chondrules (e.g., Cuzzi and Alexander 2006, Alexander et al. 2008).

The other model is the jet flow model (Liffman and Brown 1996). In this model, chondrules are formed when a chondrule precursor particle is hovering in the jet flow. Such a hovering chondrule would be impacted by smaller chondrules that are still entrained in the

jet flow and would form a compound chondrule. Although it is still not clear whether the rate of collisions which satisfies the collision condition is high enough or not, this model may provide a first-order explanation why adhering compound chondrules always have a small plastic chondrule adhering to a solid large chondrule.

In this part, we focus on the "fragment-collision model" in the frame-work of the shock-wave heating model. If there is a cm-sized dust particle, only the surface is heated and melted due to the gas frictional heating because of its large size (Yasuda and Nakamoto 2005, 2006; see also section 8.1). The molten surface is distorted by the strong gas ram pressure, and then a lot of fragments are extracted from the original dust particle. The disruption event has been examined experimentally (Kadono and Arakawa 2005), analytically (Kato et al. 2006), and numerically (Miura and Nakamoto 2007). Since the local number density of fragments behind the original dust particle is enhanced, the mutual collisions among these fragments are likely to occur frequently. In addition, the collisions would occur during the chondrule formation event as inferred from the observations of compound chondrules. We estimated the collision probability, which is the number of collisions experienced by a fragment in one disruption event, is up to ~ 0.5. Therefore, the observed fraction of compound chondrules can be explained if a certain fraction (e.g., 10%; Miura et al. 2008a) of large dust particles experience the disruption event in the chondrule-forming region.

In the simple model proposed by Miura et al. (2008a), we calculated the collision probability by using statistical quantities (velocity dispersion and number density of fragments) in which the radii of all the fragments were uniform. However, the velocity dispersion does not necessarily lead to the mutual collisions among fragments; for example, in the case where fragments are ejected radially from the original dust particle and they have velocities proportional to the distance from the original dust particle, mutual collisions would not occur. In addition, even if the fragments collide each other, they do not coalesce necessarily because the condition whether the colliding two drops coalesce or not depends on the collision velocity (Weber number of impact) and the collision angle (impact parameter) according to

the collision experiments (Ashgriz and Poo 1990, Qian and Law 1997). In order to answer these questions, we need to obtain the physical values of each fragment (velocity, position, radius, and orbit) and parameters of each collision (Weber number of impact and impact parameter), not the statistical quantities.

The purpose of this study is to examine the disruption of a molten dust particle and dynamics of fragments by using three-dimensional hydrodynamics simulations. We trace the motion of each fragment extracted from the original dust particle and obtain the radius, velocity and position at every moment. It should be noted that fragments are accelerated by the gas flow behind the original dust particle. From this simulation, we can analyze the phenomena of collisions among fragments and obtain the relative velocities and collision angles of impacts. Comparing these quantities with results of collision experiments, we can discuss whether these collisions contribute to the formation of compound chondrules or not and then calculate the probability of the compound chondrule formation. We call the disrupted dust particle as "parent particle" and fragments as "ejectors" in this study.

8 Model

8.1 Outline of Our Model

In the post-shock region, the unmelted parent dust particle is exposed to the gas flow and heated by the gas frictional heating. Since the gas frictional heating takes palce only at the surface of the parent particle, there is a temperature gradient from the hotter surface to cooler interior in the heating phase. The temperature difference between the surface and interior is proportional to its size (Appendix E.3.2). For a small particle with radius of 100 μm, the typical temperature difference is only ~ 5 K at most. In contrast, it is up to about a several hundred K for a cm-sized one. Such a large dust particle melts from the surface, then the molten surface gradually spreads toward interior due to the thermal diffusion. It results in the formation of liquid layer at the surface of the parent particle (*partially-molten*

condition). The liquid layer becomes wider as the time goes on and will be disrupted by the gas ram pressure when the width of the liquid layer reaches an enough thickness. The critical thickness of the liquid layer $h_{\rm cr}$ above which the disruption will take place is given by an empirical form as (Kadono and Arakawa 2005, 2008)

$$h_{\rm cr} \sim (10-20)\gamma_{\rm s}/p_{\rm fm}, \tag{53}$$

where $\gamma_{\rm s}$ is the surface tension coefficient and $p_{\rm fm}$ is the gas ram pressure. As a result of the disruption, many ejectors are extracted from the liquid layer and scattered behind the parent particle. We think that the mutual collisions between these ejectors lead to compound chondrule formation.

8.2 Basic Equations

In order to simulate the disruption of a *partially-molten* parent particle exposed to the high-speed gas flow, we solve the equations of continuity, motion, and energy. The basic equations are almost the same as those in the previous part.

8.2.1 Equation of Continuity

In order to express the parent particle and ejectors, that is, the silicate dust particles in the computational box, we use the color function ϕ, which takes the value of unity ($\phi = 1$) inside the parent particle and ejectors, and zero ($\phi = 0$) outside of them. Using the color function and the density of the fluid element ρ is given by

$$\rho = \rho_{\rm d} \times \phi + \rho_{\rm a} \times (1-\phi), \tag{54}$$

where the subscripts "d" and "a" indicate the dust particle and the ambient region, respectively. The equation of continuity is written by using the color function under the condition of $\rho_{\rm a}/(\rho_{\rm d}-\rho_{\rm a}) \ll 1$ as (Miura and Nakamoto 2007)

$$\frac{\partial \phi}{\partial t} + \boldsymbol{\nabla} \cdot (\phi \boldsymbol{u}) = 0, \tag{55}$$

where $\boldsymbol{u}$ represents the velocities of fluid elements in the rest frame of the center of mass. This equation describes the time evolution of the color function, and the density ρ through Eq. (54) as well.

8.2.2 Equation of Motion

The equation of motion is given by

$$\frac{\partial \boldsymbol{u}}{\partial t} + (\boldsymbol{u} \cdot \boldsymbol{\nabla})\boldsymbol{u} = \frac{-\boldsymbol{\nabla} p + \mu \triangle \boldsymbol{u} + \boldsymbol{F}_{\rm s} + \boldsymbol{F}_{\rm g}}{\rho} + \boldsymbol{g}, \tag{56}$$

where p, μ, $\boldsymbol{F}_{\rm s}$, $\boldsymbol{F}_{\rm g}$, and $\boldsymbol{g}$ are the pressure, viscosity, surface tension, gas ram pressure, and apparent gravitational acceleration, respectively. The viscosity is expressed by using the color function as

$$\mu = \mu_{\rm d} \times \phi + \mu_{\rm a} \times (1 - \phi), \tag{57}$$

where $\mu_{\rm d}$ and $\mu_{\rm a}$ are viscosities of the dust particle and the ambient region, respectively. In our model, $\mu_{\rm d}$ is a function of the internal energy of the dust particle and we distinguish the liquid part from the solid part by varying the value of $\mu_{\rm d}$ (see subsection 8.2.4). It should be noted that the forces $\boldsymbol{F}_{\rm s}$ and $\boldsymbol{F}_{\rm g}$ act only at the surface of the drop ($|\boldsymbol{\nabla}\phi| \neq 0$). In addition, we model the gas flow as a free molecular flow because the nebula gas is so rarefied that the mean free path of the gas molecules is longer than the typical dust size (Miura and Nakamoto 2007). The reason why $\boldsymbol{g}$ appears in Eq. (56) is due to our coordinate system co-moving with the mass center of the dust particles, which are accelerated by the gas flow.

8.2.3 Equation of State

We can obtain the equation that describes the time evolution of the pressure p from the equation of state, which is given by

$$\frac{dp}{d\rho} = c_{\rm s}^2, \tag{58}$$

where $c_{\rm s}$ is the sound speed.

8.2.4 Equation of Energy

Liquid and solid states in dust particles are distinguished by different viscosities. We model the viscosity of the dust particle as a function of the internal energy. We set $\mu_{\rm d} = \mu_{\rm liq}$ at $e = e_{\rm liq}$ and $\mu_{\rm d} = \mu_{\rm sol}$ at $e = e_{\rm sol}$, where $e_{\rm sol}$ and $e_{\rm liq}$ are internal energies at the liquidus and solidus, respectively. We assume that the viscosity is given by

$$\mu_{\rm d} = \begin{cases} \mu_{\rm sol} & \text{for } e \le e_{\rm sol}, \\ \mu_{\rm sol} \exp\left[\frac{\ln(\mu_{\rm liq}/\mu_{\rm sol})}{e_{\rm liq}-e_{\rm sol}}(e-e_{\rm sol})\right] & \text{for } e_{\rm sol} < e < e_{\rm liq}, \\ \mu_{\rm liq} & \text{for } e_{\rm liq} \le e. \end{cases} \tag{59}$$

Since the internal energy is transported by the fluid motion, we need to solve the advection of the internal energy. The energy conservation equation is written by

$$\frac{\partial e}{\partial t} + \boldsymbol{\nabla} \cdot (e\boldsymbol{u}) = 0. \tag{60}$$

Strictly speaking, there are other terms that change the internal energy; the gas frictional heating, the radiative cooling of the dust, the heating due to the ambient radiation field, viscous dissipation, and thermal diffusion. However, we can ignore these terms in our calculation (Appendix C).

8.3 Identification of Ejectors

In order to trace the motion of each ejector and the mutual collisions among ejectors, we have to identify each ejector as an isolated object in our hydrodynamics simulation. We apply "Clump Find" method for the detection of these isolated objects. This method is used in some fields, e.g., the information technology, astrophysics, and so forth (e.g., Williams et al. 1993). By using this method, we can obtain the information of the time evolution of the number of isolated ejectors extracted from the parent particle, and the information of each ejector (position, radius, and velocity). We explain the method of identification of ejectors in our simulation in this subsection.

We consider that there exists the dust particle on the grid point (i, j, k) if the color function at the point $\phi_{i,j,k}$ exceeds the critical value $\phi_{\rm cr}$. We call the dust-existing grid point

as "*portion*" hereinafter. At initial state of calculation, all *portions* locate only inside the parent particle. So there initially exists only one isolated object in the computational box. We number this isolated object as $m = 0$ (Figure 29A). The liquid part is torn off from the parent particle due to the gas flow. If all *portions* adjoin others, there is still one isolated object (Figure 29B). However, if the connection of the *portions* breaks off, one more isolated object appears in the computational box (Figure 29C). As the time goes on, many isolated objects will be generated (Figure 29D). After applying the "Clump Find" method, we can detect all isolated objects, $m = 1, 2, 3, ...$, in detected order. We calculate the physical values of each isolated object as follows; the radius $r_{\rm e}$ is calculated by assuming a perfectly spherical shape, the position $\boldsymbol{x}_{\rm e} = (x_{\rm e}, y_{\rm e}, z_{\rm e})$ is given by that of the mass center, and the velocity $\boldsymbol{v}_{\rm e} = (v_{{\rm e},x}, v_{{\rm e},y}, v_{{\rm e},z})$ is given by that of the mass center, respectively. Namely,

$$r_{\rm e} = \left(\frac{3}{4\pi} \sum_{(i,j,k)\in m} \phi_{i,j,k} dxdydz \right)^{\frac{1}{3}}, \tag{61}$$

$$\boldsymbol{x}_{\rm e} = \frac{\sum_{(i,j,k)\in m} \phi_{i,j,k} \boldsymbol{x}_{i,j,k} \rho_{\rm d} dxdydz}{\sum_{(i,j,k)\in m} \phi_{i,j,k} \rho_{\rm d} dxdydz}, \tag{62}$$

$$\boldsymbol{v}_{\rm e} = \frac{\sum_{(i,j,k)\in m} \phi_{i,j,k} \boldsymbol{v}_{i,j,k} \rho_{\rm d} dxdydz}{\sum_{(i,j,k)\in m} \phi_{i,j,k} \rho_{\rm d} dxdydz}. \tag{63}$$

In our simulation, there is a very tiny fragment with which the total sum of the color function of portions is less than unity. We does not account such tiny fragments because of the computational resolution.

8.4 Initial Settings and Input Parameter

We investigate the case with the parent radius $r_{\rm p} = 5$ mm and the ram pressure of the gas flow $p_{\rm fm} = 2 \times 10^4$ dyn cm^{-2}, which is realized in the shock-wave heating model for relatively high-density and low-velocity shock waves (Iida et al. 2001, Miura et al. 2008a). In this case, the width of the liquid part $h_{\rm cr}$ calculated by Eq. (53) is $2 - 4$ mm with the surface tension coefficient of $\gamma_{\rm s} = 400$ dyn cm^{-1} for molten silicates (Murase and McBirney, 1973). The viscosity in the liquid part is $\mu_{\rm liq} = 1.0$ poise from the model of Uesugi et al. (2003), in which they calculated the viscosity by using the formulation of Bottinga and Weill (1972)

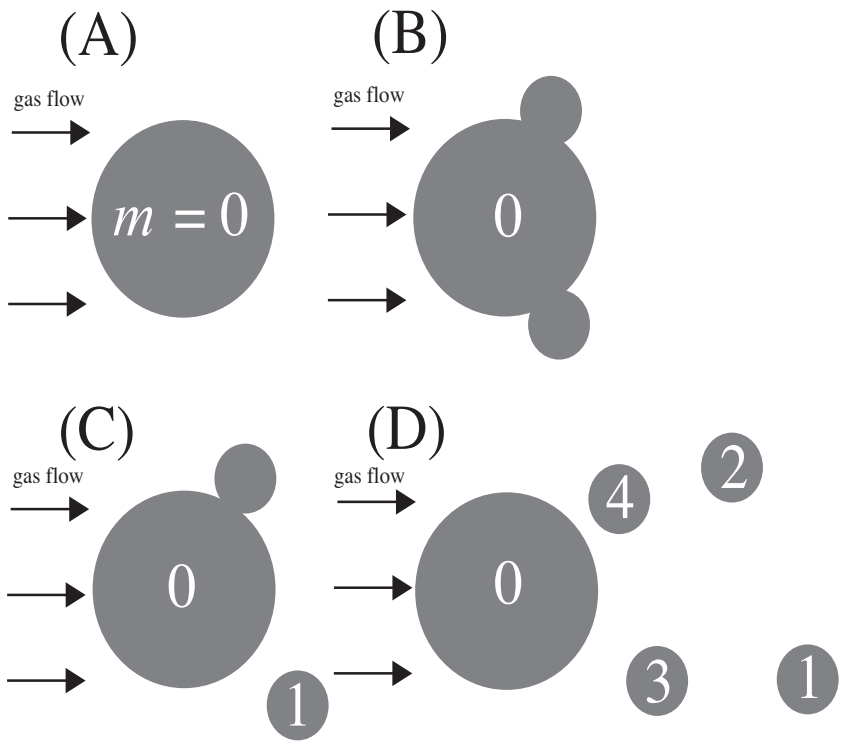

Figure 29: A schematic picture of the method for identifying each ejector. Grey objects represent *portions*, which are the grid points whose color function exceeds the critical value ($\phi_{\rm cr} = 0.1$). We number the isolated objects using m. Detailed procedure is described in section 8.3.

assuming the dust temperature ∼1800 K and the chemical composition of a typical BO type chondrule. In the solid part, we adopt $\mu_{\rm sol} = 10^6$ poise, which is high enough for the fluid element not to be deformed in the timescale of breakup of the liquid part. Other parameters are listed in Table 1.

Figure 30(A) shows the initial condition of our simulation. The horizontal, vertical, and depth axes are the z- (the direction of the gas flow), y- and x-axes normalized by the initial parent radius $r_{\rm p}$, respectively. We set the critical value of the color function as $\phi_{\rm cr} = 0.1$ and the orange object represents the external shape of the parent particle (iso-surface of $\phi = \phi_{\rm cr}$). There are two parts inside the parent particle; the liquid part at a side facing to the gas flow and the solid part at the opposite side. For simplicity, we assume that these two parts are divided by a sharp boundary at the center of the parent as shown by a dotted line. In this case, the width of the liquid layer is $h_{\rm cr} = r_{\rm p} = 5$ mm. It is consistent with the setting of our simulation ($h_{\rm cr} = 2 - 4$ mm from the empirical expression of the disruption, Eq. 53).

Parameter	Notation	Value
Ram pressure of gas flow	p_{fm}	$20,000$ dyn cm^{-2}
Surface tension	γ_{s}	400 dyn cm^{-1}
Viscosity of liquid	μ_{liq}	1.0 poise
Viscosity of solid	μ_{sol}	10^{6} poise
Viscosity of ambient region	μ_{a}	10^{-2} poise
Density of dust particle	ρ_{d}	3 g cm^{-3}
Density of ambient region	ρ_{a}	10^{-6} g cm^{-3}

Table 1: Input physical parameters for our numerical simulation.

9 Numerical Calculation Results

9.1 Disruption of Dust Particle

Figure 30 shows the evolution of the half-molten parent particle exposed to the gas flow. Each panel corresponds to the snapshot at (B) $t = 0.0050$ sec, (C) 0.0060 sec, (D) 0.0085 sec, (E) 0.0113 sec, and (F) 0.0136 sec, respectively. First, the liquid part is blown toward the down stream due to the gas flow, because the ram pressure of the gas flow overcomes the surface tension of the dust particle (B). The liquid part is deformed significantly with time and some arm-like structures appear behind the parent particle. At this time, no isolated clump except the parent particle is identified (C). As the liquid part increases its surface area, the arm-like structures are divided into a lot of small fragments and some isolated ejectors are identified (D). After that, many ejectors appear behind the parent particle (E). Finally, we detect some mutual collisions among ejectors, e.g., two ejectors labeled by "no. 3" and "no. 6" collide with each other (F) (details of the collision are discussed in section 10.2). In this way, the molten parent particle is disrupted by the strong gas ram pressure and a lot of small ejectors appear behind it.

9.2 Motion of Accelerated System

In order to examine the disruption of the parent particle and the motions of ejectors, we introduce the inertial frame (x', y', z') in which the parent particle is at rest at the initial state $t = 0$. The coordinate system (x, y, z) we adopted for the simulation is co-moving with the mass center of the dust particle, so these two coordinate systems are parting each other with time. We set that the origin of the inertial system, O$'$, corresponds to that of the co-moving system, O at $t = 0$. The position of O on the

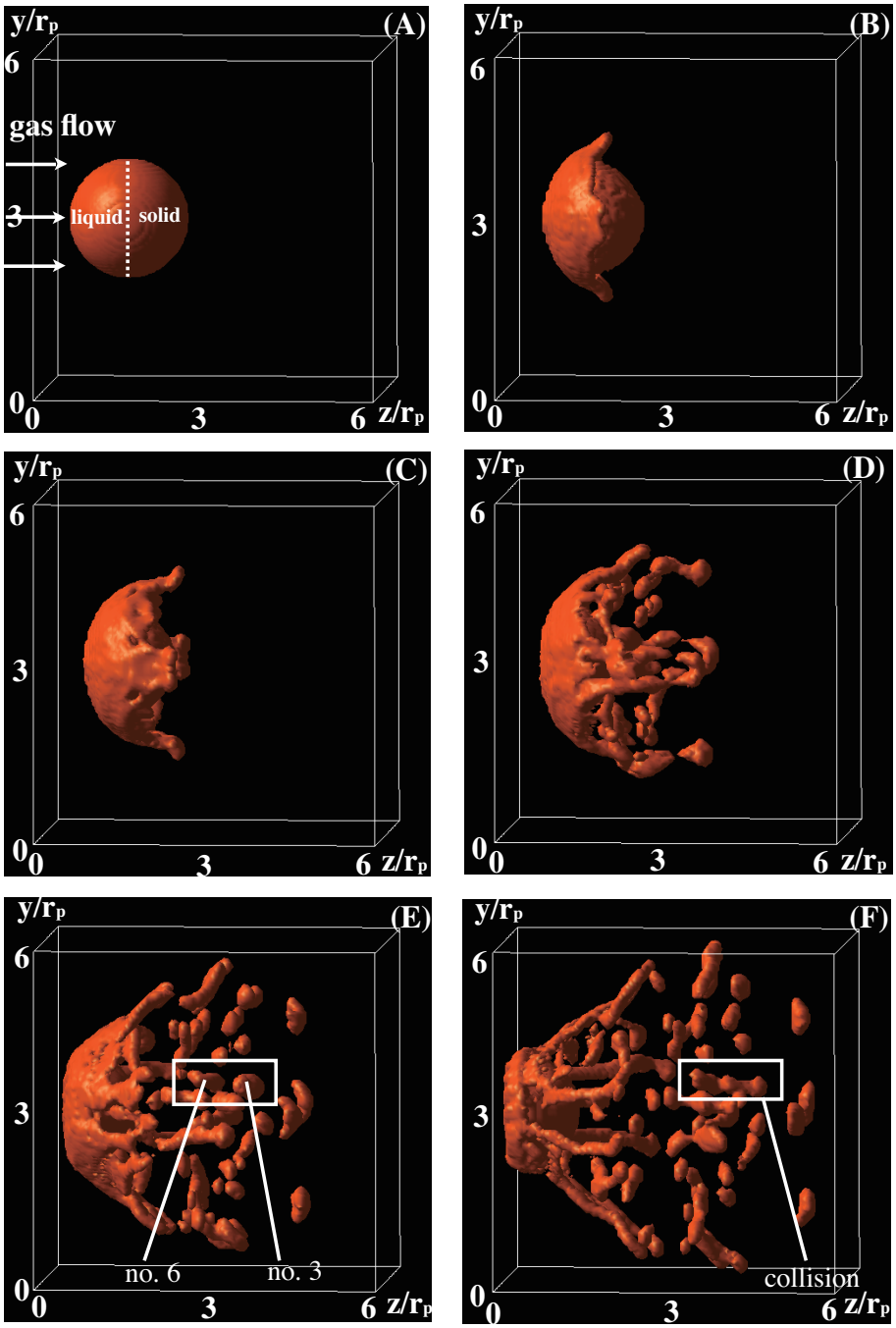

Figure 30: Hydrodynamics evolution of the half-molten parent particle. The ram pressure of the gas flow is 2×10^4 dyn cm^{-2}. Initial radius of the particle is 5 mm. The orange object represents the dust particle. Panel (A) shows the initial condition, and panels (B)-(F) show snapshots at $t = 0.0050$ sec, 0.0060 sec, 0.0085 sec, 0.0113 sec, and 0.0136 sec, respectively.

inertial system, $\boldsymbol{X} = (X, Y, Z)$ is given by

$$\boldsymbol{X}(t) = \int_0^t \boldsymbol{V}(t')dt', \tag{64}$$

where $\boldsymbol{V}$(t) is the velocity of the co-moving system relative to the inertial system. The velocity $\boldsymbol{V}$ is given by

$$\boldsymbol{V}(t) = -\int_0^t \boldsymbol{g}(t')dt', \tag{65}$$

where $\boldsymbol{g}$(t) is the apparent gravitational acceleration shown in Eq. (56).

Fig. 31 shows the time variation of the position of the origin O on the z'-axis. The solid curve represents the result of our simulation and the dashed curve shows the accelerated motion with a constant acceleration of

$$a_{\rm p} = \frac{3p_{\rm fm}}{4\rho_{\rm d} r_{\rm p}}, \tag{66}$$

which is the one for a parent particle exposed to the gas flow without deformation. Simulation results agree with the constantly-accelerated motion for $t < 0.006$ sec. However, at around $t = 0.006$ sec, the motion of the simulation deviates from the constantly-accelerated one. This is because the surface area of the parent particle increases due to the deformation (see Figs. 30B, C, and D). It should be noted that $x' \approx x$ and $y' \approx y$ because the center of mass does not move significantly to x' and y'-directions, that is, $X \approx 0$ and $Y \approx 0$.

9.3 Ejection Velocities and Ejectors

We identified totally 32 isolated ejectors at $t = 0.0134$ sec in the computational box. Table 2 summarizes sizes, positions, and velocities of ejectors at moments of their ejections. The mean velocities of all the ejectors are $\bar{v}'_x = 6.16$ cm s^{-1} for x'-direction,

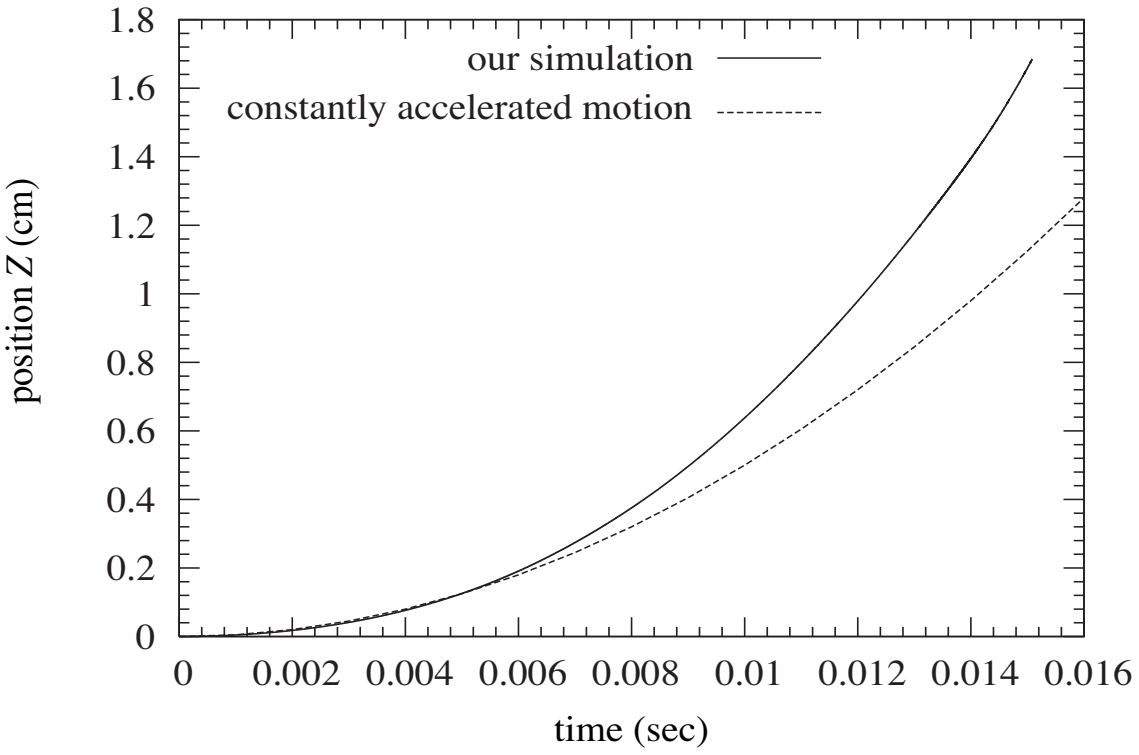

Figure 31: The time variation of the position of the origin of co-moving system O on the z'-axis. The solid curve represents our simulation result. The dashed curve shows a constantly-accelerated motion assuming that the parent particle is not deformed. Our simulation result deviates from the constantly-accelerated motion at around $t = 0.006$ sec due to the deformation of the parent particle.

$\bar{v}'_y = 6.87$ cm s^{-1} for y'-direction, and $\bar{v}'_z = 318.1$ cm s^{-1} for z'-direction, respectively. On the other hand, the velocity dispersions for each direction are $\Delta v'_x = 37.6$ cm s^{-1}, $\Delta v'_y = 27.7$ cm s^{-1}, and $\Delta v'_z = 55.6$ cm s^{-1}, respectively. For x'- and y'-directions, which are perpendicular to the gas flow, the mean velocities are much smaller than the velocity dispersions. It suggests that the distribution of ejectors on the projection to the $x'y'$-plane is almost symmetrical. Figure 32 shows positions, velocities, and radii of all the ejectors at moments of their ejections projected on the $x'y'$-plane. The filled circle at the center indicates the parent particle at the initial setting, open circles are the ejectors, and arrows are the ejection velocities. It is found that the distribution of the ejectors is almost axi-symmetric on the $x'y'$-plane.

We also calculate the velocity components for r'- and θ'-directions, where r' is the radial coordinate with the origin at the center of the parent particle and θ' is the azimuth on the $x'y'$-plane. The mean velocities for r'- and θ'-directions are $\bar{v}'_r = 38.3$ cm s^{-1} and $\bar{v}'_\theta = 0.94$ cm s^{-1}, respecitively. On the other hand, velocity dispersions for these directions are $\Delta v'_r = 14.8$ cm s^{-1} and $\Delta v'_\theta = 5.98$cm s^{-1}, respectively. Since the mean velocity for r'-direction is larger than the velocity dispersion, most of the ejectors are parting from the parent dust particle on the $x'y'$-plane. For the azimuthal component, both the mean velocity and the velocity dispersion are much smaller than $\bar{v}'_r$. These results are consistent with results that all the ejectors are ejected from the parent particle radially as shown in Fig. 32.

On the contrary, the mean velocity for z'-direction (corresponds to the gas flow direction) is much larger than the velocity dispersion. It indicates that these ejectors are accelerated by the gas flow relative to the parent particle.

number m	ejected time (sec)	$r_{\rm e}$ (mm)	$x'_{\rm e}/r_{\rm p}$	$y'_{\rm e}/r_{\rm p}$	$z'_{\rm e}/r_{\rm p}$	$v'_{{\rm e},x}$(cm s^{-1})	$v'_{{\rm e},y}$(cm s^{-1})	$v'_{{\rm e},z}$(cm s^{-1})
1	0.85×10^{-2}	0.96	2.00	2.00	3.02	-12.5	-11.3	230.1
2	0.88×10^{-2}	0.98	4.00	1.96	3.20	12.5	-11.3	235.6
3	0.90×10^{-2}	0.98	4.00	4.06	3.26	19.5	17.9	236.5
4	0.93×10^{-2}	0.99	1.98	4.06	3.48	-20.8	13.7	246.6
5	0.98×10^{-2}	1.15	2.02	2.04	2.88	-8.27	-5.96	226.9
6	1.00×10^{-2}	1.11	3.98	4.00	2.96	21.1	23.9	234.1
7	1.01×10^{-2}	1.10	2.04	4.00	3.02	-13.1	20.8	242.9
8	1.01×10^{-2}	1.00	2.64	5.14	5.18	-5.93	49.1	283.4
9	1.02×10^{-2}	1.04	2.68	1.08	4.36	19.0	-19.3	310.1
10	1.03×10^{-2}	0.94	1.22	2.64	4.44	-40.3	-1.22	313.9
11	1.03×10^{-2}	1.10	3.98	2.02	3.10	18.6	-6.78	249.9
12	1.06×10^{-2}	0.83	4.94	2.76	5.48	26.3	-4.69	388.0
13	1.06×10^{-2}	0.86	4.98	3.26	5.46	30.0	8.59	388.7
14	1.07×10^{-2}	0.94	4.86	3.32	4.46	51.3	9.86	313.8
15	1.11×10^{-2}	0.97	3.36	1.08	4.92	11.0	-44.5	323.9
16	1.11×10^{-2}	1.06	1.00	2.98	5.92	-22.2	5.68	300.4
17	1.11×10^{-2}	0.93	1.10	3.32	4.92	-45.2	5.74	325.1
18	1.11×10^{-2}	0.86	3.32	4.96	4.90	6.92	44.2	325.4
19	1.12×10^{-2}	0.95	2.67	0.78	5.70	-0.38	-44.3	305.4
20	1.17×10^{-2}	1.00	5.02	2.64	5.16	56.9	2.64	329.4
21	1.17×10^{-2}	0.98	4.62	2.64	4.10	66.7	-7.56	331.3
22	1.17×10^{-2}	1.00	4.76	3.26	4.20	54.5	9.80	340.5
23	1.20×10^{-2}	0.92	2.68	4.94	4.62	1.62	52.9	371.2
24	1.22×10^{-2}	1.04	1.22	2.70	4.60	-45.3	-1.02	356.2
25	1.22×10^{-2}	1.09	1.22	3.26	4.54	-49.3	13.8	348.5
26	1.26×10^{-2}	0.94	2.70	4.42	4.20	2.91	36.8	325.9
27	1.26×10^{-2}	0.82	2.74	5.08	7.16	-6.50	33.3	403.8
28	1.26×10^{-2}	1.08	2.66	1.24	4.80	-3.34	-42.7	361.1
29	1.26×10^{-2}	1.19	3.36	1.24	4.82	13.0	-42.3	368.5
30	1.32×10^{-2}	0.90	4.58	3.34	4.66	48.4	6.06	359.2
31	1.34×10^{-2}	0.83	3.30	4.50	4.80	3.11	42.3	375.0
32	1.34×10^{-2}	0.97	3.28	5.12	5.90	6.74	65.7	429.0

Table 2: Identified ejectors. The radius, the position, and the velocity of each ejector at ejected time are listed.

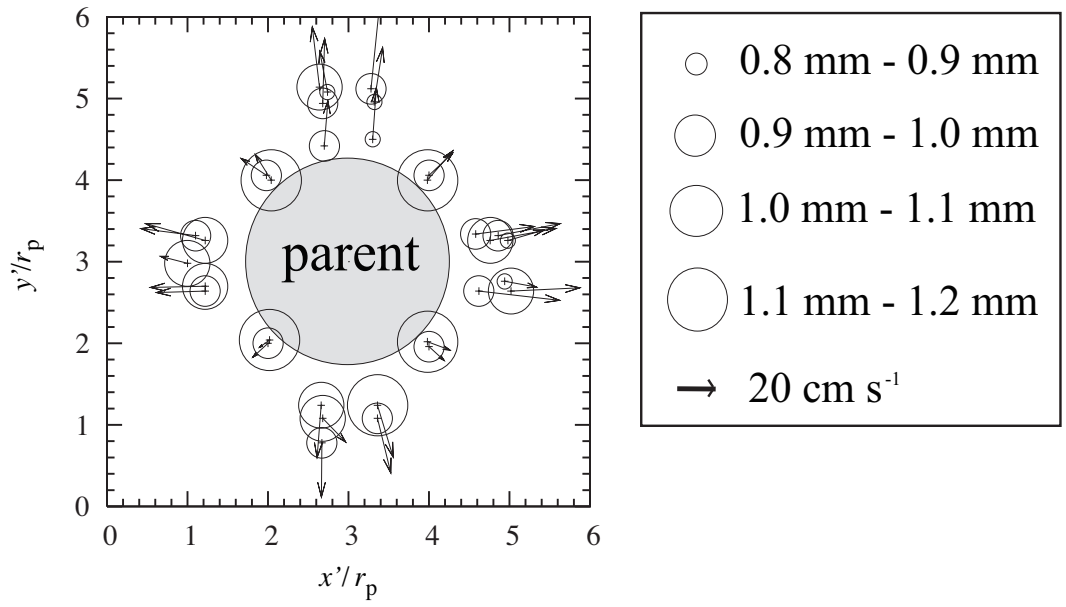

Figure 32: Positions, velocities, and radii of ejectors at their ejection time projected on the x'-y' plane. The data are from Table 2. The grey circle labeled "parent" indicates the position and the radius of the parent particle at the initial state. The radii of circles depend on the actual particle radii as shown in the legend.

9.4 Size Distribution of Ejectors

Figure 33 shows the size distribution of 32 ejectors listed in Table 2. The horizontal axis shows the ejector diameter, d_e, and the vertical axis shows the cumulative number of ejectors with diameters larger than the horizontal value, N, in a logarithmic scale. The mean diameter of ejectors is 1.90 mm and the median one is 1.96 mm. It is found that the size distribution seems along a straight line on the semi-log plot in a range of 1.6 mm $< d_e <$ 2.4 mm. It means that the size distritbution of ejectors can be fitted well by an equation $\ln(N) = a - d_e/b$, where a is a constant and b is the characteristic size of the size distribution. The best fit parameters are found to be $a = 7.923 \pm 0.353$ and $b = 0.378 \pm 0.028$ mm, respectively. The best fit line is displayed in Fig. 33 by a solid line. The size distribution of ejectors has an exponential form as $N \propto e^{-d_e/b}$.

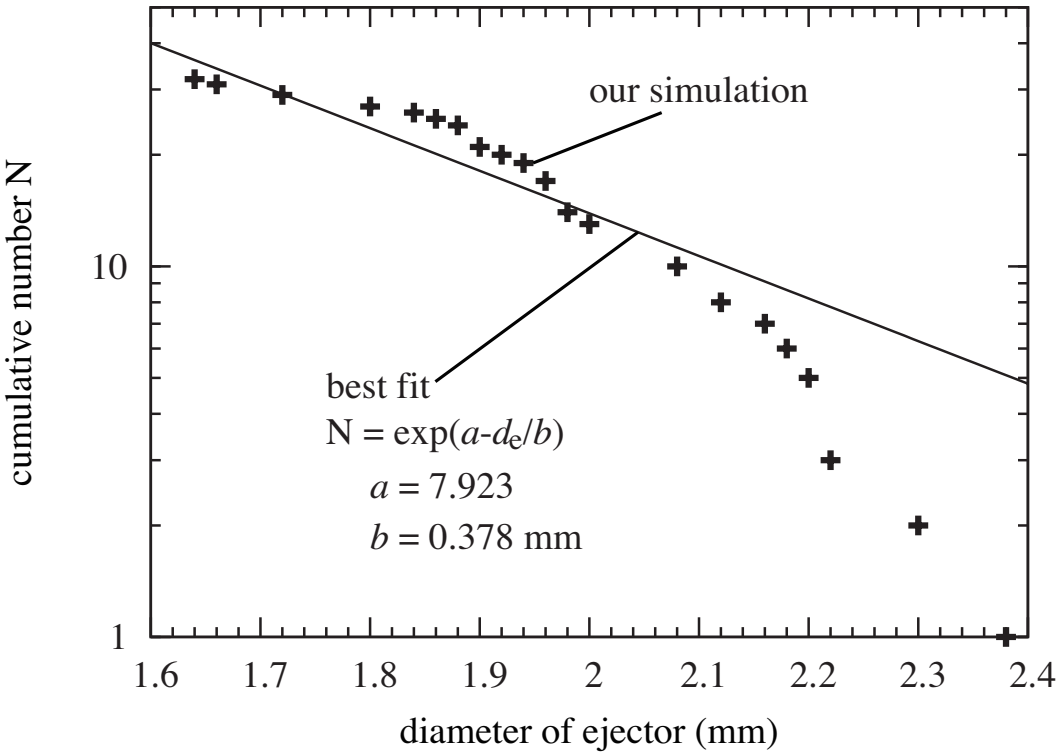

Figure 33: A size distribution of ejectors. The horizontal axis is the ejector diameter and the vertical axis is the cumulative number of ejectors whose diameters are larger than the horizontal value. The symbol "plus" (+) represents our simulation result and the solid line is the best fit line of our simulation. The data are from Table 2.

9.5 Collisions Among Ejectors

As the disruption proceeds, the number of ejections counted in the computational box increases. Figure 34 shows the time variation of the total number of ejections $N_{\rm ejection}$ by the solid line. The total number of ejections, $N_{\rm ejection}$, increases monotonically with t up to $N_{\rm ejection} = 32$ by the end of the run. If no ejector collides with others, $N_{\rm ejection}$ should be equal to the number of ejectors existing in the computational box at a certain time, $N_{\rm exist}$. However, the dashed line shows that the number of ejectors $N_{\rm exist}$ decreases with time after $t = 0.0135$ sec. This is because the collisional coalescence occurs among ejectors. We also display the number of collisions among ejectors, $N_{\rm coll}$, by the dotted line. Since a collision unifies two ejectors into a larger one, the number $N_{\rm exist}$ decreases one per collision. So, we obtain $N_{\rm coll} = N_{\rm ejection} - N_{\rm exist}$. The number of collisions $N_{\rm coll}$ increases up to $N_{\rm coll} = 12$ by the end of the run. The final number of ejectors is $N_{\rm exist} = 20$. The ratio of the number of collisions to the final number of ejectors, $R_{\rm com} = N_{\rm coll}/N_{\rm exist}$, which indicates the ratio of compound bodies produced in this event, is 0.60 in this case. In addition, the rate of ejectors which experienced collisions, $R_{\rm coll}$, can be calculated by $R_{\rm coll} = 2N_{\rm coll}/N_{\rm ejection} = 24/32 = 0.75$ because in our simulation, there is no ejector which experienced multiple collisions, and the expectation value of the number of collision for an ejector is $E_{\rm coll} = 24/32 = 0.75$, respectively. It should be noted, that these values are the smallest estimation, because we have to finish the simulation before one of the ejectors reaches the boundary of the computational box. If it is possible to trace the motions of ejectors further, these values would be larger.

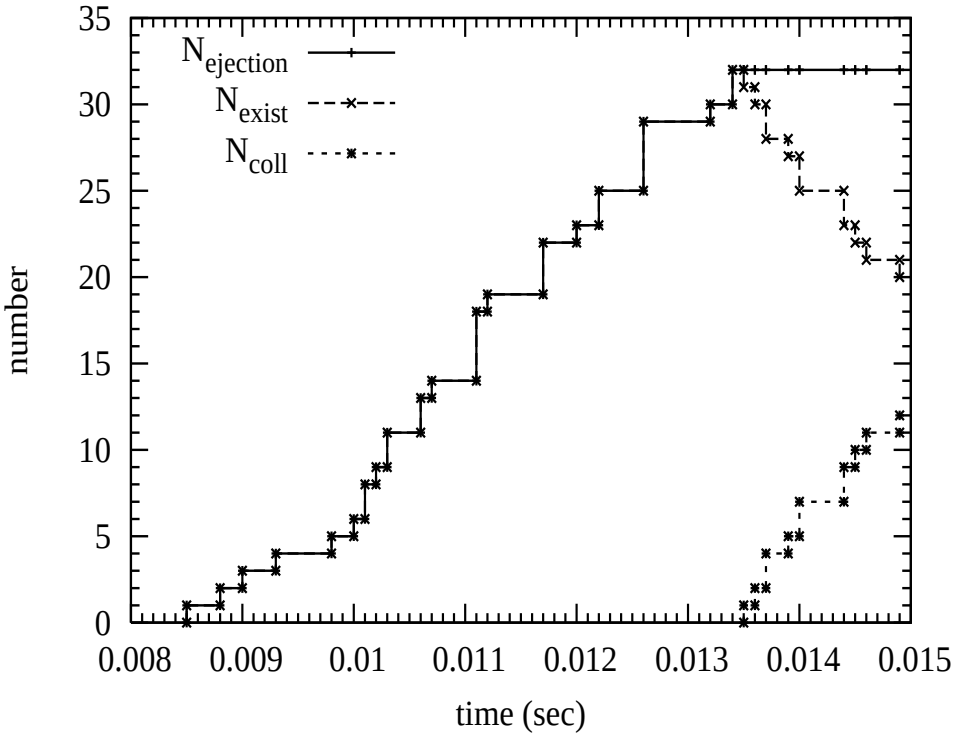

Figure 34: Time variation of the number of ejectors. The solid line represents the total number of ejections ($N_{\rm ejection}$). The dashed line represents the number of ejectors existing in the computational box at a given time ($N_{\rm exist}$). The dotted line represents the total number of collisions at a given time ($N_{\rm coll}$).

10 Discussions

10.1 Size Distribution of Ejectors

In our simulation, we found that the size distribution of ejectors has an exponential form as $N \propto e^{-d_e/b}$ (see section 9.4). The exponential distribution was also observed in a disruption experiment. Kadono and Arakawa (2005) carried out aerodynamic experiments in which a liquid layer was attached to a solid core and then the sample was exposed to a gas flow. They found that the liquid layer was stripped off and the size distributions of ejectors had exponential forms. They also found an empirical formula for the representative size b as

$$\frac{b}{h} = \frac{10.7 \pm 2.2}{We}, \tag{67}$$

where We is the Weber number for the gas flow defined by $We = p_{\rm fm}h/\gamma_{\rm s}$. Figure 35 shows the representative size b as a function of the Weber number We. The vertical axis is the representative size b normalized by the width of liquid layer h. The symbols plus and cross represent the experimental results with G63 (water and glycerol mixture, glycerol 63 % by volume) and water (Kadono and Arakawa 2005), respectively. The dashed line represents the fitted line of the experiments $\frac{b}{h} = 10.7/We$. The symbol of filled square represents the result of our numerical simulation ($We = 25, b/h = 0.756 \pm 0.056$). Our simulation result seems to be in the scatter of the experimental results. We need more studies with a variety of parameters to determine how the size distribution of ejectors is affected by physical environments (for example, Weber number, radius and viscosity of the parent drop). These studies would be helpful to understand the origin of the chondrule size distribution.

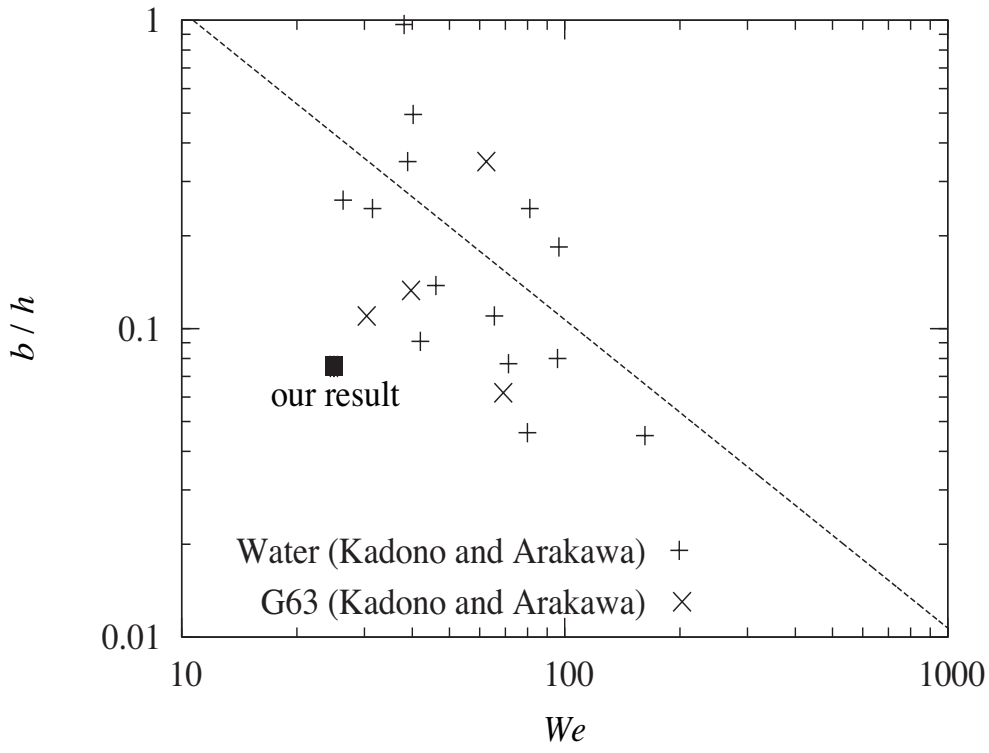

Figure 35: The representative size b normalized by h as a function of the Weber number for the gas flow We. The symbols "plus" (+) and "cross" ($\times$) indicate, respectively, the experimental data of liquid water and G63 (water and glycerol mixture, glycerol 63% by volume) obtained by Kadono and Arakawa (2005). The dashed line indicates the result of fitted data. The symbol "filled square" indicates our numerical result.

10.2 Shadow Effect

As shown in panels (E) and (F) of Fig. 30, two ejectors no. 3 and no. 6 collide each other behind the parent particle. These two ejectors, however, can not collide with each other if the ambient gas flow accelerates both of them in the same way. The acceleration of the ejector by the ambient gas flow is given by (Miura et al. 2008a)

$$a = \frac{3p_{\rm fm}}{4\rho_{\rm d} r_{\rm e}}, \tag{68}$$

which is inversely proportional to the ejector radius $r_{\rm e}$. Since the radius of the no. 3 is about 10% smaller than that of the no. 6, the no. 3 is accelerated more strongly. Fig. 36 shows the paths of these two ejectors where their initial positions and velocities (see Table 2) are taken into account properly. The horizontal axis is the position on the z'-axis and the vertical axis is the time after starting the calculation. Dashed curves are the orbits of each ejector analytically derived assuming an acceleration a given by Eq. (68). The paths of these two ejectors show that they never collide each other because of the difference in the acceleration.

In spite of above consideration, the collision between these two ejectors occurs in the simulation. Solid curves show the paths obtained by the simulation. The gray regions represent calculated tracks of these two ejectors with their radii. The path of no. 6 is very close to the dashed curve which is obtained with the acceleration from the ambient gas flow. In contrast, the acceleration of the no. 3 seems to be much smaller than that expected from Eq. (68). This is because the ambient gas flow toward no. 3 is blocked off by the no. 6 and the ejector no. 3 is not accelerated by the gas flow. We call this effect the *shadow effect*. The schematic picture of the *shadow effect* is shown in Figure 37. Because of the *shadow effect*, the distance between two ejectors becomes shorter with time and finally no. 6 contacts with no. 3

at $t = 0.0135$ sec (pointed by a star). In this case, the velocity difference Δv between these two ejectors, just before the collision, is 110.0 cm s^{-1}. The *shadow effect* plays a very important role as the cause of collisions.

10.3 Collision Conditions

We found that twelve collisions occurred in the computational box by the end of the run (see Fig. 34). However, collisions do not necessarily lead to compound chondrule formation. In order to form a compound chondrule, the collision must satisfy the collision conditions (condition for coalescence and condition for keeping shape). In this subsection, we examine whether or not the collisions detected in our simulation are appropriate for compound chondrule formation comparing with the results of part I. We need to know the collision parameters; the Weber number of collision, the impact parameter, the radii, and the viscosities of the ejectors. We have already obtained the radii, the velocities, and the positions of the ejectors. From these quantities, we can calculate the impact parameter and the Weber number. The impact parameter Im is given by

$$Im = \frac{D}{r_{\rm e1} + r_{\rm e2}}, \tag{69}$$

where D is the distance between the paths of the two colliding ejectors just before the collision, and $r_{\rm e1}$ and $r_{\rm e2}$ are their radii (we assume $r_{\rm e1} < r_{\rm e2}$). The Weber number of impact is the ratio of the momentum flux of impact to the surface tension is defined by

$$We(\text{impact}) = \frac{2\rho_{\rm d}(\Delta v)^2 r_{\rm e1}}{\gamma_{\rm s}}, \tag{70}$$

where Δv is the relative velocity between the two ejectors. We examined the impact parameters and the Weber numbers of impact for all the collisions detected in our

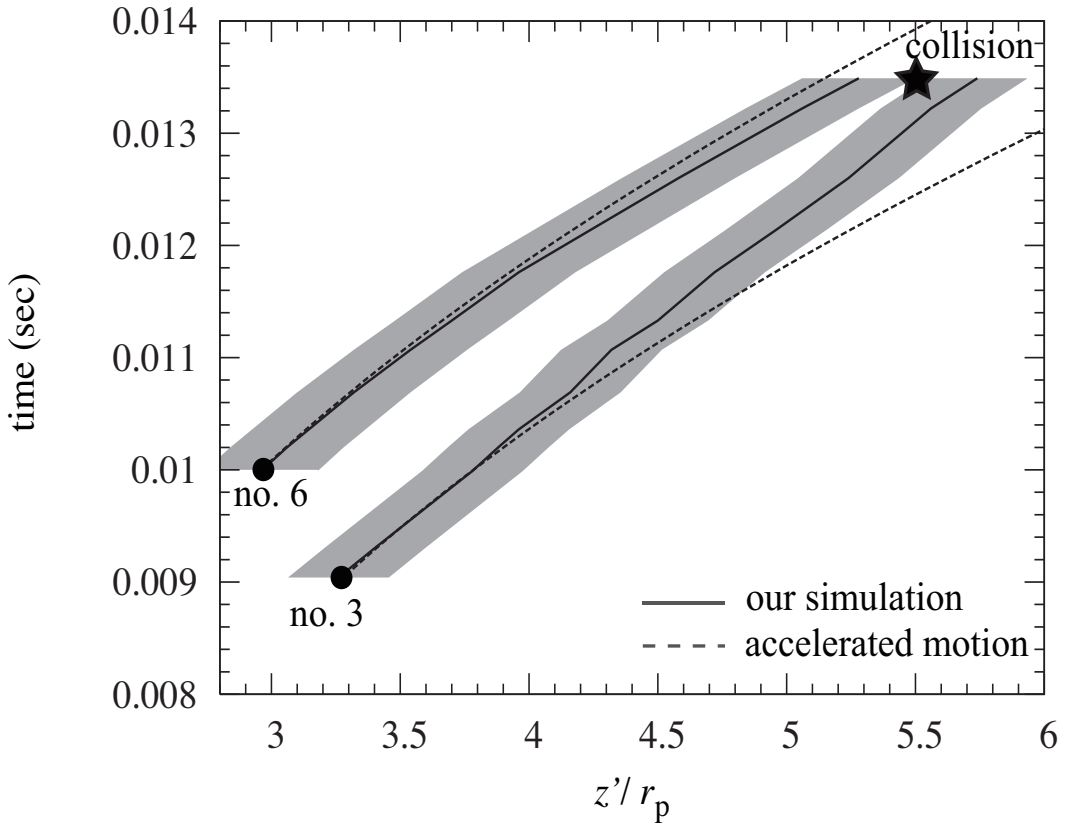

Figure 36: The time variation of the paths of two ejectors, no. 3 and no. 6, shown in Fig. 3(E). The horizontal axis and vertical axis represent the z'-position normalized by the radius of the parent particle and the time, respectively. The solid curves show the orbits obtained by our simulation and the dashed curves show accelerated motions with constant accelerations expected from Eq. (68). The filled circles represent the positions and times at their ejections. The shadowed regions are the ejectors' paths considering their radii. Ejector no. 3 deviates from the accelerated motion due to the shadow effect at around $t \sim 0.01$ sec. As a result, they collide at $t = 0.0135$ sec.

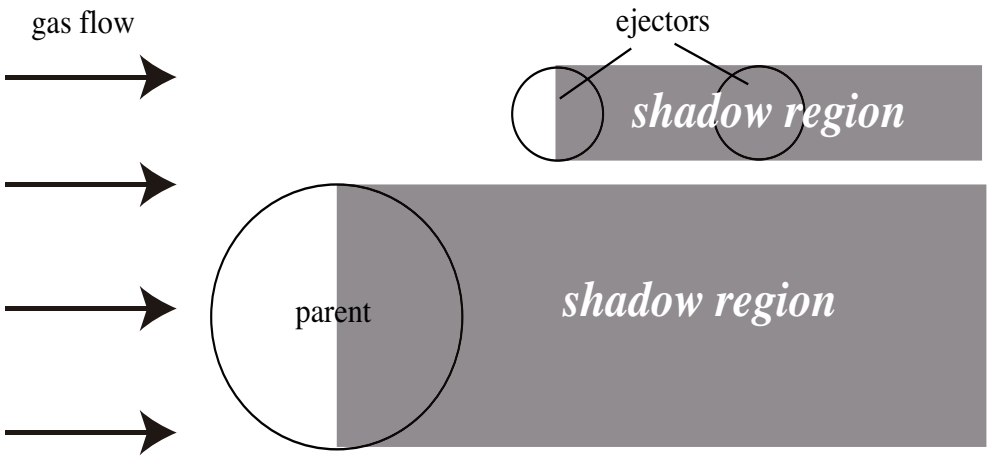

Figure 37: A schematic picture of the *shadow effect*.

simulation and summarized in Table 3.

collision time (sec)	colliding ejectors	r_{e1}	r_{e2}	Δv	Im	We(impact)
1.35×10^{-2}	no. 3 and no. 6	0.98 mm	1.11 mm	110.0 cm s^{-1}	0.24	17.8
1.36×10^{-2}	no. 4 and no. 7	0.99 mm	1.10 mm	80.7 cm s^{-1}	0.33	9.67
1.37×10^{-2}	no. 21 and no. 20	0.98 mm	1.00 mm	69.6 cm s^{-1}	0.51	7.12
1.37×10^{-2}	no. 32 and no. 8	0.97 mm	1.00 mm	96.3 cm s^{-1}	0.96	13.5
1.39×10^{-2}	no. 1 and no. 5	0.96 mm	1.15 mm	104.1 cm s^{-1}	0.33	15.6
1.40×10^{-2}	no. 2 and no. 11	0.98 mm	1.10 mm	105.3 cm s^{-1}	0.29	16.3
1.40×10^{-2}	no. 15 and no. 29	0.97 mm	1.19 mm	131.2 cm s^{-1}	0.28	25.3
1.44×10^{-2}	no. 14 and no. 22	0.94 mm	1.00 mm	126.0 cm s^{-1}	0.31	22.4
1.44×10^{-2}	no. 10 and no. 24	0.94 mm	1.04 mm	75.1 cm s^{-1}	0.10	7.95
1.45×10^{-2}	no. 27 and no. 18	0.82 mm	0.86 mm	121.3 cm s^{-1}	0.24	18.1
1.46×10^{-2}	no. 19 and no. 28	0.95 mm	1.08 mm	134.3 cm s^{-1}	0.34	25.7
1.49×10^{-2}	no. 17 and no. 25	0.93 mm	1.09 mm	41.7 cm s^{-1}	0.40	2.42

Table 3: Normalized impact parameters Im and Weber numbers of impact We(impact) for 12 collisions in our simulation. This table also contains the collision time and ID number of colliding two ejectors (each number of ejector corresponds to the ID number in Table 2), the radii of ejectors, and the relative velocities of them. We define the smaller one as the ejector1.

We cannot obtain the viscosities (temperatures) of the ejectors because we did not calculate the temperature of the ejectors. However, the temperatures of two drops does not change significantly. An ejector ejected earlier is cooled by the radiative cooling due to the shadow effect. Temperature variance of this ejector is

$$\begin{aligned} \Delta T &= \frac{3\varepsilon\sigma T^4}{r_{\rm e}\rho_{\rm d}C}\, t \\ &= 1.56 \left(\frac{\varepsilon}{1}\right) \left(\frac{t}{0.003 \text{ sec}}\right) \left(\frac{T}{1900 \text{ K}}\right)^4 \left(\frac{r_{\rm e}}{1 \text{ mm}}\right)^{-1} \text{K}, \end{aligned} \tag{71}$$

where σ, ε, T, and C are the Stefan-Boltzmann constant, the emissivity of ejector, temperature, and the heat capacity of the dust particle, respectively. We set $C = 1.4 \times 10^7$ erg g^{-1} K^{-1}. This temperature variance does not change the viscosity significantly, so the ejectors almost keep their viscosities after ejection.

Now, we can plot the results of collisions among ejectors on the diagram that was obtained in the part I. The parameters are $r_1 = r_2 = 1$ mm and $\mu_1 = \mu_2 = 1$ poise. The symbol "plus" (+) in Fig. 38 shows our results of the impact parameter Im and the Weber number of impact We(impact) for each collision. The solid (dashed) curve shows the boundary between the "coalescence" and the "stretching separation" (the "coalescence" and the "disruption"). The dotted curve shows the boundary between the surface tension control case and the ram pressure control case. We can see that eleven out of twelve collisions detected in the run are in the "coalescence". In contrast, one collision is in the "stretching separation". Almost all collisions satisfy the condition for coalescence. However, the deformation of eleven collisions are controlled by the ram pressure of collisions, so the deformation proceeds before the solidification and the condition for keeping shape is not satisfied and these collisions do not lead to compound chondrule formation (see subsection 5.2.3).

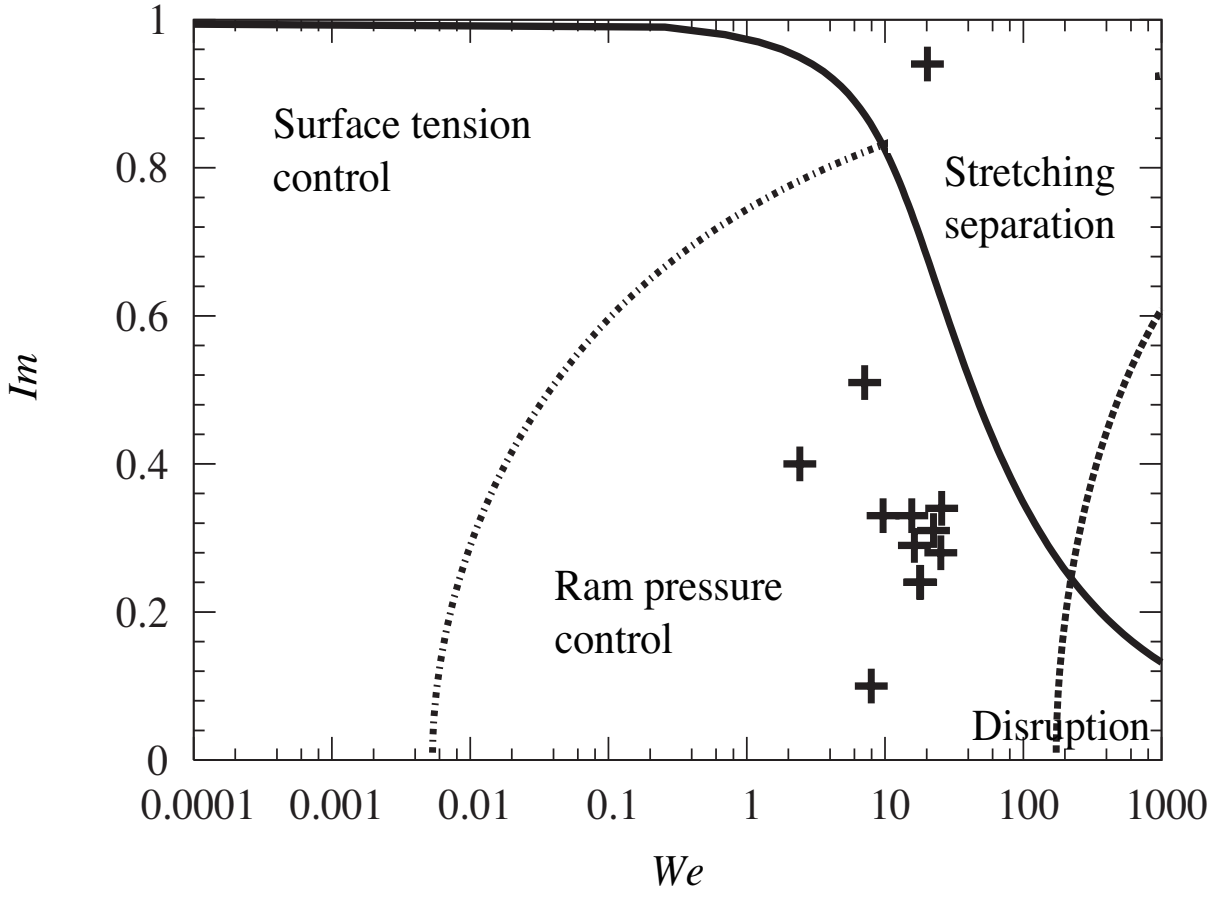

Figure 38: The diagram of collision conditions. The parameters are $r_1 = r_2 = 1$ mm and $\mu_1 = \mu_2 = 1$ poise. The solid, dashed, and dotted curves represent the boundary between "coalescence" and "stretching separation", boundary between "coalescence" and "disruption", and boundary between "surface tension control" and "ram pressure control", respectively. The symbols "plus" (+) plotted on this diagram show collisions of our numerical simulation.

10.4 Initial Condition and Parameter Dependence

10.4.1 Rotation of Parent Particle

In our simulation so far, we did not consider the rotation of the parent particle. However, in the shock-wave heating model, rotation of chondrule precursors is naturally expected and the rotation is important for the final shapes of chondrules (Miura et al. 2008b). In this case, the typical rotation period is much shorter than the cooling timescale (in which the chondrule shape is determined), so the rotation plays an important role. However, in this paper, we consider the disruption of molten particle, which is much faster than the rotation, so the rotation would not be so important.

The timescale of disruption and collision event is of the order of $\sim 10^{-2}$ sec (Table 2). On the other hand, the rotation timescale of a chondrule precursor of 5 mm in radius is

$$\begin{aligned} \omega_f &= 39.2 \left(\frac{f}{10^{-2}}\right)^{\frac{1}{2}} \left(\frac{p_{\rm fm}}{2\times 10^{-4}\ {\rm dyn\ cm^{-2}}}\right)^{\frac{1}{2}} \left(\frac{r_{\rm p}}{5\ {\rm mm}}\right)^{-1}\ {\rm rad\ s^{-1}}, \\ T_{\rm rot} &= \frac{2\pi}{\omega_f} = 0.16\ {\rm sec}, \end{aligned} \tag{72}$$

where f is the fraction of cross-section, which contributes to produce the net torque (Miura et al. 2008b). Since the timescale of disruption is an order of magnitude smaller than that of the rotation, the rotation is not so important for the dynamics of liquid part and ejectors.

However, the rotation may change the initial geometry of the liquid part because the heating timescale of the parent particle could be much longer than the rotation timescale. When the rotation is fast, the precursor particle is virtually heated axisymmetrically, and the liquid part would surround the solid core (figure 40). We have carried out a simulation with such an initial setting. Figure 39 shows the hydro-

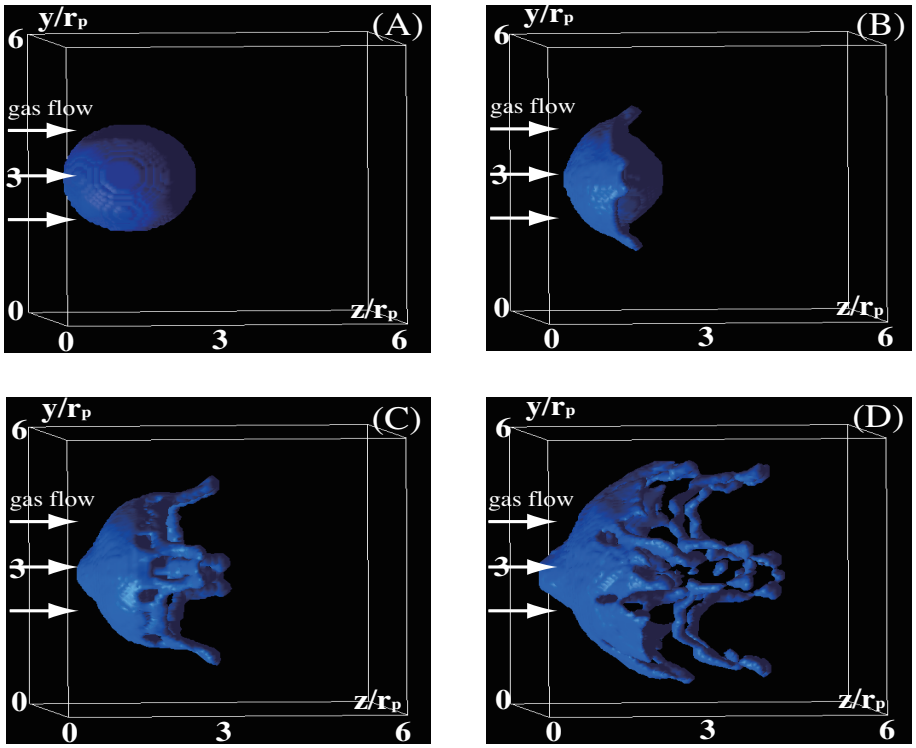

Figure 39: Hydrodynamics evolution of the parent particle with a cylindrical initial liquid part.

dynamics evolution of the parent particle whose liquid part surrounds the solid core (panel A). The radius of the parent particle is 5 mm, the radius of the solid core is 2.5 mm, and the ram pressure of the gas flow is 4.0×10^4 dyn cm^{-2}. First, the liquid part facing to the gas flow is stretched in $x - y$ plane by the gas flow (panel B), then this part is stretched to the z direction (panel C), and eventually it is disrupted into small ejectors (panel D). We can see that the fundamental result does not change significantly even if we consider the rotation of the parent dust particle.

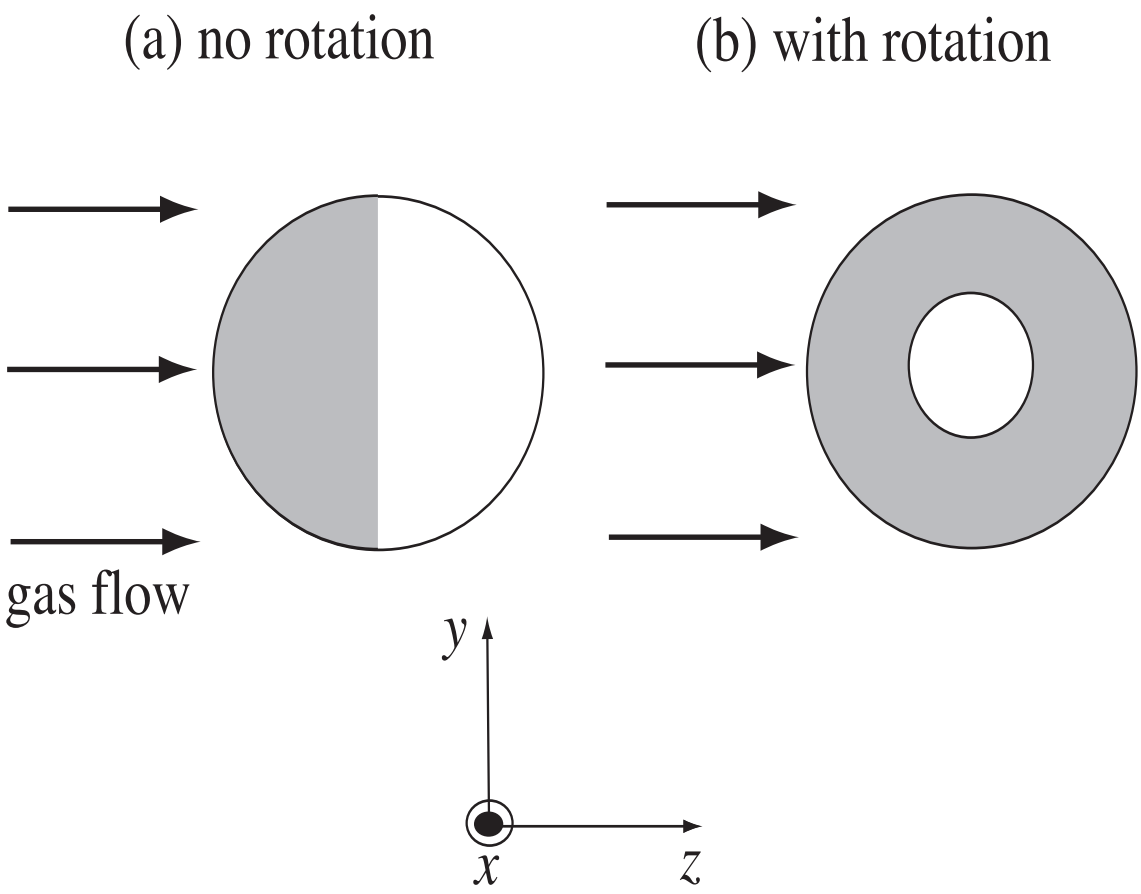

Figure 40: A schematic picture of the liquid part (grey zone) in the case of no rotation (panel a) and with fast rotation (panel b). In panel (b), the dust particle rotates around the x-axis and it is heated axi-symmetrically.

10.5 Initial Geometry and Parameter Dependence

We described and discussed the disruption of a spherical parent particle with only one limited setting (initial geometry of the liquid part, the radius of parent particle, and the ram pressure of the gas flow) in detail. However, it is unlikely that the initial geometry of chondrule precursors is a spherical shape. So one may concern that a different initial geometry and/or different parameter sets would lead to a different result. In order to examine this concern, we have carried out some parameter

sets and the initial settings. And we have found that the essential results (i.e., a liquid part is stripped off by the fast gas flow, the arm-like structure is made, that structure is disrupted, many ejectors are ejected, and they are collided each other by shadow effect) are almost the same as the results described in detail in section 9 and subsection 10.5.

10.6 Other Possibilities

In the previous section, we concluded that it is difficult to form compound chondrules from collisions between ejectors just after disruption from the view point of collision conditions. In this subsection, we consider some possibilities that overcome this difficulty.

10.6.1 Viscosity Difference in the Parent Particle

The first possibility is that there is an initial temperature (viscosity) difference between two ejectors at the time of the ejection. A cm-sized, non-rotating dust particle heated by the shock-wave heating mechanism has a temperature inhomogeneity of about a several hundred K inside the particle (Appendix E). Thus if an ejector extracted from the lower temperature part collides with another ejector from a higher temperature part, that collision would result in a compound chondrule formation because one ejector has been already stiffer than the other. In order to examine this idea, we have to solve the temperature evolution inside the particle taking into account the hydrodynamic disruption. It requires an improvement our code, such as an implementation involving the energy equation with the heat conduction, the gas drag heating, and the radiative cooling. This would be a challenging project. We are planning to develop such a numerical simulation code and carry out the

thermo-hydrodynamics simulations in the future (Appendix F).

10.6.2 Multiple Disruption Event

The second possibility is that the multiple disruption of the parent particle leads to form compound chondrules. During and after the disruption event, the parent dust particle is kept heated by the gas flow, the melted part increases again, and when the width of the melted part reaches the critical value, the second disruption event occurs. First ejectors move away to the direction of the gas flow and cool significantly during the reheating event of the parent particle. If second ejectors catch up with the first ejectors it may be possible to satisfy the condition for keeping shape because they are cooled significantly. It should be noted that these collisions are always collisions between the larger first ejectors and the smaller second ejectors because the acceleration of a smaller ejector is larger than that of a larger ejector.

We simply estimate the dynamics and the temperatures (viscosities) evolution of the ejectors, and then we examine whether the collisions satisfy the condition for keeping shape or not. Figure 41 is a schematic picture of the multiple disruption model. The interval of time between the first disruption and the second disruption $t_{\rm h}$ can be approximately estimated from the heating time scale of the parent particle as $t_{\rm h} \sim 1$ sec for the number density of the gas is 10^{16} cm^{-3} and the shock velocity is 6 km s^{-1}. If we define the time interval between the second disruption and the collisions as $t_{\rm p}$, the travel distance of the first ejector is

$$L_1 = \frac{1}{2} a_1 (t_{\rm h} + t_{\rm p})^2 + v_{01}(t_{\rm h} + t_{\rm p}), \tag{73}$$

where $a_1 = 3p_{\rm fm}/4r_1\rho_{\rm d}$ and v_{01} are the acceleration of the ejector whose radius is r_1 and the initial velocity of the ejector. On the other hand, the travel distance of the

second ejector is

$$L_2 = \frac{1}{2}a_2 t_{\rm p}^2 + v_{02} t_{\rm p}, \tag{74}$$

where $a_2 = 3p_{\rm fm}/4r_2\rho_{\rm d}$ and v_{02} are the acceleration of the ejector whose radius is r_2 and the initial velocity of the ejector. From equations (73) and (74), we have

$$t_{\rm p} = \frac{(v_{02} - v_{11}) - \sqrt{(v_{02} - v_{11})^2 - 2a_1(1 - \frac{1}{\Delta})l_1}}{a_1(1 - \frac{1}{\Delta})}, \tag{75}$$

where l_1, v_{11}, and Δ are the travel distance of the ejector1 at $t_{\rm h}$, that is, $l_1 = \frac{1}{2}a_1 t_{\rm h}^2 + v_{01} t_{\rm h}$, the velocity at $t_{\rm h}$, that is, $v_{11} = v_{01} + a_1 t_{\rm h}$, and the size ratio of the ejectors, that is, $\Delta = r_2/r_1$. We approximately obtain the relation between $t_{\rm p}$ and $t_{\rm h}$ as,

$$\frac{t_{\rm p}}{t_{\rm h}} = \frac{\Delta + \sqrt{\Delta}}{1 - \Delta}, \tag{76}$$

where we use $v_{02} << v_{11}$ and $v_{11} \sim a_1 t_{\rm h}$.

The relative velocity between the ejector1 and the ejector2 at their collision can be calculated by

$$\begin{aligned} \Delta v &= v_{02} + a_2 t_{\rm p} - (v_{11} + a_1 t_{\rm p}), \\ &\sim v_{11} + (\frac{1}{\Delta} - 1)a_1 t_{\rm p}. \end{aligned} \tag{77}$$

The ejectors cool as the relative velocity between the gas and the ejectors decreases. The temperature evolution can be written by

$$T(t) = \Big(\frac{\rho_{\rm g} v_{\rm t}^3}{2\sigma}\Big)^{\frac{1}{4}}, \tag{78}$$

where $\rho_{\rm g}$ and $v_{\rm t}$ are the mass density of the gas and the relative velocity between the gas and the ejector; $v_{\rm t} = \frac{v_{\rm rel,0}}{1 + t/\tau_{\rm stop}}$ (Appendix E.2.1). The initial relative velocity $v_{\rm rel,\ 0}$ is related to the initial temperature of ejector T_0 as

$$T_0 = \Big(\frac{\rho_{\rm g} v_{\rm rel,0}^3}{2\sigma}\Big)^{\frac{1}{4}}. \tag{79}$$

The time evolution of the temperature of the ejector can be calculated from Eqs. (78) and (79) as,

$$T(t) = \Big(\frac{\tau_{\rm stop}}{\tau_{\rm stop} + t}\Big)^{\frac{3}{4}} T_0. \tag{80}$$

Then, we can estimate the temperatures of the ejectors as $T_1 = T(t_{\rm h} + t_{\rm p})$ and $T_2 = T(t_{\rm p})$. For example, in the case of $r_1 = 1$ mm and $\Delta = 0.3$, $t_{\rm p} \sim 1.2$ sec, $\Delta v \sim 1$ kms^{-1}, $T_1 \sim 1740$ K ($\mu_1 \sim 10^2$ poise), and $T_2 \sim 1520$ K ($\mu_2 \sim 10^6$ poise). These collisions are surface tension control cases (the left panel of figure 41) and satisfy the condition for keeping shape (the right panel of figure 41).

While the multiple disruption model satisfies the condition for keeping shape, there are two problems. First, from our simple estimation above, the second ejector is cooler than the first ejector when they collide. It seems to be against the relationship between the primary and the secondary. In order to satisfy the condition $T_1 < T_2$, the relation between $t_{\rm h}$ and $t_{\rm p}$ should satisfy

$$\frac{t_{\rm p}}{t_{\rm h}} < \frac{\Delta}{1 - \Delta}. \tag{81}$$

This condition cannot be satisfied (see Eq. 76). However, the multiple disruption event depends on the heating process of the parent dust particle significantly. In order to investigate this event in detail, we have to carry out the thermo-hydrodynamics simulations. It would be carried out in the near future (Appendix F). In addition, as we noted in Part I, the solidification process may depend not only on the cooling process but also on the crystallization processes. It may be possible that the first ejectors is stiff when the collision occurs because the first ejector has more chances to collide with a small dust particles than the second ejector.

Second, the number density of ejectors far from the parent particle is much smaller than that beside it, so the rate of collisions would decrease significantly. We have to

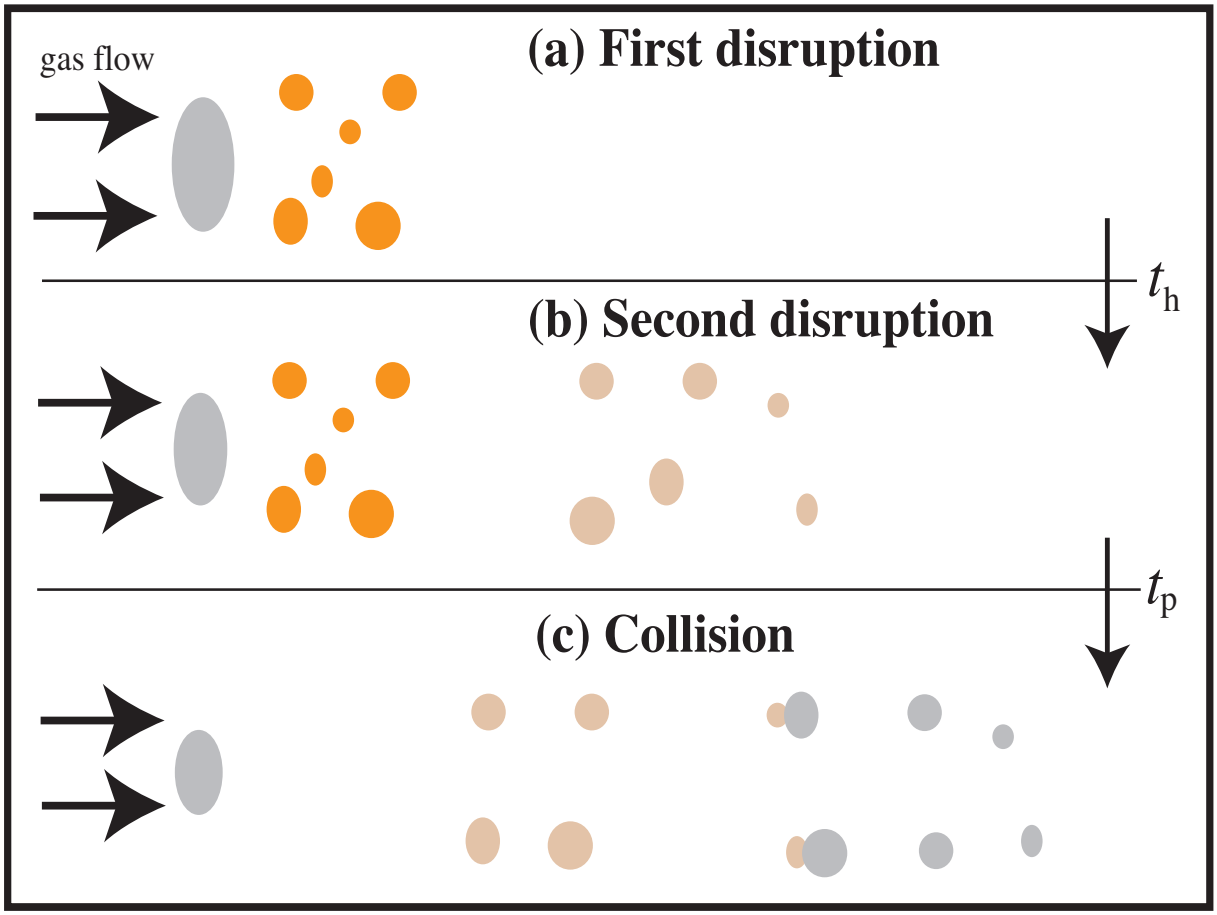

Figure 41: A schematic picture of the multiple disruption model.

examine the orbit of each ejector in order to see whether collisions occur at such a low-density region or not.

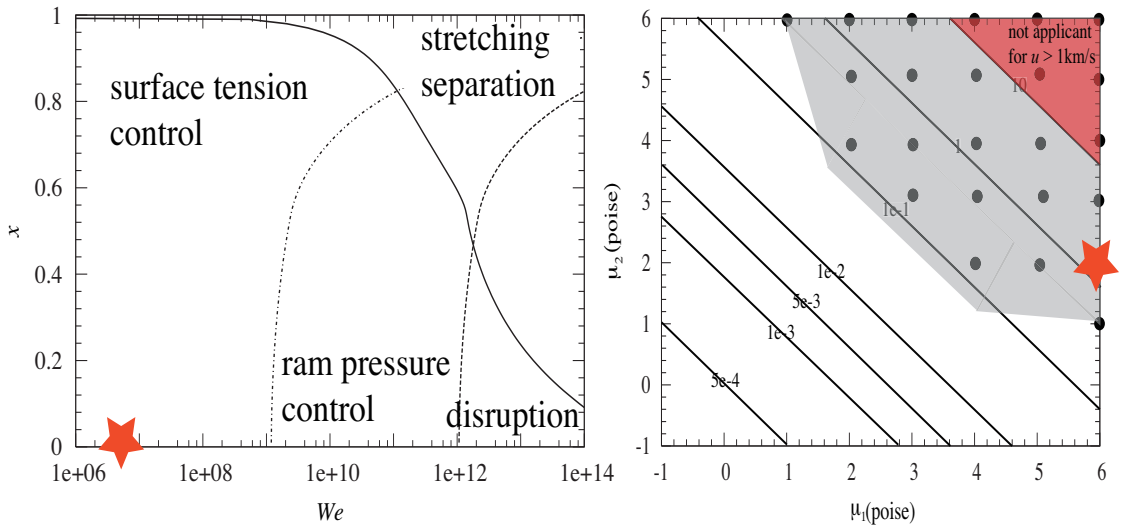

Figure 42: Collision conditions for multiple disruption event. The left panel shows the collisions (red star) that belong to the surface tension control case and the right panel shows the collisions (red star) that satisfy the condition for keeping shape.

11 Summary of Part II

We carried out three-dimensional hydrodynamics simulations and examined disruption of the partially-molten dust particle (parent particle) exposed to the high-speed gas flow and the dynamics of fragments in the framework of the shock-wave heating model. We discussed whether the collisions among these fragments contribute to the formation of compound chondrules. In this part, we described in detail the simulation results of a case in which the radius of the parent particle is 5 mm and the ram pressure of gas flow is 2×10^4 dyn cm^{-2}.

The disruption of the molten surface of the parent particle proceeds as follows. The molten surface stretches due to the gas ram pressure and then some arm-like structures are formed. The arm-like structures are disrupted into 32 small fragments. These fragments are accelerated by the gas flow, while the parent particle is not significantly done because of its larger mass. Therefore, the fragments are parted from the parent particle with time.

The size distribution of the fragments has an exponential form proportional to $\exp(-d_{\rm e}/b)$ with the fragment diameter $d_{\rm e}$ and the characteristic size b of 0.756 mm. The exponential size distribution was also observed in the aerodynamic disruption experiments of Kadono and Arakawa (2005).

The ejection velocities of fragments were almost axisymmetric around the axis across the center of the parent particle, which is parallel to the direction of the gas flow. Although this radial velocity distribution seems to be unfavorable for the mutual collisions among fragments, we detected twelve collisions by the end of the run. We analyzed the orbits of all the fragments in detail and found that the shadow effect is important. An ejector ejected earlier is not accelerated by the gas flow due

to the shadow effect, while an ejector ejected later is accelerated by the gas flow. The shadow effect causes the mutual collisions among fragments effectively.

Although we carried out the simulation for a typical parameter set and an initial geometry of the parent dust particle, the fundamental results (i.e., a liquid part is stripped by the fast gas flow, the arm-like structure is made by the gas flow, this structure disrupts, many ejectors are ejected, and the ejectors collide each other by shadow effect) are not affected by the initial geometry, the rotation of the parent dust particle, and other parameters.

It is important for compound chondrule formation that collisions among fragments satisfy appropriate collision conditions. We examined the collision parameters of all the collisions and compared with the collision conditions obtained in Part I. We found that eleven collisions resulted in coalescence. However, these eleven collisions belong to the ram pressure control case. This means that all collisions do not satisfy the condition for keeping shape and it seems difficult to form compound chondrules by collisions just after disruption event.

Finally, we considered two possibilities to form compound chondrules in the fragment-collision model. First one is a case where there is a temperature (viscosity) difference between two ejectors at the time of ejection occurs. And second case is the one where the collision among the ejectors that are from different disruption event. In order to discuss these possibilities in detail, we have to carry out thermo-hydrodynamics simulations.

12 Summary

We have simulated two molten silicate drop collisions for a wide range of collision parameters (the collision velocity, the collision angle, diameters of drops, and the viscosities of drops) with three-dimensional hydro-dynamics simulations in order to examine the collision conditions for compound chondrule formation. Collision conditions consist of two conditions; condition for coalescence and condition for keeping shape.

- Condition for Coalescence

We have found that collision outcomes can be classified into three categories. For close to head-on and lower relative velocity collisions, "coalescence" occurs because the kinetic energy for stretching two drops is dissipated by the surface energy of interaction region, the viscous dissipation of drops, and the rotational energy. For grazing collisions, "stretching separation" occurs because the stretching kinetic energy overcomes energy dissipations. For close to head-on and higher relative velocity collisions, "disruption" occurs because the kinetic energy for deformation increases the surface energy to exceeds the critical value.

- Condition for Keeping Shape

In order to keep drops shape, the deformation timescale should be longer than the solidification timescale. The deformation is controlled by ram pressure of the collision and the surface tension. When the relative velocity is high, the deformation is mainly controlled by ram pressure of the collision (ram pressure control case) and the deformation time can be interpreted as the transit time of the two drops. On the contrary, when the relative velocity is low, the deformation is mainly controlled by

the surface tension (surface tension control case) and the deformation time depends only on the diameters and the viscosities of the two drops. We found that the deformation of the large drop is modeled by the oscillation of a viscoelastic body and the deformation time can be written as a quarter of the period of damped oscillation. Moreover, we found that the boundary between these two cases can be obtained from the balance between the kinetic energy which works deformation of the large drop and the viscous dissipation just after collision.

The solidification time is difficult to estimate because the crystallization processes by collision have not been understood well. In this paper, we assume that the seed of the crystal occurs at the interaction case and define the solidification time as the growth time of crystal. It is the lower limit of the solidification time, so we can obtain the least viscosities of drops to satisfy the condition for keeping shape. In the ram pressure control case, the deformation time is longer than the solidification time for every viscosity, so it seems to be difficult to form compound chondrule by the collision in the ram pressure control case. In the surface tension control case, the deformation time is longer than the solidification time for more than about 330 poise. Therefore, in order to satisfy the condition for keeping shape, the collision should be in the surface tension control case and the viscosities of the two drops are, at least, more than about 330 poise.

Now, we obtain the collision conditions for compound chondrule formation quantitatively. Since we analytically understood the phenomena of drop collisions, we can know the conditions by not using numerical simulation for wide range of collision parameters and verify the formation models.

We have verified the “Fragment-Collison in the shock-wave heating model”, which is one of the plausible models for compound chondrule formation, proposed by Miura et al. (2008). We carried out three-dimensional hydrodynamics simulations and examined the disruption of a partially-molten dust particle exposed to high-speed gas flow and the dynamics of fragments in order to obtain the collision parameters of collisions among the fragments. We mainly described the simulation results of a case in which the radius of the parent particle is 5 mm and the ram pressure of the gas flow is 2×10^4 dyn cm^{-2} in detail.

The disruption of the molten surface of the parent particle proceeds as follows. The molten surface stretches due to the gas ram pressure and then some arm-like structures are formed. The arm-like structures are disrupted into 32 small fragments. These fragments are accelerated by the gas flow, while the parent particle is not significantly done because of its larger mass. Therefore, the fragments are parted from the parent particle with time.

The ejection velocities of fragments were almost axisymmetric around the axis across the center of the parent particle, which is parallel to the direction of the gas flow. Although this radial velocity distribution seems to be unfavorable for the mutual collisions among fragments, we detected twelve collisions by the end of the run. We analyzed the orbits of all the fragments in detail and found that the shadow effect is important. An ejector ejected earlier is not accelerated by the gas flow due to the shadow effect, while an ejector ejected later is accelerated by the gas flow. The shadow effect causes the mutual collisions among fragments effectively.

We also carried out some numerical simulations for other parameter and initial geometries. As a result, we found that the fundamental results are not affected

by the initial geometry of melted part, the rotation of the parent particle, and the parameters (the thickness of the liquid part, the radius of the parent particle, the ram pressure of the gas flow).

It is important for compound chondrule formation that collisions among fragments satisfy appropriate collision conditions. We examined the collision parameters of all the collisions and compared with the collision conditions obtained in Part I. We found that eleven collisions resulted in coalescence. However, these eleven collisions belong to the ram pressure control case. This means that all collisions do not satisfy the condition for keeping shape and it seems difficult to form compound chondrules by collisions just after disruption event.

Finally, we considered two possibilities to form compound chondrules in the fragment-collision model. First one is a case where there is a temperature (viscosity) difference between two ejectors at the time of ejection occurs. And second case is the one where the collision among the ejectors that are from different disruption event. In order to discuss these possibilities in detail, we have to carry out thermo-hydrodynamics simulations.

A Energy Dissipations

In order to compare the energy dissipations, we estimate them in the condition of $\Delta = 1$. In this case, $\phi_1 = \phi_2$, $\tau = 2(1-x)$, and $h = d_2(1-x)$. The magnitude of the surface energy at the interaction part is given by

$$\begin{aligned} S &= \sigma\Big(4\pi V_2 d_2 \tau \phi_2\Big)^{\frac{1}{2}} \\ &= 17.8\ (\tau\phi_2)^{\frac{1}{2}}\ \mathrm{erg}\ \Big(\frac{d_2}{1\ \mathrm{mm}}\Big)^2, \end{aligned} \tag{82}$$

where ϕ_2 is given by

$$\phi_2 = \begin{cases} 1 - \frac{1}{4}(2-\tau)^2(1+\tau) & \text{for} \quad x \geq 0.5, \\ \frac{\tau^2}{4}(3-\tau) & \text{for} \quad x \leq 0.5. \end{cases} \tag{83}$$

The magnitude of the viscous dissipation is given by

$$\begin{aligned} E_{\mathrm{vis}} &= \frac{2u}{h}\Big(\mu_2 \phi_2 V_2\Big) \\ &= 6.28\ \phi_2\ \mathrm{erg}\ \Big(\frac{d_2}{1\ \mathrm{mm}}\Big)^2 \Big(\frac{u}{100\ \mathrm{cm\ s^{-1}}}\Big)\Big(\frac{\mu_2}{1\ \mathrm{poise}}\Big)\Big(\frac{1-x}{0.5}\Big)^{-1}. \end{aligned} \tag{84}$$

And the magnitude of the rotational energy is given by

$$E_{\mathrm{rot}} = 0.58\ \mathrm{erg}\ \Big(\frac{d_2}{1\ \mathrm{mm}}\Big)^3 \Big(\frac{u}{100\ \mathrm{cm\ s^{-1}}}\Big)^2 \Big(\frac{x}{0.5}\Big)^2. \tag{85}$$

From the estimation above, we can see that the dissipation by the surface energy is the most effective one at lower viscosity ($\mu_1,\ \mu_2 \lesssim 1$ poise) and lower relative velocity ($u \lesssim 200$ cm s^{-1}, corresponding Weber number is 30). In the larger viscosity case (more than ~ 10 poise), the viscous dissipation is the most effective one among three. In contrast, in the case of water drops ($\mu_{\mathrm{water}} \sim 10^{-2}$ poise), the viscous dissipation is much less than the dissipation by the surface energy and the rotational energy. Rotational energy is much less than the dissipation by the surface energy and the viscous dissipation for lower relative velocity. However, for larger relative velocity

($u \gtrsim 400$ cm s^{-1}, corresponding Weber number is 120), this is the most effective one among three.

B Disruption and Reflexive Separation

In our numerical simulations, the outcome "Disruption" appears instead of "Reflexive separation", which appeared in experiments with low viscosity fluids like water and hydrocarbons. Critical Weber numbers for "Reflexive separation" were investigated by some authors experimentally as a function of the Ohnesorge number ($Oh \equiv \mu_2/(\sigma\rho_2 d_2)^{1/2}$), which indicates the ratio of viscous effects to surface tension effects, Gotaas et al. (2007) summarized these data with their experimental data sets (figure 9). For the parameter set used in our simulation, $Oh \sim 0.09$. It indicates that the critical Weber number for "Reflexive separation" ($We_{\rm ref}$) is about 200. On the other hand, our numerical results and theory indicates that the critical Weber number for "Disruption" ($We_{\rm dis}$) is about 120.

C Energy Equation

The energy equation has various source terms on the right hand side of Eq. (8), such as, thermal diffusion, viscous dissipation, gas frictional heating, radiative cooling, and radiative heating due to the ambient radiation field. However, we ignore these terms because their timescales are much longer than that of the advection term in Eq. (8). We estimate these timescales in this appendix.

The timescale of advection can be estimated from the fluid-crossing time $t_{\rm adv} \sim$

$r_{\rm p}/v_{\rm max}$ where $v_{\rm max}$ is the maximum internal velocity of the drop exposed to the gas flow. We adopt the formalism obtained by the linear analysis of $v_{\rm max} \simeq 0.1 p_{\rm fm} r_{\rm p}/\mu_{\rm d}$ (Sekiya et al. 2003) and then

$$t_{\rm adv} \sim \frac{\mu_{\rm d}}{0.1 p_{\rm fm}} \simeq 5 \times 10^{-4} \ {\rm sec} \left(\frac{p_{\rm fm}}{2 \times 10^4 \ {\rm dyn \ cm^{-2}}} \right)^{-1} \left(\frac{\mu_{\rm d}}{1 \ {\rm poise}} \right). \quad (86)$$

The timescale of thermal diffusion is estimated by

$$t_{\rm cond} \sim \frac{r_{\rm p}^2}{a} \simeq 25 \ {\rm sec} \left(\frac{r_{\rm p}}{5 \ {\rm mm}} \right)^2 \left(\frac{a}{10^{-2} \ {\rm cm^2 \ s^{-1}}} \right)^{-1}, \quad (87)$$

where a is the thermal diffusivity. The timescale of viscous dissipation can be estimated by $t_{\rm vis} \sim \rho_{\rm d} C T/\dot{e}_{\rm vis}$, where T is the temperature of molten dust particles and $\dot{e}_{\rm vis}$ is the energy dissipation rate per unit volume. The dissipation rate is an order of $\dot{e}_{\rm vis} = \mu_{\rm d} (\partial u_i/\partial x_j)^2 \sim \mu_{\rm d} v_{\rm max}^2/r_{\rm p}^2$, so we obtain

$$\begin{aligned} t_{\rm vis} &\sim \frac{\mu_{\rm d} \rho_{\rm d} C T}{0.01 p_{\rm fm}^2} \\ &\simeq 2 \times 10^4 \ {\rm sec} \left(\frac{p_{\rm fm}}{2 \times 10^4 \ {\rm dyn \ cm^{-2}}} \right)^{-2} \left(\frac{\mu_{\rm d}}{1.0 \ {\rm poise}} \right) \left(\frac{T}{2000 \ {\rm K}} \right). \end{aligned} \quad (88)$$

Therefore, the advection is much more efficient to change the internal temperature distribution inside the molten dust particle than the thermal conduction and the viscous dissipation.

The overall temperature of the dust particle changes by the input/output of energy by the gas frictional heating, radiative cooling, and radiative heating due to the ambient radiation field. However, the timescales of these processes are much longer than the time duration of interest in this study. The timescale of the gas frictional heating is given by (see also Appendix A of Miura et al. 2008b)

$$\begin{aligned} t_{\rm heat} &\sim \frac{8 r_{\rm p} \rho_{\rm d} C T}{3 \rho_{\rm g} v_{\rm rel}^3} \\ &\simeq 130 \ {\rm sec} \left(\frac{r_{\rm p}}{5 \ {\rm mm}} \right) \left(\frac{\rho_{\rm g}}{4 \times 10^{-9} \ {\rm g \ cm^{-3}}} \right)^{-1} \end{aligned}$$

$$\left(\frac{v_{\rm rel}}{6\ {\rm km\ s^{-1}}}\right)^{-3}\left(\frac{T}{2000\ {\rm K}}\right). \tag{89}$$

The timescale of the radiative cooling is (see also Eq. 28 of Miura et al. 2008a)

$$\begin{aligned} t_{\rm cool} &\sim \frac{r_{\rm p}\rho_{\rm d}CT}{3\epsilon_{\rm emit}\sigma T^4} \\ &\simeq 160\ {\rm sec}\left(\frac{r_{\rm p}}{5\ {\rm mm}}\right)\left(\frac{\epsilon_{\rm emit}}{0.1}\right)^{-1}\left(\frac{T}{2000\ {\rm K}}\right)^{-3}, \end{aligned} \tag{90}$$

where σ and $\epsilon_{\rm emit}$ are the Stefan-Boltzmann constant and the emissivity of the dust particle. The timescale of the radiative heating due to the ambient radiation filed is given by (also see Eq. 28 of Miura et al. 2008a)

$$\begin{aligned} t_{\rm heat} &\sim \frac{r_{\rm p}\rho_{\rm d}CT}{3\epsilon_{\rm abs}\sigma T_{\rm rad}^4} \\ &\sim 2500\ {\rm sec}\left(\frac{r_{\rm p}}{5\ {\rm mm}}\right)\left(\frac{\epsilon_{\rm abs}}{0.1}\right)^{-1}\left(\frac{T}{2000\ {\rm K}}\right)\left(\frac{T_{\rm rad}}{1000\ {\rm K}}\right)^{-4}, \end{aligned} \tag{91}$$

where $T_{\rm rad}$ is the temperature of the ambient radiation field and $\epsilon_{\rm abs}$ is the absorption coefficient. As shown above, these timescales are much longer than the disruption timescale in this study (~ 0.01 sec). Therefore, we ignore these terms in the energy equation.

D Temperature Inhomogeneity in a Dust Particle

In the shock-wave heating model, the dust particle is exposed to the fast gas flow and heated by the gas frictional heating. In this appendix, we examine the temperature distribution in the dust particle exposed to the gas flow with three-dimensional heat conduction calculation code.

D.1 Numerical Simulation

D.1.1 Color Function

Figure 43 shows the schematic picture of our numerical calculation model and the coordinate system. We adopt the Cartesian coordinate system (x, y, z). In order to express the dust particle, that is, the silicate dust particle in the calculation region, we use color function ϕ, which takes the value of unity ($\phi = 1$) inside the dust particle and zero ($\phi = 0$) in the other region. For initial condition, the gas flow is parallel to the x-axis and when we consider the rotation of the dust particle, we rotate the direction of the gas flow (Fig 43B).

D.1.2 Energy Equation

The energy equation of the dust particle is written as

$$\frac{dT}{dt} = \frac{\lambda}{\rho C}\Delta T + \frac{S_{\rm eff}(\Gamma_{\rm g-d} - \Lambda_{\rm rad} + \Gamma_{\rm rad})}{\rho V C_{\rm eff}}, \tag{92}$$

where T, λ, C, ρ are the temperature, the heat conduction coefficient, the heat capacity, and the mass density of the dust particle, respectively. The mass density is given by

$$\rho = \rho_{\rm d} \times \phi + \rho_{\rm a} \times (1 - \phi), \tag{93}$$

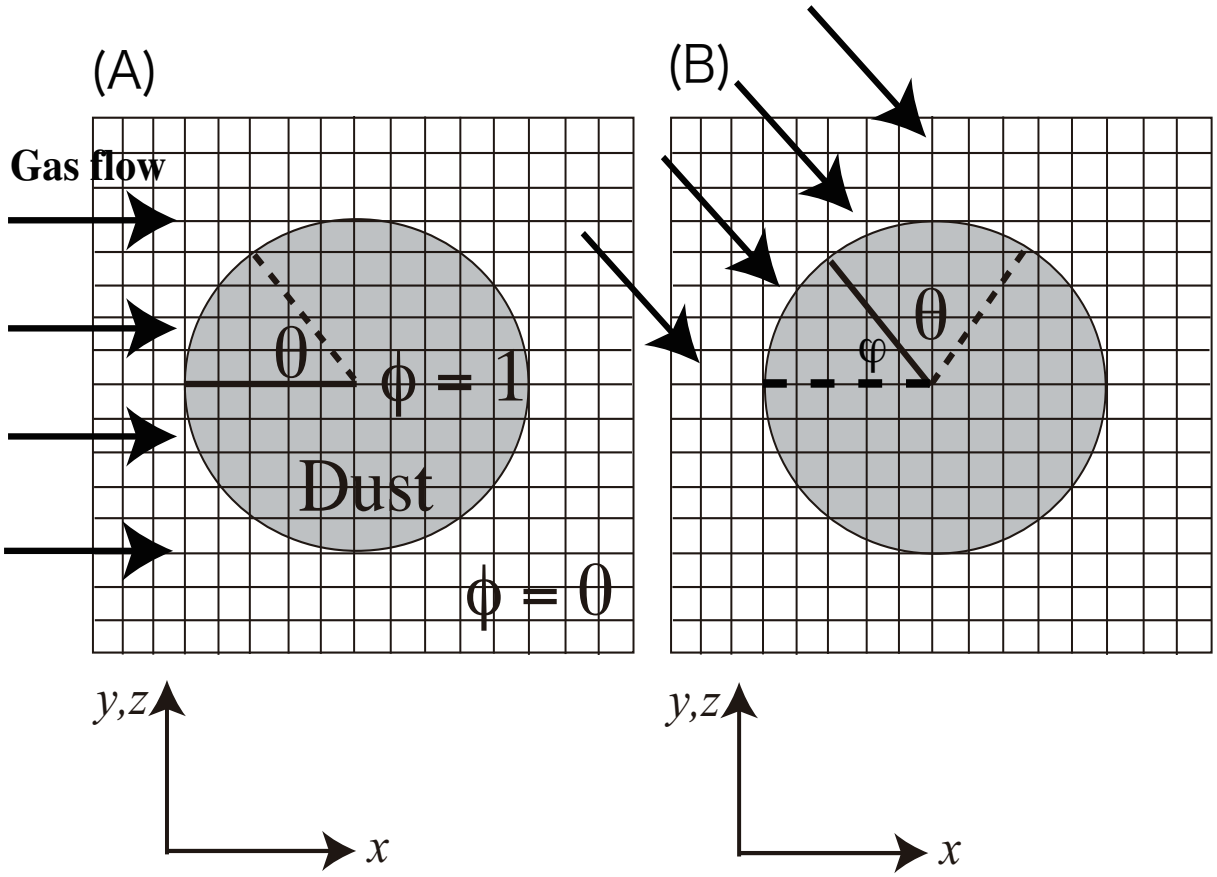

Figure 43: A schematic picture of our numerical model and the coordinate system. We set $\phi = 1$ in the dust particle and $\phi = 0$ in the ambient region. The allows show the direction of the gas flow.

where the subscripts "d" and "a" indicate the dust particle and the ambient region. The first, second, third, fourth terms of the right hand side of the Eq. (92) mean the heat conduction, the heat transfer between the gas and the dust particle, which includes the gas frictional heating, the radiative cooling of the dust particle, and the radiative heating due to the ambient radiation field, respectively. The effective surface area $S_{\rm eff}$ is explained in next subsection. The effective heat capacity $C_{\rm eff}$ means that it includes absorption of the latent heat of melting. We assume that the dust particle absorbs the latent heat ($L_{\rm melt}$) between the solidus temperature ($T_{\rm sol}$) and the liquidus temperature ($T_{\rm liq}$), so the effective heat capacity is written as

$$\begin{aligned} C_{\rm eff} &= C + \frac{L_{\rm melt}}{T_{\rm liq} - T_{\rm sol}}, \quad \text{for } T_{\rm sol} < T < T_{\rm liq}, \\ C_{\rm eff} &= C, \qquad\qquad\qquad \text{otherwise.} \end{aligned} \tag{94}$$

D.2 Detection of Surface and Effective Surface Area

The heating and cooling processes occur only on the surface of the dust particle. We have to detect the surface of the dust particle in the calculation box. Let us consider one of the cell (Figure 44). We can judge whether a surface is exposed to outside or not from the inner product of the normal vector of a surface ($\boldsymbol{n}_{m,i,j,k}$) and the gradient of the color function ($\boldsymbol{\nabla}\bar{\phi}$), where $\bar{\phi}$ is the smoothed profile of the color function (Miura et al. 2007).

$$\boldsymbol{\nabla}\bar{\phi} = \Big(\frac{\bar{\phi}_{i+1,j,k} - \bar{\phi}_{i-1,j,k}}{2dx}, \ \frac{\bar{\phi}_{i,j+1,k} - \bar{\phi}_{i,j-1,k}}{2dy}, \ \frac{\bar{\phi}_{i,j,k+1} - \bar{\phi}_{i,j,k-1}}{2dz}\Big). \tag{95}$$

If the inner product, $\boldsymbol{n}_{m,i,j,k} \cdot \boldsymbol{\nabla}\bar{\phi}$, is negative, this surface is exposed to outside and vice versa. However if we detect the surface in this way, we overestimate the surface area of the dust particle because we use Cartesian coordinate and the dust particle is expressed by cubes (cells), so the surface area of the dust particle is different from

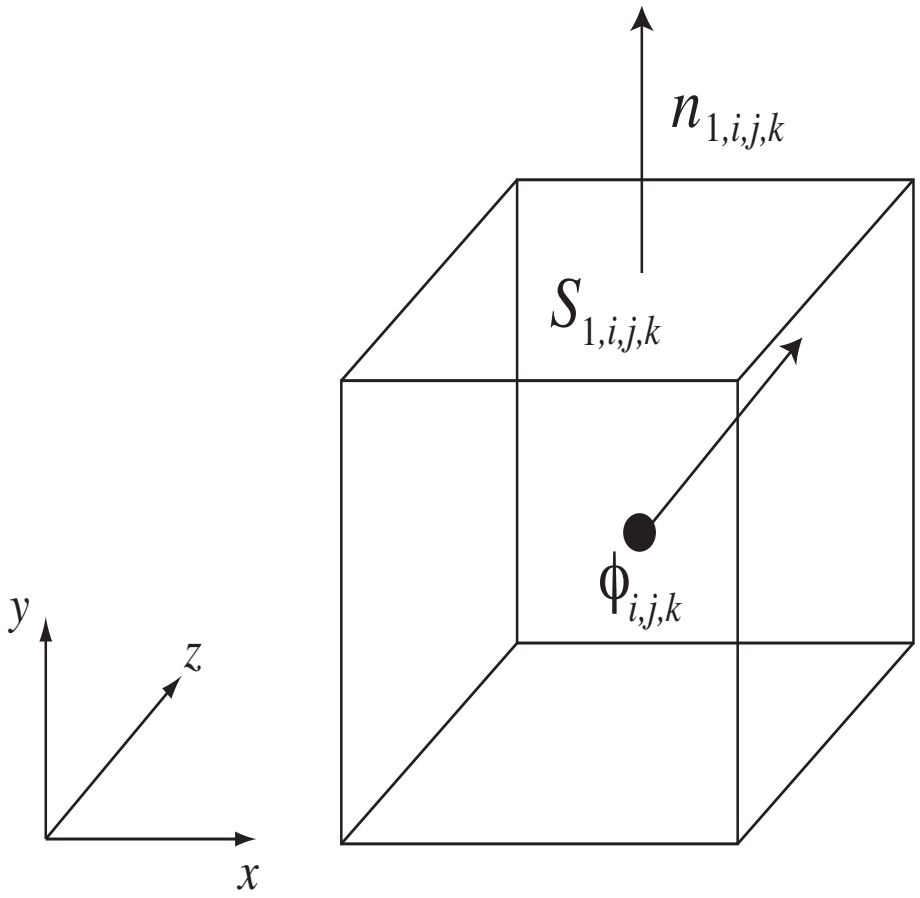

Figure 44: A cell in the computational box.

that of sphere. In order to avoid this difficulty, we define the effective surface area $S_{\rm eff}$. The effective surface area of the top surface of the cell is given by

$$\begin{aligned} S_{1,i,j,k} &= (\bar{\phi}_{i,j+1,k} - \bar{\phi}_{i,j,k})dxdz \quad \text{if } \boldsymbol{n}_{1,i,j,k} \cdot \boldsymbol{\nabla}\bar{\phi}_{i,j,k} < 0, \\ S_{1,i,j,k} &= 0 \qquad\qquad\qquad\qquad\quad \text{if } \boldsymbol{n}_{1,i,j,k} \cdot \boldsymbol{\nabla}\bar{\phi}_{i,j,k} > 0. \end{aligned} \tag{96}$$

The effective surface of a cell is the sum of six aspects, that is,

$$S_{\rm eff} = \sum_{m=1}^{6} S_{m,i,j,k}. \tag{97}$$

We confirm that the sum of the effective surface area corresponds to the surface area of the sphere.

D.2.1 Energy Flux

1. Gas Drag Heating

We can treat the gas flow as the free molecular flow, because the number density of the nebular gas is too rarefied (Iida et al. 2001, Miura et al. 2007). In this case, the flux of the heat transfer between the gas and the dust surface $\Gamma_{\rm g-d}$ is written as

$$\Gamma_{\rm g-d} = n_{\rm post} v_{\rm m} (T_{\rm rec} - T) C_{\rm H}, \tag{98}$$

where $n_{\rm post}$, $v_{\rm m}$, $T_{\rm rec}$, and $C_{\rm H}$ are the number density of the gas in the post-shock region, the peak velocity of Maxwell distribution function that relates with the thermal velocity of the gas ($v_{\rm t}$) as $v_{\rm m} = v_{\rm t}\sqrt{\pi}/2$, the recovery temperature, and the heat transfer function, respectively. The recovery temperature $T_{\rm rec}$ and the heat transfer function $C_{\rm H}$ are given by

$$\begin{aligned} T_{\rm rec} &= T_{\rm g}\Big(1 + 2s^2 \frac{\gamma - 1}{\gamma + 1}\{\frac{2s^2 + (2s^2+1)B}{2s^2(1+B)}\}\Big), \\ C_{\rm H} &= \frac{1}{2\sqrt{\pi}} \exp(-s\cos^2\theta)(1+B)\frac{\gamma+1}{\gamma-1}\frac{k}{2}, \\ B &\equiv \sqrt{\pi} s\cos\theta(1 + {\rm erf}(s\cos\theta))\exp(s\cos\theta)^2, \end{aligned} \tag{99}$$

where θ is the angle from the line parallel to the gas flow (Fig 43), s is the ratio of the relative velocity between the gas and the dust particle (the relative velocity is related to the shock velocity; $v_{\rm rel} = 5v_{\rm sh}/6$ for $Ma >> 1$) to the thermal velocity of the gas, $s = v_{\rm rel}/v_{\rm t}$, ${\rm erf}(x)$ is the error function defined by ${\rm erf}(x) = 2/\sqrt{x}\int_0^x \exp(-t^2)dt$, and $T_{\rm g}$ is the temperature of the gas in the post-shock region. The gas temperature $T_{\rm g}$ in the post-shock region is typically about 2000 K according to Iida et al. (2001), which calculate the gas temperature in the post-shock region taking into account a lot of the physical and chemical processes.

The gas drag heating is decreased with time because the relative velocity between the gas and the dust particle is decreased due to the gas drag. The equation of motion of the dust particle in the post-shock region is given by

$$V\rho_{\rm d}\frac{dv_{\rm rel}}{dt} = -\rho_{\rm g}v_{\rm rel}^2\pi. \tag{100}$$

The solution of the above equation is

$$\begin{aligned} v_{\rm rel} &= \frac{v_{\rm rel}(t=0)}{t/\tau_{\rm stop}+1}, \\ \tau_{\rm stop} &\equiv \frac{4\rho_{\rm d}r_{\rm s}}{3m_{\rm g}n_{\rm g}v_{\rm rel}(t=0)}. \end{aligned} \tag{101}$$

Dust particles in the solar nebular were naturally thought to be irregular shaped. If the irregular shaped dust particle is exposed to the fast gas flow, the dust particle receives asymmetric torque and obtains rotational velocity (Miura et al. 2008). We consider the rotation of the dust particle into account. The direction of the direction of the gas flow rotates with time.

$$\psi = 2\pi f t, \tag{102}$$

where f is the rotation frequency and we treat it as free parameter.

2. Radiative Cooling

The energy flux of the radiative cooling of the dust particle is given by

$$\Lambda_{\rm rad} = \varepsilon\sigma T^4, \tag{103}$$

where ε and σ are the emissivity of the dust particle and Stefan Boltzman constant, respectively.

3. Radiative Heating

The energy flux of the radiative heating due to the ambient radiation field is given by

$$\Gamma_{\rm rad} = \varepsilon\sigma T_0^4, \tag{104}$$

where T_0 is ambient radiation temperature. In this study, we assume that the ambient radiation temperature is $T_0 = 1000$ K. This value does not change the calculation results very much.

D.2.2 Physical Parameters and Initial Condition

We investigate the time evolution of the temperature distribution in the dust particle for various radii of the dust particle, shock velocities, gas number densities, and rotation frequency. We assume that the initial temperature of the dust particle is homogeneous and equal to the radiation field temperature in the post-shock region, that is, $T(t = 0) = T_0 = 1000$K. We assume that the dust particle is forsterite (Mg_2SiO_4) and physical parameters of the dust particle is listed in Table 4.

Parameter	Notation	Value
Mass density of the dust	$\rho_{\rm d}$	3 g cm^{-3}
Mass density of the ambient	$\rho_{\rm a}$	10^{-15} g cm^{-3}
Specific heat	C	1.4×10^7 erg g^{-1} K^{-1}
Heat conductivity	λ	5.3×10^5 erg cm^{-1} s^{-1} K^{-1}
Latent heat	$L_{\rm melt}$	4.5×10^9 erg g^{-1}
Liquidus temperature	$T_{\rm liq}$	1900 K
Solidus temperature	$T_{\rm sol}$	1500 K
Emissivity	ε	0.1

Table 4: Input physical parameters for our numerical simulation.

D.3 Numerical Results

D.3.1 Evolution of Temperature Distribution

At first, we do not take rotation and deceleration of the dust particle due to the gas flow into account in order to understand the physics of the temperature distribution in detail. Figure 45(a) shows the temperature evolutions of the front (the solid curve), the center (the dashed curve), and the back (the dotted curve) of the dust particle. Parameters are $r_{\rm s} = 1$ mm, $v_{\rm sh} = 10$ km s^{-1}, and $n_{\rm post} = 2.0 \times 10^{14}$ cm^{-3}. At first, the temperature of the dust particle goes up due to the gas frictional heating. Around 50 second, the temperatures reach the peak values when the heating rate and the cooling rate are balanced. Figure 45(b) shows the temperature evolution of $r_{\rm s} = 5$ mm. Other parameters are the same as panel (a). We can see the heating rate at the beginning is smaller and the temperature difference is broader than those of panel (a). Figure 45(c) shows the temperature evolution of $v_{\rm sh} = 20$ km s^{-1}. Other parameters are the same as panel (a). The heating rate is bigger, the temperature difference is broader, and peak temperature is higher than those of panel (a). Figure 45(d) shows the temperature evolution of $n_{\rm post} = 4 \times 10^{14}$ cm^{-3}. Other parameters are the same as panel (a). It shows the same tendency with panel (c). From Fig. 45, we can see that the temperature evolution and temperature distribution depend on the radius of the dust particle, the shock velocity and the number density of gas.

D.3.2 Parameter Dependence

1. Heating Rate

If we assume the temperature in the dust particle is homogeneous, the heating

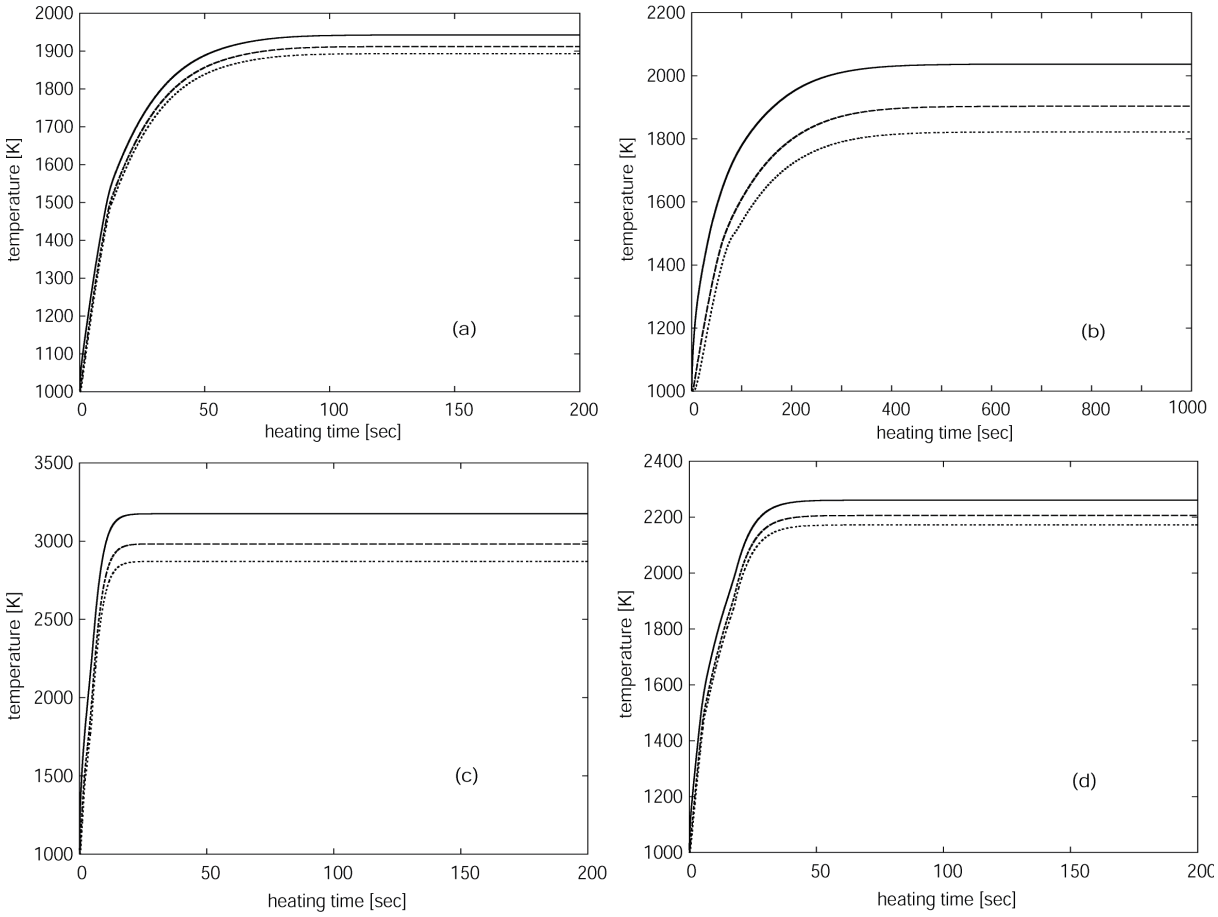

Figure 45: (a) The time evolution of the temperature in the dust particle vs heating time. Parameters are $r_{\rm s} = 1$ mm, $v_{\rm sh} = 10$ km s^{-1}, and $n_{\rm g} = 2.0 \times 10^{14}$ cm^{-3}. The solid, dashed, and dotted lines represent the front, center, and back of the dust particle. (b) The case with the radius of the dust particle $r_{\rm s} = 5$ mm. (c) The case with the shock velocity $v_{\rm sh} = 20$ km s^{-1}. (d) The case with number density of the gas $n_{\rm g} = 4 \times 10^{14}$ cm^{-3}.

rate of the dust particle just after beginning of heating can be written as

$$\begin{aligned} \rho_{\rm d} CV \frac{\partial T}{\partial t} &= \frac{1}{2} m_{\rm g} n_{\rm post} v_{\rm rel}^3 \pi r_{\rm s}^2, \\ \frac{\Delta T}{\Delta t} &= 35.5 \text{ K s}^{-1} \Big(\frac{n_{\rm post}}{2 \times 10^{14} \text{ cm}^{-3}} \Big) \Big(\frac{v_{\rm sh}}{10 \text{ km s}^{-1}} \Big)^3 \Big(\frac{r_{\rm s}}{1 \text{ mm}} \Big)^{-1}. \end{aligned} \quad (105)$$

This heating rate should be correspond to the numerical results of the heating rate of the center of the dust particle. we compare them in table 5. Cases (a) - (d) correspond to the parameter sets of figs. 42 (a) - (d). We can see that our numerical simulations show good agreement with the analytical calculations.

2. Peak Temperature

If we assume the temperature in the dust particle is homogeneous, peak temperature of the dust particle is understood by the balance between the heating rate and the cooling rate. So, we have,

$$\frac{1}{2} m_{\rm g} n_{\rm post} v_{\rm rel}^3 \pi r_{\rm s}^2 + 4\pi r_{\rm s}^2 \varepsilon \sigma T_0^4 = 4\pi r_{\rm s}^2 \varepsilon \sigma T^4, \quad (106)$$

$$T_{\rm peak} = 1829 \text{ K} \Big(\frac{n_{\rm post}}{2 \times 10^{14} \text{ cm}^{-3}} \Big)^{\frac{1}{4}} \Big(\frac{v_{\rm sh}}{10 \text{ km s}^{-1}} \Big)^{\frac{3}{4}}. \quad (107)$$

This peak temperature also compare with the calculation results in table 5. They show very good agreement.

3. Maximum Temperature Difference

The maximum temperature difference between the front and the back of the dust particle is caused by the energy flux. The gradient of the temperature is proportional

to the energy flux, that is,

$$\begin{aligned}
\frac{1}{2} m_{\rm g} n_{\rm post} v_{\rm vel}^3 &= -\lambda \frac{\partial T}{\partial z} \sim -\lambda \frac{\Delta T}{r_{\rm s}}, \\
\Delta T_{\rm max} &= = \frac{1}{2} m_{\rm g} n_{\rm post} v_{\rm vel}^3 \frac{r_{\rm s}}{\lambda}, \\
&= 45.1 \text{ K} \Big(\frac{n_{\rm post}}{2 \times 10^{14} \text{ cm}^{-3}} \Big) \Big(\frac{v_{\rm sh}}{10 \text{ km s}^{-1}} \Big)^3 \Big(\frac{r_{\rm s}}{1 \text{ mm}} \Big). \qquad (108)
\end{aligned}$$

This maximum temperature difference also compare with the calculation results in table 5. They show a very god agreement.

Shock parameters	Heating rate (simulation)	Heating rate (analysis)
Case (a)	32.2 K s^{-1}	35.5 K s^{-1}
Case (b)	6.3 K s^{-1}	7.1 K s^{-1}
Case (c)	243.6 K s^{-1}	284.0 K s^{-1}
Case (d)	65.0 K s^{-1}	71.0 K s^{-1}
Shock parameters	Peak temperature (simulation)	Peak temperature (analysis)
Case (a)	1828 K	1829 K
Case (b)	1839 K	1829 K
Case (c)	3031 K	3079 K
Case (d)	2152 K	2175 K
Shock parameters	Temp diff (simulation)	Temp diff (analysis)
Case (a)	45.0 K	45.1 K
Case (b)	199.0 K	225.5 K
Case (c)	323.0 K	360.8 K
Case (d)	87.0 K	90.2 K

Table 5: Comparison of the results of numerical simulation with our analyses. We compare the heating rate, the peak temperature, and the temperature difference. Shock parameters (cases a - d) correspond to Fig. 45(a) - (d).

D.3.3 Effect of Deceleration of Dust

Figure 46 shows temperature evolution of the front, the center, and the back of the dust particle. Parameters are same as figure 45(a). While the temperature evolution before reaching peak temperature is almost same as the case with Fig 45(a), after reaching peak temperature the temperature decreases gradually because of the deceleration of the dust particle.

D.3.4 Dust Rotation

Figure 47(a) shows the temperature evolution of the front, the center, and the back of the dust particle with rotation frequency $f = 0.1$ s^{-1}. Parameters except for rotational frequency are the same as Fig. 45(a) We define the front, the center, and the back as the front, the center, and the back toward the gas flow at initial. Parameters except for rotational frequency are same as Figure 45(a). The maximum temperature difference between the front and the back of the dust particle is smaller than the case without rotation because the heat flux from the gas flow is dissipated on the surface of the dust particle. In this case, the maximum temperature difference between the front and the back ($\Delta T_{\rm fb}$) is greater than that between the front and the center ($\Delta T_{\rm fc}$). Figures 48(a)-(c) are the temperature distribution on $x - y$ (a), $y - z$ (b), and $z - x$ (c) plane when the center of the dust particle reaches the peak temperature. The temperature around the gas flow is higher than the opposite side. We call this type of the distribution *layered*.

Figure 47(b) shows the temperature evolution with rotational frequency $f = 100$ s^{-1}. The temperatures of the front, the center, and the back is almost the same and the difference is less than 5 K. Figure 47(c) is a close up of panel (b) around

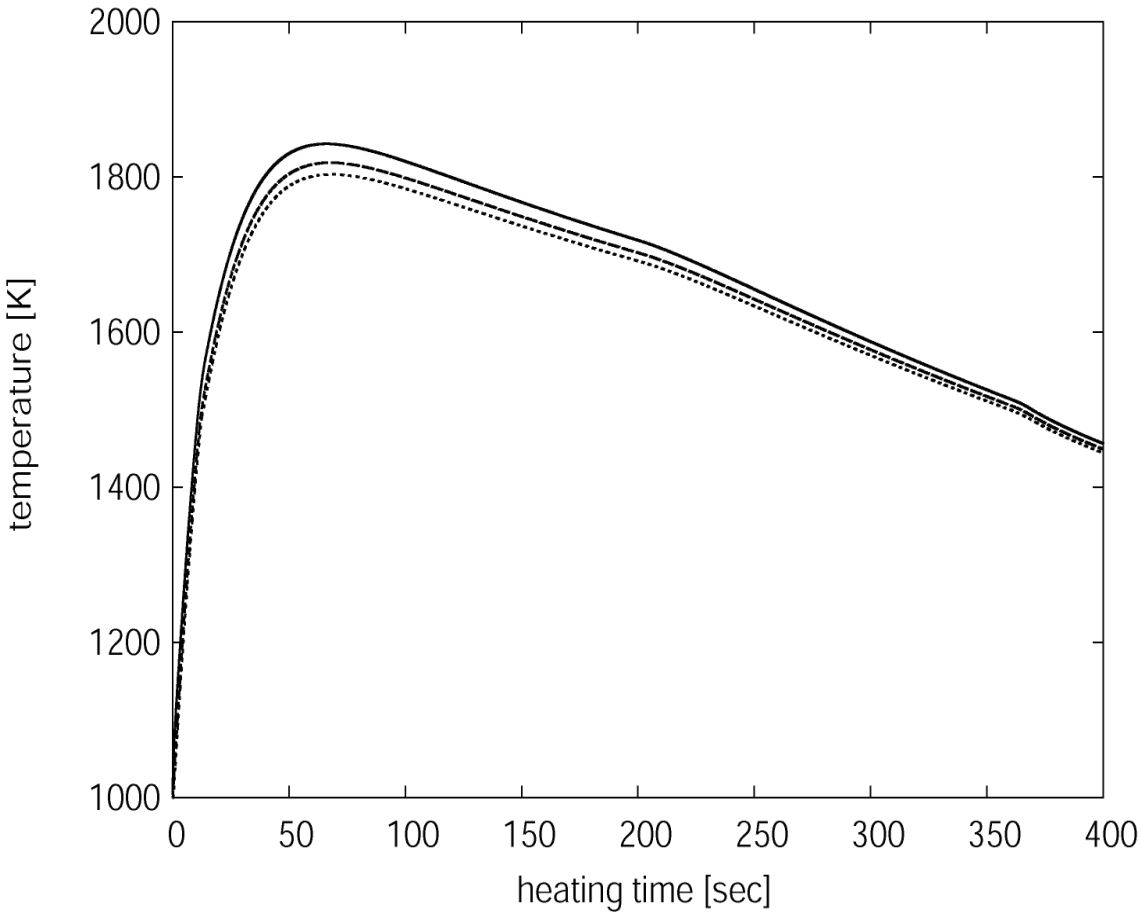

Figure 46: The time evolution of the temperature in the dust particle vs. heating time. Parameters are the same as Fig. 45. Decreasing heating due to the deceleration of the dust particle is considered. The solid, dashed, and dotted lines represent the front, center, and back of the dust particle.

the peak temperature. We can see that a temperature difference exists between the front (or the back) and the center, that is, the surface and the center ($\Delta T_{\rm fb} < \Delta T_{\rm fc}$). Figure 45(d) - (f) are the temperature distribution on $x-y$ (d), $y-z$ (e), and $z-x$ (f) plane, respectively. The temperature on the equator of the dust particle is the hottest, on the contrary, the temperature at the center is the coolest. We call this type of the distribution *cylindrical*. We find that the dust particle heated by shock wave has two types of temperature distributions depending on the rotational frequency.

Figures 49(a) and (b) show the maximum temperature difference between the front and the back ($\Delta T_{\rm fb}$), between the front and the center ($\Delta T_{\rm fc}$), respectively. Basically, the temperature difference is larger when the radius of the dust particle is larger and the rotation frequency is larger. However, at upper right region, the temperature difference does not change when the rotation frequency is larger. This is because the rotation only works as the heating energy due to the gas friction dissipates on the surface of the dust particle. In this region, $\Delta T_{\rm fb}$ is less than $\Delta T_{\rm fc}$ and the temperature distribution is *cylindrical*.

D.3.5 Critical Frequency

Whether the temperature distribution becomes *layered* or *cylindrical* depends on whether the temperature of the dust particle changes or not before rotating once. So the critical rotational frequency is obtained from comparing the timescale of the rotation and that of the heating. The timescale of heating is calculated as

$$\begin{aligned} t_{\rm h} &= \frac{2\pi\rho_{\rm d} C r_{\rm s} \Delta T}{3\rho_{\rm g} v_{\rm vel}^3}, \\ &= 0.11\ {\rm sec}\Big(\frac{n_{\rm post}}{2\times10^{14}\ {\rm cm^{-3}}}\Big)^{-1}\Big(\frac{v_{\rm sh}}{10\ {\rm km\ s^{-1}}}\Big)^{-3}\Big(\frac{r_{\rm s}}{1\ {\rm mm}}\Big)\Big(\frac{\Delta T}{1\ {\rm K}}\Big). \end{aligned} \quad (109)$$

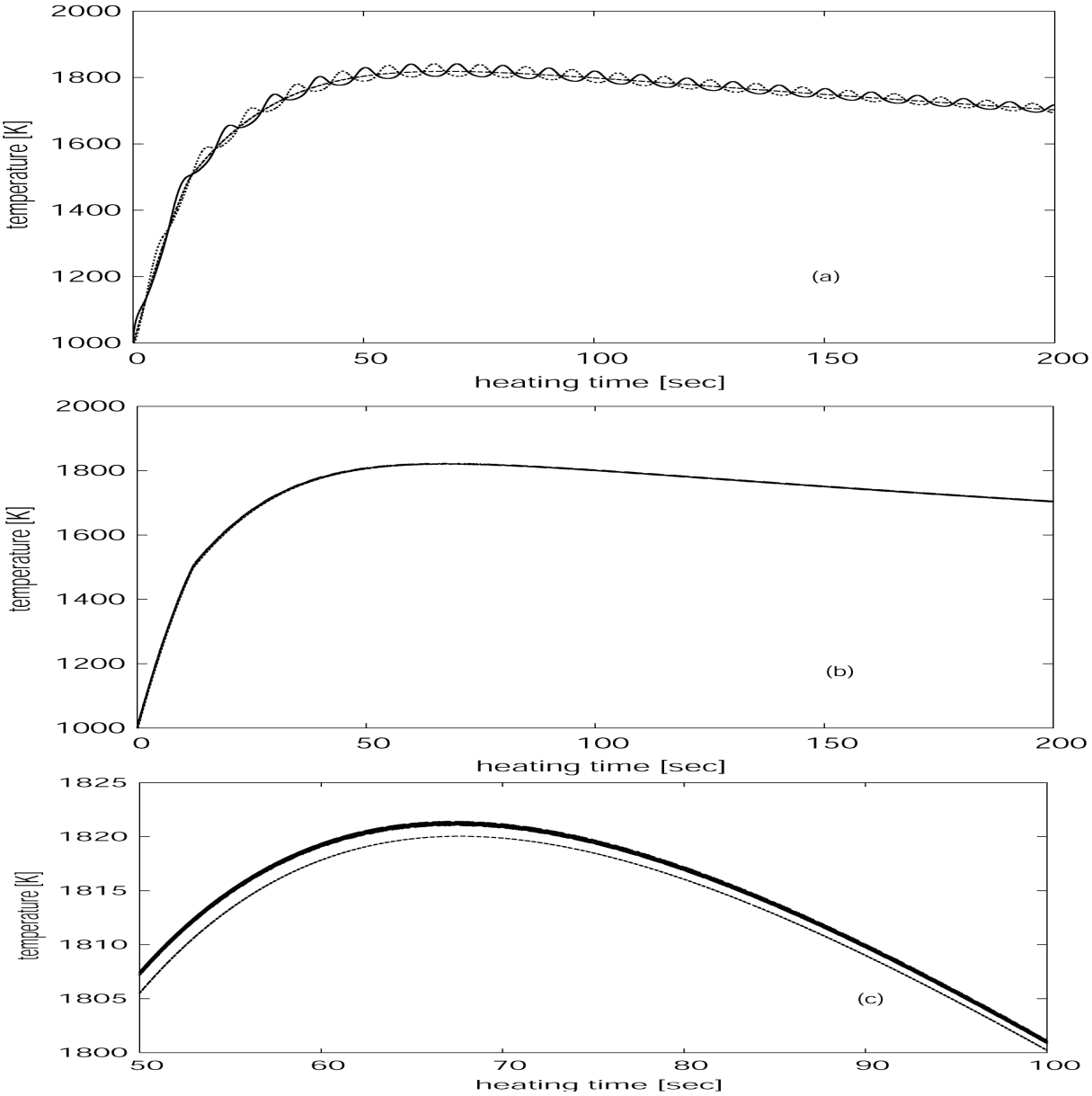

Figure 47: The time evolution of the temperature in the dust particle vs. heating time. Parameters are same as figure 45(a) except for the rotational frequency $f = 0.1$ s^{-1} (a) and $f = 100$ s^{-1} (b). The solid, dashed, and dotted lines represent the front, center, and back of the dust particle. (c) is the expanded figure of the figure (b).

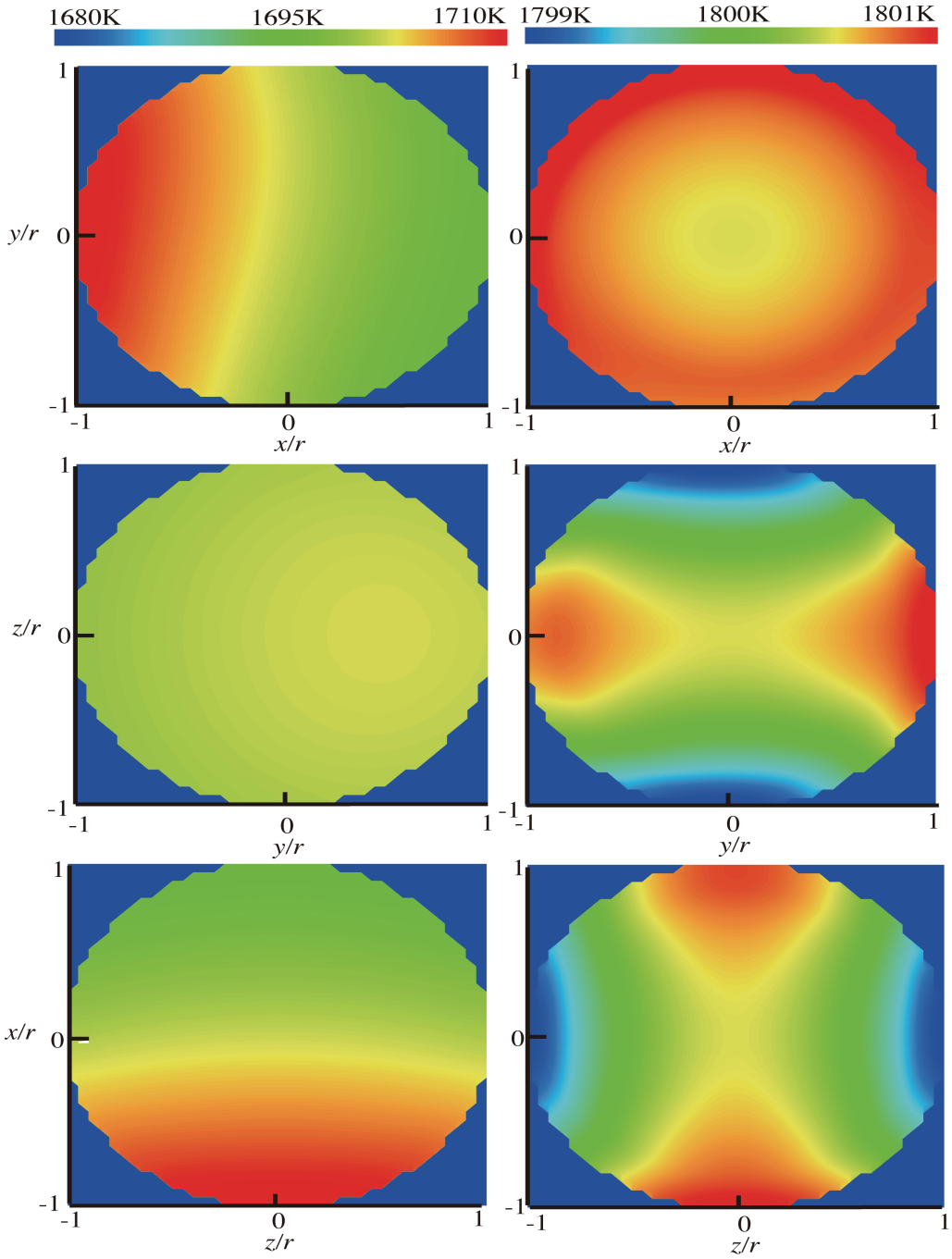

Figure 48: (a) The temperature distribution of the dust particle on $x-y$ plane. (b) $y-z$ plane. (c) $z-x$ plane. Parameters are same as figure 47(a). These pictures are 100 sec after beginning of heating. (d) The temperature distribution of the dust particle on $x-y$ plane. (e) $y-z$ plane. (f) $z-x$ plane. Parameters are same as figure 47(b).

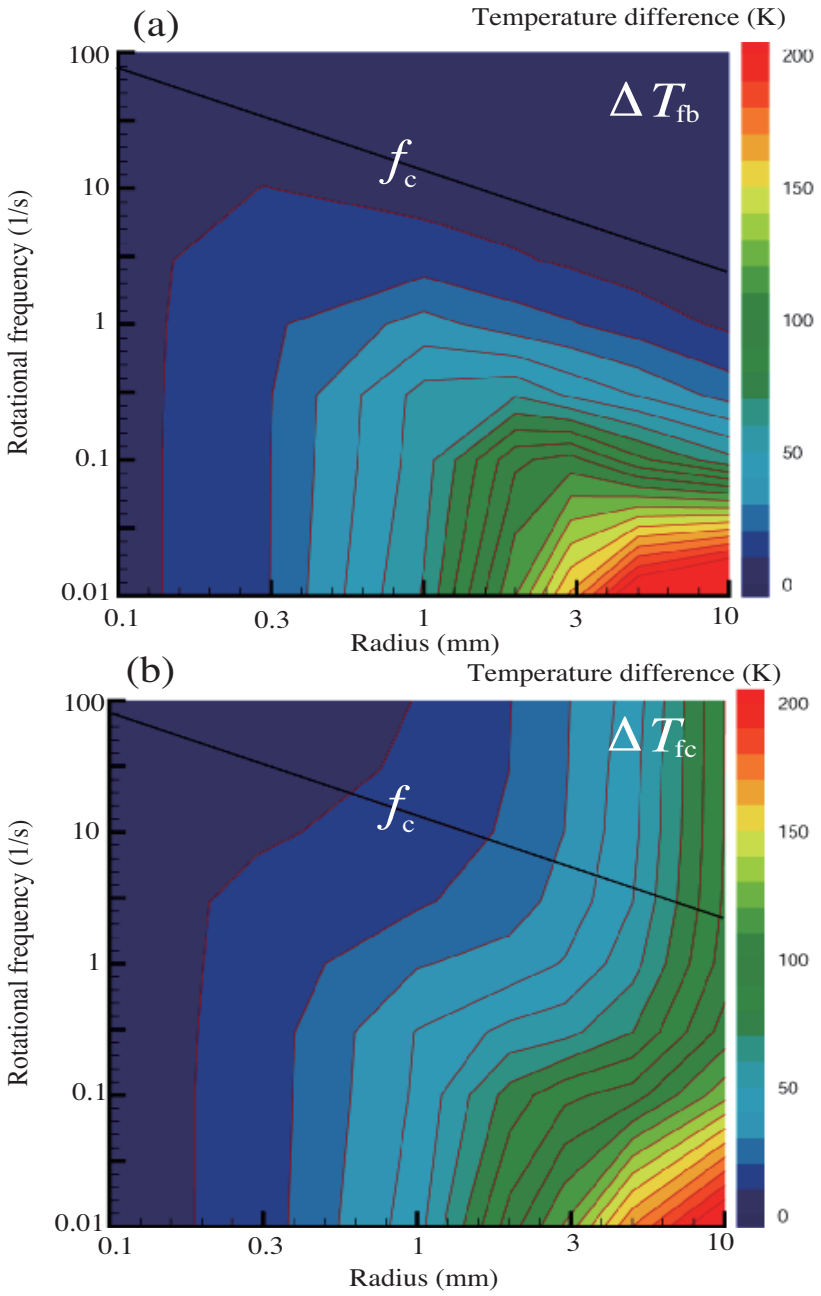

Figure 49: (a) The contour of the maximum temperature difference between the front and back of the dust particle. (b) The maximum temperature difference between the front and center of the dust particle. f_c is the critical rotational frequency.

The timescale of the rotation is written as

$$t_{\rm r} = 1.0 \ {\rm sec}\Big(\frac{f}{1.0 \ {\rm s}^{-1}}\Big). \tag{110}$$

This timescale is a time with which the dust particle makes a turn. We can estimate the critical rotational frequency comparing the timescale of the rotation with that of the heating, and we have,

$$f_{\rm c} = 8.28 \ {\rm s}^{-1}\Big(\frac{n_{\rm post}}{2 \times 10^{14} \ {\rm cm}^{-3}}\Big)\Big(\frac{v_{\rm sh}}{10 \ {\rm km \ s}^{-1}}\Big)^{3}\Big(\frac{r_{\rm s}}{1 \ {\rm mm}}\Big)^{-1}. \tag{111}$$

When the rotation frequency is larger than the critical one, the heating energy from gas friction is evenly distributed on the surface of the dust particle and when $f < f_{\rm c}$ the temperature distribution is *layered*, while when $f > f_{\rm c}$ the temperature distribution is *cylindrical*. Solid line drown in the figure 49 (a) and (b) represent the critical rotational frequency ($f_{\rm c}$). In the region $f < f_{\rm c}, \Delta T_{\rm fb}$ is smaller than $\Delta T_{\rm fc}$ and then the temperature distribution is *layered*. On the other hand, in the region $f < f_{\rm c}, \Delta T_{\rm fb}$ is larger than $\Delta T_{\rm fc}$, and then it is *cylindrical*.

E Development of Thermo-Hydrodynamics Simulation Code

In the shock-wave heating model, the dust particle is heated by the gas friction. The dust particle melts from the front (Appendix D) and the melted part is exposed to the gas flow. In the liquid part, the inner flow is driven by the gas flow and when the dust particle is large enough, the liquid part is stripped from the dust particle (Part II). When we calculate the temperature distribution (Appendix D), we do not consider the inner flow. Moreover, when we simulate the disruption of the dust particle, we assume the initial condition. However, in fact, these phenomena occur simultaneously. In order to investigate the dust particle exposed to the fast gas flow in detail, we need to develop the thermo-hydrodynamics simulation code. In this section, we introduce this code and discuss some difficulties.

E.1 Basic Equations

Basically, we have to do is collaborating two codes (the hydrodynamics code and the heat conduction code). The equation of energy is rewritten as

$$\frac{\partial e}{\partial t} + \boldsymbol{\nabla} \cdot (e\boldsymbol{u}) = a\Delta T + S_{\rm eff}(\Gamma_{\rm g-d} - \Lambda_{\rm rad} + \Gamma_{\rm rad}). \tag{112}$$

Other equations are same as the equations explained in Part II. The calculation method are the same as that in Part II and Appendix E.

E.2 Test Calculation

Figure 50 shows the thermo-hydrodynamics evolution of the dust particle in the fast gas flow. Parameters are $n_{\rm post} = 5 \times 10^{15}$ cm^{-3}, $v_{\rm sh} = 7$ km s^{-1}, and $r_{\rm s} = 1$ cm.

The specific heat is as 10^{-3} times as that of value of the forsterite. At initial the dust particle is solid and the temperature is 1000 K (panel A). While the dust particle is heated by the gas frictional heating, the dust particle has not deformed yet (panels B and C) because its viscosity is still high. After 0.047 sec, the dust particle is gradually deformed by the gas flow (panel D). The higher temperature part is deformed significantly with time (panels E - G) and some arm-like structures appear behind the parent particle (panels H and I). Thus we succeeded the thermo-hydrodynamics simulation.

However, there is a big problem related to CPU time. When we use the specific heat of the forsterite, the timescale of the disruption event is about 10^{-2} sec, on the other hand, that of the heating is about 10-1000 sec. The timestep is limited due to the CFL condition and we have to choose $\Delta t = 10^{-5}$ sec at least. Therefore, we have to calculate $10^6 - 10^8$ steps and we need several years to calculate the thermo-hydrodynamics phenomena. Now, we are developing this simulation code. It will be possible to simulate thermo-hydrodynamics phenomena in realistic time in the near future.

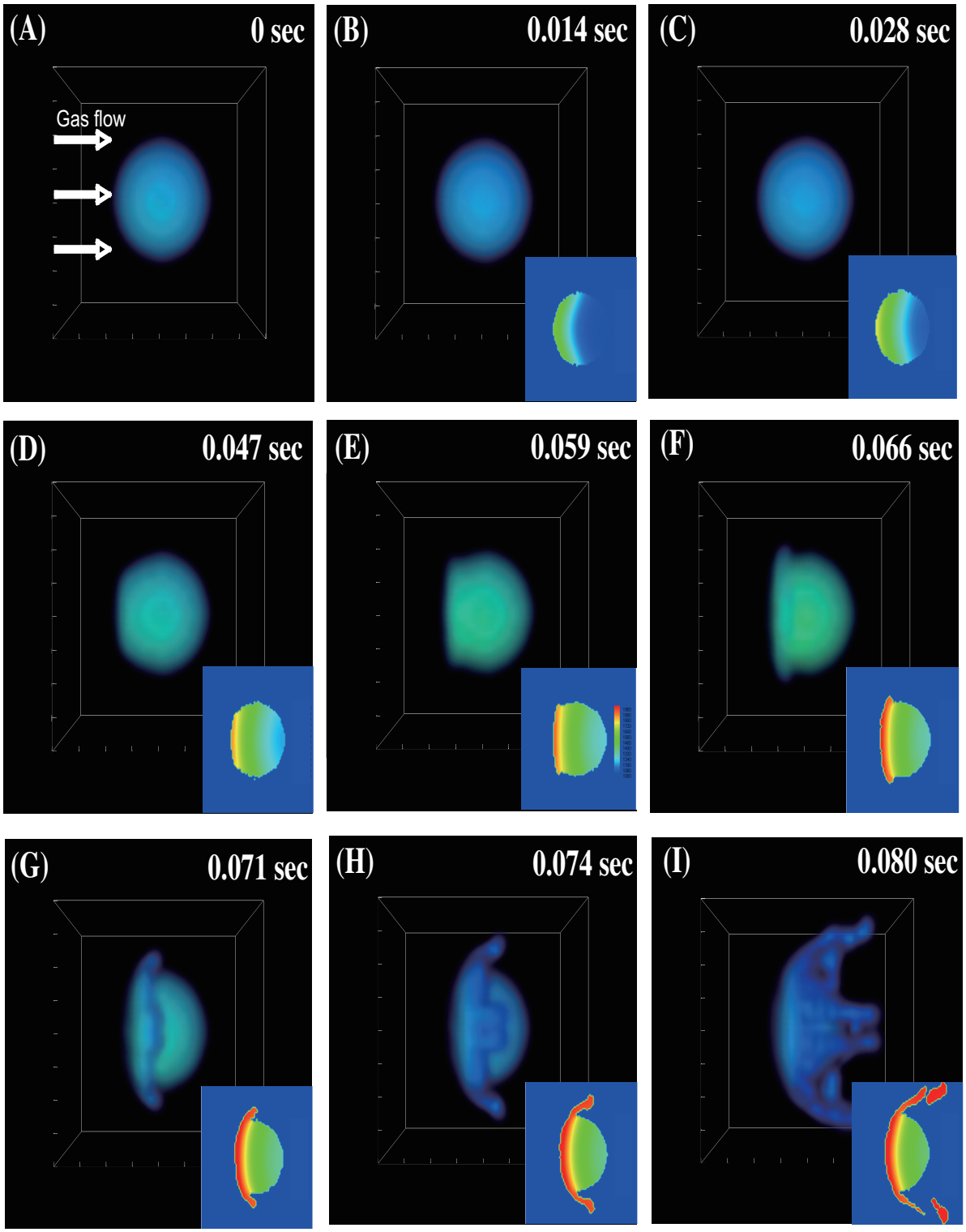

Figure 50: The thermo-hydrodynamics evolution of the dust particle exposed to the gas flow. The blue object represents the dust particle. The contour at bottom shows the temperature distribution on $y - z$ plane.

References

[1] Akaki, T., Nakamura, T., 2004. The formation process of adhering and consorting compound chondrules inferred from their petrology and major-element composition. Workshop on Chondrites and Protoplanetary Disk. 9021.

[2] Akaki, T., Nakamura, T., 2005. Formation processes of compound chondrules in CV3 carbonaceous chondruites: Constraints from oxygen isotope ratios and major element concentrations. Geochim. Cosmochim. Acta 69, 2907-2929.

[3] Alexander, C. M., Grossman, J. N., Ebel, D. S., Ciesla, F. J., 2008. The formation conditions of chondrules and chondrites. Science. 320, 1617.

[4] Amelin, Y., Krot, A., N., Hutcheon, I., D., Ulyanov. A., A. Lead isotopic ages of chondrules and calcium-alminium-rich inclusions. Science. 297., 1678.

[5] Ashgriz, N., Poo, J. Y., 1990. Coalescence and separation in binary collisions of liquid drops. J. Fluid Mech. 221, 183-204.

[6] Bottinga, Y., Weill, D. G., 1972. The viscosity of magmatic silicate liquids: A model for calculation. Am. Jour. Sci. 272, 438-475.

[7] Ciesla, F.J., hood, L.L., 2002. The nebular shock wave model for chondrule formation: Shock processing in a particle-gas suspension. Icarus 158, 281-293.

[8] Ciesla, F. J., 2006. Chondrule collisions in shock waves. Meteorit. Planet. Sci. 41, 1347-1359.

[9] Cuzzi, J. N., Alexander, C. M., 2006. Chondrule formation in particle-rich nebular regions at least hundreds of kilometers across. Nature. 441,483-485.

[10] Desch, S.J., Connolly Jr., H.C., 2002. Amodel of the thermal processing of particles in solar nebula shocks: Application to the cooling rates of chondrules. Meteorit. Planet. Sci. 37, 183-207.

[11] Gooding, J. L., Keil, K., 1981. Relative abundances of chondrule primary textural types in ordinary chondrites and their bearing on conditions of chondrule formation. Meteoritics 16, 17-43.

[12] Hood, L.L., Horanyi, M., 1991. Gas dynamic heating of chondrule precursor grains in the solar nebula. Icarus 93, 259-269.

[13] Hood, L.L., Horanyi, M., 1993. Thee nebular shock wave model for chondrule formation- One-dimensional calculations. Icarus 106, 179-189.

[14] Hood, L.L., 1998. Thermal processing of chondrule and CAI precursors in planetesimal bow shocks. Meteorit. Planet. Sci. 33, 97-107.

[15] Iida, A., Nakamoto, T., Susa, H., Nakagawa, Y., 2001. A shock heating model for chondrule formation in a protoplanetary disk. Icarus 153, 430-450.

[16] Jiang, I, Y., Umemura, A., Law, K, C., 1992. An experimental investigation on the collision behaviour of hydrocarbon droplets. J. Fluid Mech. 234, 171.

[17] Jones, R. H., Lee, T., Connolly Jr., H. C., Love, S. G., Shang, H., 2000. Formation of chondrules and CAIs: Theory vs. Observation. In: Boss, A. P., Russell, S. S. (Eds.), Protostars and Planets IV. Univ. of Arizona Press, Tucson, pp. 927-962.

[18] Kadono, T., Arakawa, M., 2005. Breakup of liquids by high velocity flow and size distribution of chondrules. Icarus 197, 621-626.

[19] Kadono, T., Arakawa, M., Kouchi, A., 2008. Size distributions of chondrules and dispersed droplets caused by liquid breakup: An application to shock wave conditions in the solar nebula. Icarus 173, 295-299.

[20] Kato, T., Nakamoto, T., Miura, H., 2006. Maximal size of chondrules in shock wave heating model: Stripping of liquid surface in a hypersonic rarefied gas flow. Meteorit. Planet. Sci. 41, 49-65.

[21] Kouchi, A., Yamamoto, T., Kozasa, T., Kuroda, T., Greenberg, J, M., 1994. Conditions for condensation and preservation of amorphous ice and crystallinity of astrophysical ices. Astron. Astrophys. 290, 1009-1018.

[22] Liffman, K., Brown, M. J. I., 1996. The Protostellar Jet Model of Chondrule Formation. Chondrules and The Protoplanetary Disk 285-302.

[23] Miura, H., Nakamoto, T., Susa, H., 2002. A shock-wave heating model for chondrule formation: effects of evaporation and gas flows on silicate particles. Icarus 160, 258-270.

[24] Miura, H., Nakamoto, T., 2005. A shock-wave heating model for chondrule formation. II. Minimum size of chondrule precursors. Icarus 175, 289-304.

[25] Miura, H., Nakamoto, T., 2006. A shock-wave heating model for chondrule formation: Prevention of isotopic fractionation. Astrophys. J. 651, 1273-1295.

[26] Miura, H. 2006. Shock-wave heating model for chondrule formation: Thermal evolution of precursor dust particles and hydrodynamics of molten droplets. Doctoral thesis. in university of Tsukuba.

[27] Miura, H., Nakamoto, T., 2007. Shock-wave heating model for chondrule formation: Hydrodynamic simulation of molten droplets exposed to gas flows. Icarus 188, 246-265.

[28] Miura, H., Yasuda, S., Nakamoto, T., 2008a. Fragment-collision model for compound chondrule formation: Estimation of collision probability. Icarus 194, 811-821.

[29] Miura, H., Nakamoto, T., and Doi, M., 2008b. Origin of three-dimensional shapes of chondrules. I: Hydrodynamics simulations of rotating droplet exposed to high-velocity rarefied gas flow, Icarus, in press.

[30] Murase, T., McBirney, A. R., 1973. Properties of some common igneous rocks and their melts at high temperatures. Geol. Soc. Am. Bull. 84, 3563-3592.

[31] Nagashima, K., Tsukamoto, K., Satoh, H., Kobatake, H., Dold, P., 2006. Reproduction of chondrules from levitated, hypercooled melts. J. Crystal Growth. 293, 193-197.

[32] Nakamoto, T., Miura, H., 2004. Collisional destruction of chondrules in shock waves and inferred dust to gas ratio. Lunar Planet. Sci. 35, 1847.

[33] Nakamura, T., Yabe, T. 2001. Exactly conservative semi-lagrangian scheme for multi-dimensionla hyperbolic equations with directional splitting technique. Journal of Computational Physics. 182. 118-148.

[34] Plateau, J. 1873. Statique experimentale at theorique des liquides soumis aux seules forces moleculaires. Gauthier-Villars, Paris.

[35] Qian, J., Law, C. K., 1997. regimes of coalescence and separation in droplet collision. J. Fluid Mech 331, 59-80.

[36] Rayleigh, L. 1879. Scientific Papers (Cambridge University Press, Cambridge). Proc. R. Soc. London 29, 71.

[37] Ruzmaikina, T.V., Ip, W.H., 1994. Chondrule formation in radiative shock. Icarus 112, 430-447.

[38] Sekiya, M., Nakamura, T., 1996. Condition for the formation of the compound chondrules in the solar nebula. Proc. NIPR Symp. Antarct. Meteorites 9, 208-217.

[39] Sekiya, M., Uesugi, M., Nakamoto, T., 2003. Flow in a liquid sphere moving with a hypersonic velocity in a rarefied gas. Progr. Theor. Phys. 109, 717.

[40] Tanaka, K. K., Tanaka, H., Nakazawa, K., 1998. Shock heating due to accretion of a clumpy cloud onto a protoplanetary disk. Icarus 134, 137-154.

[41] Tanaka, K. K., Yamamoto, K., Nagashima, K., Tsukamoto, K. 2008. A new method of evaluation of melt/crystal inerfacial energy and activation energy of diffusion, Journal of Crystal Growth 310, 1281-1296.

[42] Uesugi, M., Sekiya, M., Nakamoto, T., 2003. Deformation and internal flow of a chondrule-precursor molten sphere in a shocked nebular gas. Earth, Planets and Space. 55, 493-507.

[43] Wasson, J. T., Alexander, N. K., Lee, M. S., Rubin, A. E., 1995. Compound chondrules. Geochim. Cosmochim. Acta 59, 1847-1869.

[44] Xiao, F., Yabe, T. 2001. Completely conservative and oscillationless semi-lagrangian schemes for advection transportation. Journal of Computational Physics. 170. 498.

[45] Yabe, T., Wang, P-Y., 1991. Unified Numerical procedure for compressible and incompressible fluid. Journal of the Physical Society of Japan. 60, 2105-2108.

[46] Yabe, T., Xiao, F., Utsumi, T., 2001. The constrained interpolation profile method for multiphase analysis. Journal of Computational Physics. 169, 556.

[47] Yasuda, S., Nakamoto, T., 2005. Inhomogeneous temperature distribution in chondrules in shock-wave heating model. Lunar Planet. Sci. 36, 1252-1253.

[48] Yasuda, S., Nakamoto, T., 2006. Possible size of porphyritic chondrules in shock-wave heating model. Lunar Planet. Sci. 37, 1674-1675.